Scholars' Mine

Spring 2018

Modeling and characterization of thermo-oxidative behavior of bismaleimide composites

Rafid Muhammad Hussein

MODELING AND CHARACTERIZATION OF THERMO-OXIDATIVE BEHAVIOR

OF BISMALEIMIDE COMPOSITES

by

RAFID MUHAMMAD HUSSEIN

A DISSERTATION

Presented to the Faculty of the Graduate School of the

MISSOURI UNIVERSITY OF SCIENCE AND TECHNOLOGY

In Partial Fulfillment of the Requirements for the Degree

DOCTOR OF PHILOSOPHY

in

MECHANICAL ENGINEERING

2018

Approved by
K. Chandrashekhara, Advisor
L. R. Dharani
K.M. Isaac
A. Okafor
V. A. Samaranayake

PUBLICATION DISSERTATION OPTION

This dissertation has been prepared in the form of three papers for publication as follows:

Paper I: pages 9-45 have been published in Journal of Materials Science.

Paper II: pages 46-78 are under review in Mechanics of Time-Dependent Materials.

Paper III: pages 79-115 have been published in Applied Composite Materials.

ABSTRACT

High-temperature polymer matrix composites (HTPMCs) are susceptible to thermo-oxidation, which accelerates the composites' degradation and reduces the service life. Mechanical properties of HTPMCs deteriorate due to coupled thermo-oxidation and cross-linking mechanisms. Bismaleimides (BMIs) are commonly used high-temperature resins for aerospace applications. This work presents the viability of using experimental weight loss to model the spatial distribution of oxidation when the oxidized polymer matrix is not discernible. Three tasks are introduced: (1) Anisotropic oxidation prediction using optimized weight loss behavior of bismaleimide composites, (2) A multi-scale modeling of thermo-oxidative effects on the flexural behavior of cross-ply bismaleimide composites, and (3) Thermo-oxidative induced damage in polymer composites: microstructure image-based multi-scale modeling and experimental validation. Task 1 deals with simulating the weight loss and oxidized layer evolution in unidirectional BMI composites exposed to a service temperature in the operating range, 176.67 °C (350 °F) and 200 °C (392 °F). In task 2, microstructural changes of the cross-ply BMIs composites were characterized using microscopy. A multiscale approach for modeling flexural modulus degradation was proposed. In Task 3, a multi-scale modeling approach is presented to simulate and validate thermo-oxidation shrinkage and cracking damage. The micro-scale shrinkage deformation and cracking damage are simulated and validated using 2D and 3D simulations. The meso-scale geometrical domain and the micro-scale geometry and mesh are developed using the object oriented finite element (OOF). The macro-scale shrinkage and weight loss are measured using unidirectional coupons and used to build the macro-shrinkage model.

ACKNOWLEDGMENTS

TABLE OF CONTENTS

LIST OF ILLUSTRATIONS

LIST OF TABLES

SECTION

1. INTRODUCTION

High-temperature polymer composites are used under severe environmental conditions for aerospace applications like jet engines and lead edge of fighter wings. These materials are in direct contact with service oxidative environments which can lead to cross-linking progression, superficial thermo-oxidation, fiber/matrix interface debonding, and matrix micro-cracking. These degradation mechanisms play a significant role in determining the residual elastic and strength properties of the composite. Thermo-oxidation is a thermally-activated diffusion and reaction process taking place in the composite's surfaces under oxidative environments. The superficial oxidation evolves deeply in to the composite's core as aging time elapses. Simultaneously to oxidation, a matrix decomposition takes place throughout the matrix volume. Oxidation and polymer decomposition are characterized by weight loss and volumetric shrinkage in the aged composites. The oxidized layers are also denser than the virgin matrix.

Degradation of HTPMC is a time, pressure and temperature-dependent phenomenon involving significant evolution of the mechanical, thermo-physical and chemical properties. These changes initiate at the molecular level of the polymer matrix in the form of cure/cross-linking progression, which lead to a sudden drop in the mechanical elastic properties in the early hundreds of aging time. The strength properties are less susceptible to these effects compared to the elastic properties in this stage. The cross-linking progression reaches a saturation point beyond which oxidation effects are more

dominant in the form of fiber/matrix interface debonding and micro-cracking damage. Due to thermo-oxidation, the affected superficial layer shrinks leading to the formation of a complex stress state in the surrounding fibers, matrix and fiber/matrix interface, which finally leads to the micro-cracking damage.

This work presents the viability of using experimental weight loss to model the spatial distribution of oxidation when the oxidized polymer matrix is not discernible. The oxidized layer thickness and weight loss are predicted at a microscale level by implementing a volumetric integral in a finite element analysis and scaled to a macroscale level by respective area ratios. This frame work is utilized to predict the shrinkage strains, stresses, and the associated micro-cracking and Damage.

2. LITERATURE REVIEW

Thermo-oxidation of polymer matrix composites is a major cause of degradation for high- temperature applications where chemical aging dominates the service life estimation. Properties such as laminates' ultimate strength, notched strength and flexural strength are critical. Thermal oxidation mainly affects the matrix-dominated properties of polymer composites namely the transverse and shear properties [1]. Polyimides and bismaleimides (BMIs) are commonly used high-temperature resins for aerospace applications. Polyimides have good mechanical properties at elevated temperatures, but they are associated with high costs and manufacturing difficulty. BMIs, due to their thermal stability at high temperatures and ease of manufacturing are a good alternative to epoxies and polyimides for extended use under severe environments [2]. Thermal oxidation behavior of high-temperature resins such as BMI, PETI-5 and PMR-15 was studied by many researchers using empirical, finite-difference, and finite element modeling. Bellenger et al. [3] studied the weight loss of unidirectional carbon/epoxy composites aged at 150 and 180 °C. The effect of surface roughness on oxidation weight loss was introduced by Kung [4]. A modified rule of mixtures was developed to account for the surface roughness effect on the oxidation-exposed area. The concept of equivalent isothermal time was introduced by Chung et al. [5] by studying the weight loss of unidirectional and cross-ply carbon fiber/rubber-modified epoxy composites in the range of 170 to 200 °C. Parameters of weight loss models were fitted using experimental data showing a diffusion-controlled degradation mechanism.

In addition, thermo-oxidation was studied using finite element analysis (FEA) and representative volume elements (RVEs) to predict the behavior of composite oxidation [1, 6]. The oxidized layer growth under isothermal conditions was modeled based on a diffusion–reaction and an oxidation state equation. A three-zone model was used to describe the transient evolution of the oxidation variable by fitting a time-dependent function to account for variable weight loss rates.

However, few researchers studied the effects of the thermal oxidation on the mechanical properties and behavior of the polymer matrix composites. These studies were also limited to specific problems like elastic constants and flexural stiffness degradation for a unidirectional laminates. Roy et al. [7, 8] used continuum damage mechanics (CDM) analysis of a pre-existing fiber/matrix debond to model the damage evolution due to oxygen diffusion. The fiber/matrix damage was analyzed using a debonded representative volume element (RVE). Upadhyaya et al. [9] investigated the long-term degradation in the inter-laminar strength of unidirectional IM-7/PETI-5 laminates subjected to oxidation at 300 °C up to 2,000 hours. An internal state variable (ISV) was used to account for the molecular oxidation damage. 2D viscoelastic cohesive layer modeling was utilized to predict the delamination numerically. The local shear model predictions for the cohesive layer showed a significant decrease of 73 % and 68 % in shear modulus and strength after 2,016 hours of aging, respectively. Haque et al. [10] implemented a 2D viscoelastic cohesive layer model to simulate the changes in the flexural properties in a three-point bend test. Unidirectional IM7/BMI samples were aged at 260 °C for 3,000 hours in air. It was observed that weight loss rate, flexural modulus and strength were significantly reduced in the samples having fibers in transverse direction. Meng et al. [11] developed a 3D finite

element model of the three-point bend test for unidirectional, cross-ply and angle-ply carbon epoxy laminates. The modeling results revealed significant transverse normal stresses and in-plane shear stress in the cross-ply and angle-ply laminates, respectively.

In the literature, the study of stress effects on thermo-oxidation behavior was limited to neat resin. Antoun et al. [12] investigated the effect of pressure and stress on thermo-oxidation behavior of BMI resin samples. A stress-coupling parameter was then introduced and determined using experimental outcomes under tension stress of 13.8 MPa. When the model was validated under 34.5 MPa, a discrepancy was risen in the results which was attributed to shrinkage and erosion effects.

Micro-scale damage is localized and dependent on the microstructural characteristic. An isomorphic microstructure can be built using object oriented finite element analysis (OOF) tool to analyze materials' behavior using microstructural images [1–4]. In the field of polymer composites/nanocomposites, OOF was used to investigate mechanical properties, especially the elastic modulus. Goel et al. [5] investigated the elastic modulus of a chopped glass fiber and polypropylene matrix thermoplastic composite. Dong and Bhattacharyya [6, 7] built a model to determine the tensile modulus of polypropylene/organoclay nanocomposites at various clay contents using OOF.

Damage induced by thermo-oxidation was studied by a few investigators focusing on a homogenized composite domain. An and Pochiraju [11] simulated the oxidation and damage growth of bismaleimide (BMI) resin and cross-ply laminates. The analysis was implemented in the macro-scale for a neat resin plate subjected to bending and a laminated plate with a hole subjected to a tensile loading using extended finite element method (XFEM) and Hashin-Rotem law. Liang and Pochiraju [12] presented a simulation scheme

for the isothermal oxidation damage of unidirectional carbon polyimide composites. Damage initiation was analyzed using Hashin's failure criteria. XFEM, cohesive elements, and a traction-separation law were used for modeling crack initiation and propagation. Daghia et al. [13] investigated the damage evolution in the transverse direction of oxidized superficial layers in thin cross-ply epoxy plates. The damage kinetics was modeled in the meso-scale using 2D FEA assuming a constant thickness of the oxidized layer.

3. SCOPE AND OBJECTIVES

This dissertation comprises three papers corresponding to the following problems.

The first paper is titled "Anisotropic Oxidation Prediction Using Optimized Weight Loss Behavior of Bismaleimide Composites." In this paper, 3D finite element models for the thermo-oxidation of unidirectional BMI composites are developed and analyzed using the micromechanics approach. This work is dedicated to study the diffusion-limited regime of the thermal oxidation where oxygen excess case is not considered. Optimized parameters are introduced to account for the temperature dependence of the proportionality function. The weight loss % in air at 200 °C (392 °F) and 176.67 °C (350 °F) are investigated using oxidative aging experiments. The longitudinal and transverse homogenized diffusivities are determined by averaging. The degree of non-linearity is predicted at both temperatures to describe the contribution of cracking thermo-oxidation. A novel index is presented that corresponds to the weight loss per unit volume of the completely oxidized matrix.

The second paper is titled "Multi-Scale Modeling of Thermo-Oxidation Effects on the Flexural Behavior of Cross-Ply Bismaleimide Composites." In this paper, the flexural behavior of aged cross-ply bismaleimide composites is investigated experimentally and numerically. An analysis of the degradation mechanisms: cross-linking and oxidation in a multiscale approach is presented to gain a better understanding of the flexural behavior under aging. Simulated numerically and verified experimentally, the failure mechanisms of the matrix and fiber under tension/compression and shear are considered. Experiments are conducted to collect the weight loss data at 176.67 °C for around 1,700 hours. Simultaneously, three-point bending test coupons are also aged and tested to inspect the

changes in the flexural properties. The micro-cracking/ debonding damage is monitored using SEM of aged coupons.

The third paper is titled "Thermo-Oxidative Induced Damage in Polymer Composites: Microstructure Image-Based Multi-scale Modeling and Experimental Validation." In this paper, a multiscale approach is proposed to simulate the shrinkage deformation and micro-scale cracking damage. The effects of the global thermo-oxidation on the local boundary conditions are considered by running macro- and meso-scale simulations and extracting the induced 3D displacements (u, v, and w). These displacement boundary conditions are then applied to the respective micro-scale simulations utilizing an OOF-generated mesh and geometry. The oxidative macro-shrinkage strain is assumed linearly dependent on the oxidation state variable and attains its maximum value when the matrix is completely oxidized. The micro-cracking is validated using a 3D static simulation to the OOF- generated/replicated mesh and geometrical domain.

PAPER

I. ANISOTROPIC OXIDATION PREDICTION USING OPTIMIZED WEIGHT LOSS BEHAVIOR OF BISMALEIMIDE COMPOSITES

R.M. Hussein, S. Anandan and K. Chandrashekhara
Department of Mechanical and Aerospace Engineering
Missouri University of Science and Technology, Rolla, MO 65409

ABSTRACT

High-temperature polymer matrix composites are susceptible to thermo-oxidation, which accelerates their degradation and reduces the service life. This work presents the viability of using experimental weight loss for modeling the spatial distribution of oxidation when the oxidized polymer matrix is not discernible due to cracking. The oxidized layer thickness and weight loss were predicted at a microscale level by implementing a volumetric integral in finite element analysis and scaled to a macroscale level by respective area ratios. Weight loss was shown to have a spatial distribution following the three-zone model. The proportionality parameter was optimized by fitting the scaled finite element predictions to the experimental results using artificial neural networks and a generalized pattern search algorithm. Aging experiments have been conducted at the operating temperature range of BMIs, 176.67 °C (350 °F) and 200 °C (392 °F). Optical dark field images were acquired to monitor longitudinal and transverse oxidation. Microscale simulations were conducted using representative volume elements

utilizing COMSOL Multiphysics. A novel characteristic index for describing the completely oxidized matrix was the weight loss per unit volume that equals 0.44 mg/μm^3 as shown by spatial distribution simulations. The orthotropic diffusivity resulted in a higher degree of anisotropy in the oxidized thickness compared to the weight loss %. At the representative volume element scale, the oxidized layer thickness simulations showed a higher degree of nonlinearity at higher temperatures stemming from the cracking effect.

1. INTRODUCTION

Degradation of polymer matrix composites under extreme environmental conditions is a major concern for their extended service life. In aerospace applications, where composites are exposed to high temperature and moisture conditions, composite properties deteriorate due to accelerated aging. Chemical, physical and thermomechanical aging mechanisms interact in a complex manner resulting in composite degradation [1]. Polyimides and Bismaleimides (BMIs) are traditionally used as high temperature resins for aerospace applications. Although polyimides have good mechanical properties at elevated temperatures, they are associated with high costs and manufacturing difficulty. Due to their thermal stability at high temperatures and ease of manufacturing, BMIs are a good alternative to epoxies and polyimides for extended use under severe environments [2]. In thermal oxidation, oxygen diffuses and reacts on the exposed surfaces resulting in grafted oxygen and polymer decomposition. Volatiles produced during polymer decomposition diffuse out of the part. Polymer decomposition by chain breaking reactions takes place simultaneously with superficial oxidation. Weight loss, density increase, and volumetric

shrinkage are observed during the propagation of the oxidized layer. Due to volumetric shrinkage, strain and stress fields are built up, leading to matrix cracking [3]. Although polymer oxidation is a superficial phenomenon, decomposition reactions are associated with a volumetric degassing of chain cleavage products. Anisotropy in the oxidation of polymer matrix composites has been reported and characterized with a preferential oxidation path along fibers. The stressed fiber-matrix interface region is considered to be a possible reason for the assisted diffusion-reaction. The effect of fiber sizing on the stoichiometry of the polymer matrix at the interface region has been presented as a second possible reason for preferential oxidation [4]. Many researchers used weight loss models to study the thermo-oxidation of polymer and polymer matrix composites. Bellenger et al. [5] studied the weight loss of unidirectional carbon/epoxy composites aged at 150 °C and 180 °C. Weight loss was estimated as the sum of grafted oxygen on the matrix and eliminated water and volatiles by solving a closed loop mechanistic scheme of reactions. The effect of surface roughness on oxidation weight loss was introduced by Kung [6]. A modified rule of mixtures was developed to account for the surface roughness effect on the oxidation- exposed area. Experimental weight loss data was taken from another study and used for comparison. The comparison showed a higher discrepancy along the fiber direction that was attributed to the effect of oxidation cracking in the fiber direction that penetrated into the matrix resulting in increased area of oxidation exposure. The concept of equivalent isothermal time was introduced by Chung et al. [7] by studying the weight loss of unidirectional and cross-ply carbon fiber/rubber modified epoxy composites in the range of 170 °C to 200 °C. Parameters of weight loss models were fitted using experimental

data showing a diffusion-controlled degradation mechanism. Weight loss predictions of cross-ply samples showed a discrepancy, especially close to 200 °C.

In addition, thermo-oxidation has been studied using finite element analysis (FEA) and representative volume elements (RVEs) to predict the behavior of composite oxidation [1, 8, 9]. The oxidized layer growth under isothermal conditions was modeled based on a diffusion-reaction and an oxidation state equation. A three-zone model was used to describe the transient evolution of the oxidation variable by fitting a time-dependent function to account for variable weight loss rates. In the aforementioned models, although empirical weight loss models were limited to describing the overall sample's oxidation, FEA models were mainly built to estimate the spatial distribution of the oxidized layer.

In the present work, FEA models were developed using COMSOL Multiphysics to predict the weight loss and the oxidized layer thickness in the range of 176.67 °C (350 °F) to 200 °C (392 °F). Weight loss was predicted at the micro scale by introducing a volumetric integral and scaled to the sample's level to be comparable to the experimental findings. Weight loss at a microscale level has not been studied in the literature that only focused on the oxidation thickness. Aging experiments were conducted in air and argon to monitor weight loss up to 1000 hours at both temperatures. Dark field images were taken to investigate the impact of oxidation on aged samples. Optimization utilized the generalized pattern search and artificial neural networks to accurately represent the time- and temperature-dependent proportionality parameter.

2. MATERIALS, MANUFACTURING AND THERMAL AGING EXPERIMENTS

Composite laminates were manufactured using IM7G/AR4550, a unidirectional BMI prepreg system from Aldila Composite Materials. Two sets of laminates, $[0]_{12}$ and $[0]_{16}$, were manufactured using an out-of-autoclave (OOA) prepreg process. Laminates were laid up according to the required lamination scheme and debulked under a 28-in. Hg vacuum pressure, for 30 minutes every 4 layers. The bagging scheme is shown in Figure 1. A recommended two-step cure cycle was used to cure the laminate. The temperature was first held at 143 °C for one hour in order to enhance the mobility of the reacting groups. The laminate was then cured in an oven at 191 °C for four hours. A free-standing post cure was performed at 232 °C for two hours.

Test specimens measuring 76.2 mm x 76.2 mm were cut using a low speed saw. The samples were cleaned and dried in an oven at 70 °C for 20 hours. The initial weights and dimensions were measured, and the samples were placed in a convection oven for aging. A similar procedure was followed on small samples measuring 25.4 mm x 4 mm for microscopy testing. A pressure vessel was required to conduct aging studies in argon. A cylindrical steel vessel, with a length of 50 cm and an inside diameter of 10 cm was used. Samples were placed inside the pressure vessel, which was then filled with argon such that the pressure inside the vessel was about 101 kPa at the aging temperature. Test samples were removed at regular intervals so that the weight loss could be recorded. These samples were immediately transferred to a desiccator and allowed to cool to room temperature prior to measurements. Sample mass was measured using a high-precision balance with a least count of 0.1 mg.

3. THERMO-OXIDATION MODELING AND FEA IMPLEMENTATION

Thermo-oxidation of a polymer matrix is associated with oxygen diffusion and reaction based on the three-zone model shown in Figure 2. The unoxidized material has an oxidation state variable, ϕ, equal to 1. Due to thermo-oxidation, the oxidation front advances gradually into the unoxidized material. When the polymer is completely oxidized, ϕ equals φ_{ox}. The active oxidation zone shown in Figure 2 is the reaction zone where the value of φ lies in the range $\varphi_{ox} \leq \varphi \leq 1$. A time-dependent oxidation state variable, $\varphi(t)$, was introduced to account for transient oxidation. This model has been used to study the thermo-oxidation of a neat polymer as well as polymer matrix composites [1, 8, 9].

3.1 LAMINA SCALE HOMOGENIZATION

An RVE was chosen such that the spatial distribution of fibers in the matrix maintained the same fiber volume fraction as that of the composite. In this work, a hexagonal packing unit cell geometry was used to model thermo-oxidation. The periodic RVEs of the hexagonal unit cell are shown in Figure 3. An averaging method was used in the homogenization of the diffusion-reaction properties to model thermo-oxidation as described below. Because the fiber volume fraction of the current laminate was 57.66 %, the same ratio was considered in building the unit cell and the RVE geometry. The RVE geometry consisted of two fiber quarters centered at two opposite corners of a rectangular matrix with dimensions of 3.14 µm x 5.43 µm x 135 µm as shown in Figure 4. The RVE geometry was scaled to a unit volume prior to homogenization. Lamina effective diffusivity

can be estimated using an averaging method by solving a steady-state simulation for a unit

RVE in the longitudinal direction [8].

Homogenized diffusivities in the transverse x- and y-directions were determined by

running two more simulations with a concentration gradient in the transverse directions

using the same procedure.

3.2 LAMINA SCALE MODELING OF THERMO-OXIDATION

By introducing the homogenized properties of a lamina, Fick's second law of

diffusion with a reaction term, $R_{eff}(C, \varphi^{eff})$, and time dependent oxidation state variable, φ

(t), can be represented as the following equations:

$$\frac{\partial C(x,y,z,t)}{\partial t} = \bar{\nabla} \cdot (D_{eff}(\phi^{eff})\bar{\nabla}C(x,y,z,t)) - R_{eff}(C,\phi^{eff}) \tag{1}$$

$$\frac{d\varphi^{eff}}{dt} = -\alpha(t,T)R_{eff}(C,\varphi^{eff}) \tag{2}$$

where $\alpha(t,T)$ is a fitted proportionality equation depending on time and temperature. The

temperature dependence was assumed to be linear to account for isothermal oxidation at

different temperatures. The following form of the time- and temperature-dependent

proportionality equation was proposed:

$$\alpha(t,T) = (AT + B)C \times exp((AT + B)Ct) \tag{3}$$

where *A*, *B*, *C*, and *D* are experimental fitted parameters. The determination of these

parameters is discussed in Section 3.6. The unit of the temperature in the later equation is

Kelvin throughout the whole numerical calculations. The validity of the proportionality

equation and its respective parameters is limited to the time/temperature range of the

current work. Assuming that the fiber was unoxidized during thermo-oxidation, the homogenization of diffusivity and reaction term can be obtained using the rule of mixtures [10]:

$$D_{eff}(\varphi^{eff},T) = D_{eff}{}^{un}(T)\{\frac{\varphi^{eff}-\varphi^{eff}_{ox}}{1-\varphi^{eff}_{ox}}\} + D^{ox}(T)\{\frac{1-\varphi^{eff}}{1-\varphi^{eff}_{ox}}\} \tag{4}$$

$$R_{eff}(C,\phi^{eff},T) = R_0^{eff}(T)\{\frac{\phi-\phi^{eff}_{ox}}{1-\phi^{eff}_{ox}}\}[\frac{2\beta C}{1+\beta C}(1-\frac{\beta C}{2(1+\beta C)})] \tag{5}$$

$$R_0^{eff}(T) = V_m R_0^m(T) \tag{6}$$

$$\varphi^{eff}_{ox} = \varphi^m_{ox}(1-V_f) + V_f \varphi^f_{ox} \tag{7}$$

where $D_{eff}{}^{un}$ and D^{ox} represent the Arrhenius forms of unoxidized and oxidized matrix effective diffusivity [7], respectively. The rule of mixtures was applied to the reaction rate constant, $R_0^m(T)$, and the oxidation state variable, φ^m_{ox}, of the matrix. As the fiber was assumed to be unoxidized, φ^f_{ox} is equal to unity.

Weight loss at any time increment, $W(t)$, of completely oxidized and active zones was determined by volume integration over the matrix domain. The weight loss integral was derived from the definition of the oxidation state variable, $\varphi(t)$, which is the instantaneous weight, $W(t)$, divided by the original weight, W_0:

$$\varphi(t) = \frac{W(t)}{W_0}$$

Weight loss as a function of time can be written as the difference between the initial weight and the instantaneous weight:

$$W_{loss}(t) = W_0 - W(t)$$

Substituting for $\varphi(t)$ from the definition above yields:

$$W_{loss}(t) = W_0(1 - \varphi(t))$$

The following integral was introduced for weight loss due to oxidation by considering an infinitesimal homogenized element of volume $dv = dxdydz$ undergoing thermal oxidation:

$$W_{loss}(t) = \rho_o \iiint_{matrix} (1 - \varphi)dv \tag{8}$$

where ρ_0 is the density of the unoxidized polymer matrix calculated from the unoxidized composite density (ρ_c). This integral was implemented in COMSOL [12] by post-processing the derived values over the matrix domain.

The concentration boundary condition was determined using Henry's Law:

$$C\big|_b = S \times P \tag{9}$$

Solubility, S, is a temperature-independent parameter $S = 3.61 \times 10^{-4}$ mol/m$^3 \cdot$Pa for BMI. Oxygen partial pressure, P, was calculated as 0.21 of the air pressure at the aging temperature. Unless specified, all simulation parameters were obtained from references [9, 11] and are listed in Table 1.

3.3 FEA IMPLEMENTATION OF THERMO-OXIDATION

Thermo-oxidation behavior is dependent on fiber, matrix, and fiber-matrix interface and their respective directional properties. The current study assumes localized oxidation on orthotropic RVE with no interaction in the perpendicular directions. This assumption does not correspond to oxidation at corners where interaction is present. However, the corner effect was assumed to be insignificant. It was also assumed that the localized oxidation reduced computational time where separate orthotropic simulations have been run in the longitudinal z-direction and transverse x- and y-directions.

Diffusion-reaction and oxidation rate equations were simulated using a system of two coefficient form partial differential equations (PDE). The system of fiber domain was solved by defining a zero rate of $\varphi(t)$ while, in matrix domain system, the rate was defined as discussed in Section 3.2. The time-dependent solver of generalized-α was selected for its accuracy, which is recommended for transport phenomena problems. During early simulations, oscillations in $\varphi(t)$ were persistent especially at the fiber-matrix interface. The variable $\varphi(t)$ was controlled throughout the solution by imposing two conditions to insure that the range $\varphi_{ox} \leq \varphi \leq 1$ was not exceeded. With this definition, the spurious oscillations were minimized at the fiber-matrix interface without having any convergence problems. Weight loss integrals were only calculated over the matrix domain that cut the effect of oscillation of the fiber domain. FEA simulations are mesh-sensitive for element type, size, and bias. Unstructured mesh was created by sweeping triangular-element-based face meshes with a predefined distribution biased towards oxidation exposed faces. Element distribution was also imposed on the fiber arcs and boundaries to have fine mesh where sharp gradients of $\varphi(t)$ were expected. The meshing strategy of FEA simulations was shown to damp numerical oscillations where the fiber and matrix intersect. Figure 5 shows the mesh strategy for longitudinal and transverse simulations.

Due to orthotropic RVE diffusivity, the transient diffusion-reaction and weight loss rate behavior were orthotropic. Prior to optimization, FEA meshes were thickness scaled in the z-dimension to 0.157 μm to save computational time. Only the oxidation-exposed surface, depicted in Figure 5, was assigned a constant oxygen concentration. The concentration was calculated using Henry's Law as defined in Section 3.2.

An approximate value was proposed and assigned to each parameter of the proportionality equation by running multiple oxidation simulations in longitudinal and transverse directions. First, the value of $(AT + B)$ was assumed unity at 200 °C. Then, FEA simulations were conducted at 200 °C using the estimated values of $C = 4.5 \times 10^{-5}$ and D =7.5×10^{-7}. The same values of C and D were used in the simulations at 176.67 °C. The value of $(AT + B)$ at 176.67 °C was estimated to be 0.35. Then, A and B were determined by least squares fitting of points (0.35, 449.67) and (1,473). Approximate values of A and B were 0.02786 and -12.1783, respectively.

The RVE's weight loss was scaled by the respective face area ratio of the sample to RVE. In all cases, the sample's face area was based on initial measurements in longitudinal and transverse simulations:

$$W_{loss} = W_{loss}^r(x) \times \frac{A_x^s}{A_x^r} + W_{loss}^r(y) \times \frac{A_y^s}{A_y^r} + W_{loss}^r(z) \times \frac{A_z^s}{A_z^r} \qquad (10)$$

where W_{loss} is the total weight loss in the sample's scale; $W_{loss}^r(x)$, $W_{loss}^r(y)$ and $W_{loss}^r(z)$ are the weight loss per RVE due to oxidation in x, y , and z calculated using the volume integral of Section 3.2; and A_x^s and A_x^r are the area of oxidation-exposed surfaces perpendicular to x-direction in the sample and the RVE, respectively. Similarly, A_y^s, A_z^s and A_y^r, A_z^r are the exposed surface areas in their respective scales and directions. The surface area ratio of the sample to the RVE was considered equivalent to a unique number that defines the number of RVEs in surface area. Then, A_x^s / A_x^r was equivalent to the number of RVEs in the oxidation-exposed surfaces perpendicular to x-direction. A similar definition was introduced for A_y^s / A_y^r and A_z^s / A_z^r in their respective directions. The

number of RVEs was constant as based on the initial sample's area, even though matrix

shrinkage had taken place throughout the oxidation process. The presence of cracks due to

matrix shrinkage and residual stresses had an effect on the area ratios; however, the crack

surface area was hard to measure or calculate precisely. Fitting the simulation results to

experimental results by introducing $\alpha(t,T)$ can handle the effect of the growing crack in the

surface area. Time and temperature dependence of $\alpha(t,T)$ were assumed isotropic in

longitudinal and transverse thermo-oxidation. The optimized FEA results are discussed in

Section 4.4.

3.4 ARTIFICIAL NEURAL NETWORKS (ANN) AND GENERALIZED PATTERN SEARCH (GPS) ALGORITHM OPTIMIZATION

The rate of change of the oxidation state variable, $\varphi(t)$, relative to the oxidation

rate is described by the term $\alpha(t,T)$ (Equation 3). The parameters *A, B, C,* and *D* need to be

obtained by fitting the experimental results and then optimized to reduce errors. The

procedure shown in Figure 6 was adopted to make this optimization computationally

inexpensive. Optimization of the parameters requires a large amount of input data, which

can be obtained by running 3-D unsteady FEA simulations in the longitudinal and

transverse directions. An ANN was trained, using the results from FEA, to provide input

data for optimization and reduce computational time. FEA simulations were conducted

using the approximate values of the proportionality parameter to generate input data for

ANN. In these simulations, three temperatures (176.67 °C, 188.34 °C, and 200 °C) were

used up to 1000 hours of oxidation time. Weight loss results and the simulation parameters

of time, temperature, and $\alpha(t,T)$ were used to build the ANN model. ANN predictions were used in the GPS algorithm to optimize the proportionality parameter.

3.5 BUILDING ANN MODEL USING FEA RESULTS

Generally, a network consists of three layers: an input layer, hidden layer/layers and, an output layer. ANN modeling fits the dependence of the output layer (dependent variables) to the input layer (independent variables). Flexible transfer functions are used to transfer weighted signals to the output layer where error minimization is the goal of the training algorithms by altering signal weights. Data sets are divided into training, testing, and/or validation data to check the performance of the network over unseen data. The full structure is shown in Figure 7. The input layer had three neurons corresponding to time, temperature, and $\alpha(t,T)$. Two hidden layers with 15 and 8 neurons were used with sigmoidal transfer functions. The output layer had one neuron corresponding to weight loss. The inputs to the hidden layers were weighed signals from the preceding layer. The transfer function for hidden neurons was:

$$h(j) = 1 / (1 + exp(-\sum_{i=1}^{n} x(i)w(i)))$$

(11)

where $x(i)$ is the normalized input variable; $w(i)$ is the weight; n is the number of neurons in preceding layer; $h(j)$ is the output of the hidden neuron; and j is the respective neuron number in the first hidden layer. The output of the hidden neuron $h(j)$ serves as an input signal to the next layer nodes. For the output layer, the transfer function was linear.

$$O = \sum_{i=1}^{m} H(i)W(i)$$

(12)

where $H(i)W(i)$ is the second hidden layer signal multiplied by its weights over $m = 8$ hidden nodes and O is the normalized output (weight loss). All weights were adjusted using

the Levenberg-Marquardt training algorithm to minimize the error, which is the goal of the training process.

A data set of 300 patterns was obtained from FEA simulations and used in a MATLAB code to build the network. The training error target was set to 1×10^{-9} with 1,250 maximum training epochs. Validation patterns were set to a default of 15 % of the total patterns. In this stage, the FEA weight loss results along with input parameters of time, temperature, and approximate $\alpha(t,T)$ were transferred to ANN as a training data set. The data details are listed in Table 2.

3.6 GPS OPTIMIZATION OF PROPORTIONALITY PARAMETER

The proportionality equation, $\alpha(t,T)$, was optimized using the GPS algorithm. This was done by introducing a parameter, L, into Equation 3:

$$\alpha(t,T) = LC(AT + B) \times exp(L(AT + B) \times Dt) \qquad (13)$$

The introduction of this optimization parameter was to account for time and temperature contributions in the optimization of the proportionality parameter. The goal was to find the optimum value of L that makes the objective function of mean squared error (MSE) converge. MSE was calculated as the error difference between the network predictions and the optimization data set. Optimization data was the experimental results of Section 4.1. The GPS algorithm (incorporated in MATLAB) recalls the network to predict weight loss, compares the results to the optimization data, and searches/polls for L values that minimize MSE. The optimum point that corresponds to the optimization parameter was expected to lie between the lower and upper bounds of 0.9 and 1.1. Stopping criteria tolerances of the GPS algorithm were set to 1×10^{-30} to avoid early termination and search/poll throughout

the maximum number of 2,000 iterations. Multiple start points were selected to ensure that the algorithm converges to a global minimum. All start points converged to the same optimized value.

4. RESULTS

4.1 THERMAL AGING EXPERIMENTS

Weight loss percent measurements at 200 °C and 176.67 °C as a function of aging time up to 1,000 hours are shown in Figures 8 and 9. The average weight of intact samples was 18.82 g and 13.54 g of those aged at 176.67 °C and 200 °C, respectively. The weight loss results were recorded at different temperatures and thicknesses, where 12-layer laminate was aged at 200 °C and 16-layer laminate was aged at 176.67 °C. Due to thickness differences, the results have been shown in separate graphs. A similar concept was reported in [4, 17]. Thicker samples were used for thermo-oxidation at 176.67 °C so that the weight loss was more significant and easier to measure. Thicker samples at a lower temperature had less weight loss and a lower weight loss percent than thinner samples at a higher temperature. Generally, the weight loss of samples in air was higher than the weight loss in argon. The effect of the oxidizing environment on weight loss was significant compared to the non-oxidizing gas of argon where volumetric polymer decomposition was dominant. The average contribution of oxidative weight loss was about 92 % of the total weight loss at both temperatures. These observations indicate that the major cause of weight loss is an oxidation reaction, compared to polymer decomposition. Weight loss due to polymer decomposition results from cleavage of low molecular weight chains and products of

decomposition outgas from the composite. This is the cause of weight loss under thermal aging in an argon atmosphere.

Weight loss behavior in all cases was almost linear up to the current range of aging time. The average contribution of weight loss in argon to total weight loss at 200 °C was 8 %. It was assumed that the average non-oxidative weight loss contributed similarly at 176.67 °C. The weight loss of argon-aged samples at longer aging times showed uncertainty from the linear trend, which was possibly due to a variation in the internal pressure of the vessel.

In the present study, weight loss predictions were correlated to the surface area of samples (Section 3.3). Also, the interaction between oxidation and decomposition, if any, was assumed insignificant, and the difference between weight loss in air and argon was completely due to oxidation. The superficial nature of oxidation and the accompanying volumetric polymer decomposition were reported in the literature [3, 11, 15].

Dark field microscopy was used to characterize the oxidized layer in aged samples. The oxidation-exposed area varied with aging time due to crack initiation and growth. Matrix shrinkage also altered the exposed area. However, the area was altered to a lesser extent compared to matrix cracking. Figures 10 and 12 show the dark field optical images of samples aged for 100, 500 and 1270 hours at 176.67 °C. Under the dark field, the matrix looked bright, while the oxidized "layer" seemed to be brighter. Fibers were dark, showing the oxidation penetration path through cracks. Matrix cracks at 100 hours were limited in size and number. With an increase in aging time, the size and number of cracks increased. Crack propagation was along the fiber direction. In all cases, the transverse cracking and the oxidized "layer" front were not discernible. Accordingly, quantitative measurements of

the average oxidized thickness were not taken. At longer aging times, the oxidation-exposed edge in the longitudinal direction was distorted due to oxidized matrix shrinkage and longitudinal cracking.

4.2 HOMOGENIZATION SIMULATION

For homogenized diffusivity simulation, three steady-state simulations were conducted for the scaled RVE. Symmetry boundary conditions were applied on all surfaces not exposed to the atmosphere. Exposed surfaces were assigned constant oxygen concentration boundary conditions of unit concentration difference on opposed surfaces. The homogenized diffusivity tensor was orthotropic. However orthotropic homogenized diffusivity was considered, the difference in transverse diffusivities was small. Longitudinal homogenized diffusivity was about 15 times the average transverse diffusivity. These results highly promote oxygen diffusion along fibers in the longitudinal thermo-oxidation. Carbon fiber diffusivity has been assumed as a fraction of the matrix diffusivity, listed in Table 1.

4.3 ANN AND GPS OPTIMIZATION

ANN training, testing, and validation performance are shown in Figure 13. Similar performance trends are shown over the first 19 epochs where the testing curve was just close to the validation curve, indicating an equivalent division of data and nonexistent overfitting problem. The best validation point had 3.3×10^{-9} mean squared error (MSE), which was close to the goal of 10^{-9}. Excellent predictions for all data sets were achieved with a correlation coefficient of unity between predictions and targets (FEA results).

GPS optimization of the proportionality parameter was conducted by adjusting $\alpha(t,T)$ with the factor L. In the optimization data, the function of $\alpha(t,T)$ was defined using a two-component vector of $L : L_1$ and L_2. The introduction of L_1 was to optimize the ANN simulation predictions over the experimental data at 176.67 °C. Similarly, L_2 was used to optimize predictions at 200 °C. The objective function history, MSE, over the 2,000 iterations of GPS is shown in Figure 14. The error values were scaled between 0 and 1 to represent the relative difference between data points over the iteration number. The MSE curve of GPS optimization was depicted by a two-segment plot showing the decline in scaled error as iterations proceeded. The MSE convergence curve was fluctuating at the points of both segments. However, the lower segment showed faster convergence to the optimum point that occurred at $L_1 = 1.072$ and $L_2 = 1.0121$. The final mesh size that the GPS searched/polled was 6×10^{-4} with an MSE $= 2.4\times10^{-6}$. This error reflects the difference between optimized ANN predictions and unseen experimental data.

4.4 OPTIMIZED THERMO-OXIDATION SIMULATION

The optimum values of L_1 and L_2 were used to adjust the parameters A and B. The optimized values of A and B were 0.0273 and -11.89, respectively. The values of C and D were kept the same as proposed earlier (Table 2). The MSE of predictions from the numerical model compared to ANN predictions was reduced by 3.4 % after optimization. The intensive trial and error determination of the proportionality parameter was reflected in this small error difference. This was also critical in reducing the optimization time where the optimum point was close to the polled/searched points. However, the optimized models were considered for further analysis by studying the significance of $\alpha(t,T)$.

The effect of $\alpha(t,T)$ on the oxidation behavior was investigated by sensitivity studies at 176.67 °C. The value of $\alpha(t,T)$ was increased by 5 % and 10 % while the temperature was kept constant to evaluate the effect of uncertainty in the proportionality equation. The average increase in predicted weight loss was about 5 % and 9 %, respectively, in longitudinal oxidation (Figure 15). This shows that any uncertainty in the reaction rate parameters has a significant effect on the FEA predictions of thermo-oxidation.

The weight loss predictions compared to experimental results as a function of aging time at both temperatures are shown in Figure 16. An excellent correlation was achieved between the simulation and experimental results with $R^2 = 0.9963$. It was reported in the literature that the initial weight loss rate was unexpectedly higher during early aging times up to 200 hours without a direct correlation to diffusion and/or reaction mechanism [1, 7, 16]. However, in the present work, this kind of behavior was not significant.

4.5 RVE-SCALE AND SAMPLE-SCALE RESULTS

The spatial distribution of the oxidation state variable, $\varphi(t)$, and the weight loss per unit volume at 200 °C after 1,000 hours of oxidation are shown in Figure 17. The weight loss per unit volume was zero at the fiber domain and the unoxidized matrix where the oxidation state variable was unity, which was defined in Equation 8. The weight loss per unit volume was 0.44 mg/µm^3 for the oxidized matrix that was considered to be a characteristic index of the completely oxidized matrix. The weight loss per unit volume plots also follow the three-zone model that was described for thermo-oxidation. The oxidized layer thickness in the longitudinal and transverse directions, at the RVE scale, is

shown in Figures 18 and 19. The growth of oxidized layer thickness with time in transverse x and y exhibited a similar trend at 176.67 °C as well as 200 °C. The degree of non-linearity was higher at 200 °C compared to 176.67 °C in all directions where the cracking effect was more significant. With an increase in aging temperature and time, the rate of oxidation growth increased. This was also affected by increased cracking. The oxidized layer thickness in the longitudinal direction was 3 and 2.5 times the average thickness in the transverse directions at 176.67 °C and 200 °C, respectively. This was attributed to the fact that the longitudinal diffusivity was 15 times the average transverse diffusivity. This behavior was valid throughout the aging hours as the diffusivity increased isotropically due to oxidation (Section 3.2). This reflected the direct dependence of oxidized thickness on diffusivity, resulting in a higher degree of anisotropic oxidation thickness. The growth of oxidized thickness reached a constant rate at 176.67 °C for longer aging times. The oxidized thickness growth, in the longitudinal direction, was higher at early aging times up to 200 hours at both temperatures. The effect of longitudinal cracking during early aging times was a possible reason behind this trend as dark field microscopy did not reveal a discernable transverse cracking.

The weight loss % predictions in the longitudinal and transverse directions, at the RVE scale, are shown in Figures 20 and 21. The transverse weight loss % in x and y were distinctively different, showing higher predictions in the former. The weight loss % in the transverse directions at both temperatures was significant compared to the weight loss % in the longitudinal direction in RVE level. The homogenized diffusivity in x- and z-directions was respectively 20 and 1.7 times the diffusivity in the y-direction, again throughout the whole aging process. However, the weight loss % results did not follow the

same diffusivity proportion/dependence where the weight loss % in x- and z-directions was respectively 4.5 and 3 times the weight loss % in the y-direction. The weight loss % rate and the degree of non-linearity exhibited similar behaviors at both temperatures in all directions.

At the sample scale, components of the weight loss % of the *x*, *y*, and *z* directional terms in Equation 10 are shown in Figures 22 and 23. However, the contribution of the weight loss % in the transverse directions was higher at the sample's scale at both temperatures. In this case, the weight loss % in the y-direction was the highest, exceeding 90 % of the total. It was the effect of the area ratios that made the contribution of the weight loss % higher in the transverse directions where the significance was limited to numerical calculations. All trends showed a linear dependence of weight loss % on time for the current aging hours.

5. CONCLUSIONS

Thermo-oxidative aging of OOA cured carbon BMI laminates was investigated at the operating temperature range of BMI systems, 176.67 °C (350 °F) and 200 °C (392 °F). The validity of the present work is limited to the time/temperature range discussed in the body of the paper. This work was dedicated to study the diffusion-limited regime of the thermal oxidation where oxygen excess case was not considered. Micromechanical modeling was conducted using 3-D FEA for the approximate and optimized proportionality parameters. Optimized parameters were introduced to account for the temperature dependence of the proportionality function. Due to thickness differences, the weight loss

% in air at 200 °C (392 °F) was not directly comparable to the weight loss % at 176.67 °C (350 °F). However, both were seemingly stemming from 92 % oxidative aging. The longitudinal homogenized diffusivity determined by averaging was 15 times the diffusivity in the transverse directions where the difference of transverse diffusivity was insignificant. However, the transverse diffusivity values were close, there was anisotropic increase in the oxidized layer thickness and the weight loss % at the RVE level at both temperatures. The anisotropic growth in the oxidized layer was more significant, showing sparse trends in the longitudinal and transverse cases. A higher degree of non-linearity was shown at 200 °C (392 °F) for the oxidized layer thickness, raising the contribution of cracking in creating a larger surface area. A novel index was presented that corresponds to the weight loss per unit volume of the completely oxidized matrix. The analysis of thermo-oxidation behavior at the RVE level was more realistic, reflecting the diffusion-reaction mechanisms rather than incorporating the effect of area ratios as it was shown in the sample level. By simulation, the initial high rate of oxidized layer growth was markedly shown at both temperatures in the longitudinal direction; however, weight loss % predictions did not show a remarkable initial weight loss % rate in all directions. In either case, this work assumes the possibility of fitting the FEA weight loss predictions to experimental data to attain models that predict the oxidized layer growth behavior sufficiently.
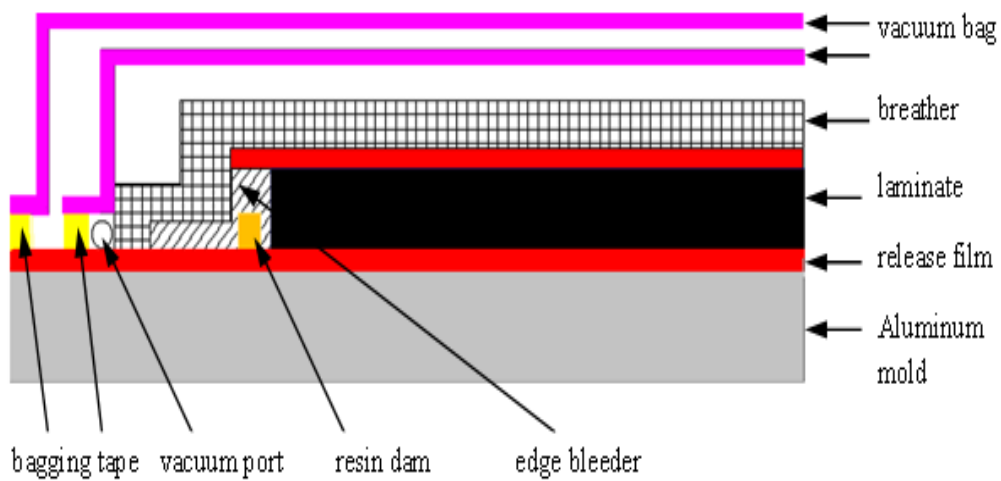
Figure 1. OOA process bagging assembly with edge bleeder
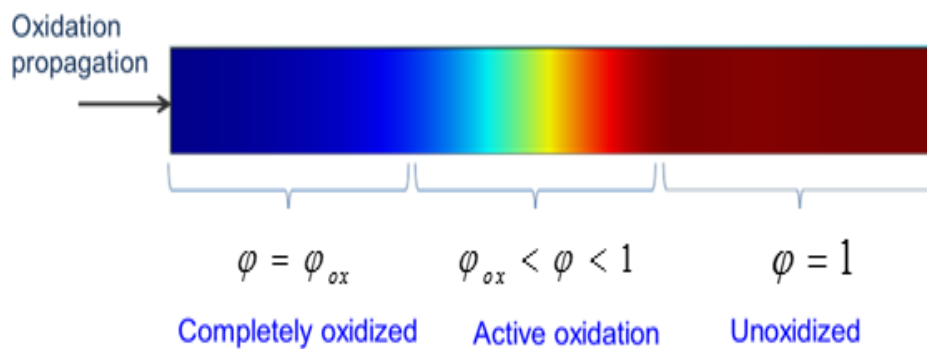
Figure 2. Three-zone oxidation model
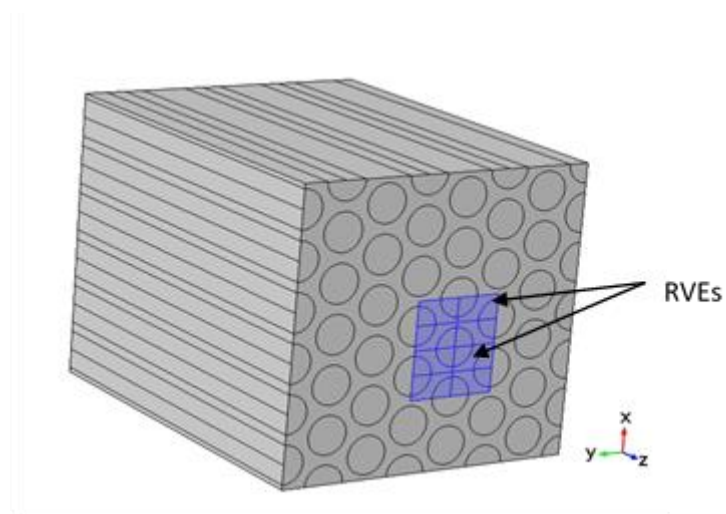
Figure 3. Hexagonal packing unit cell and RVE geometry
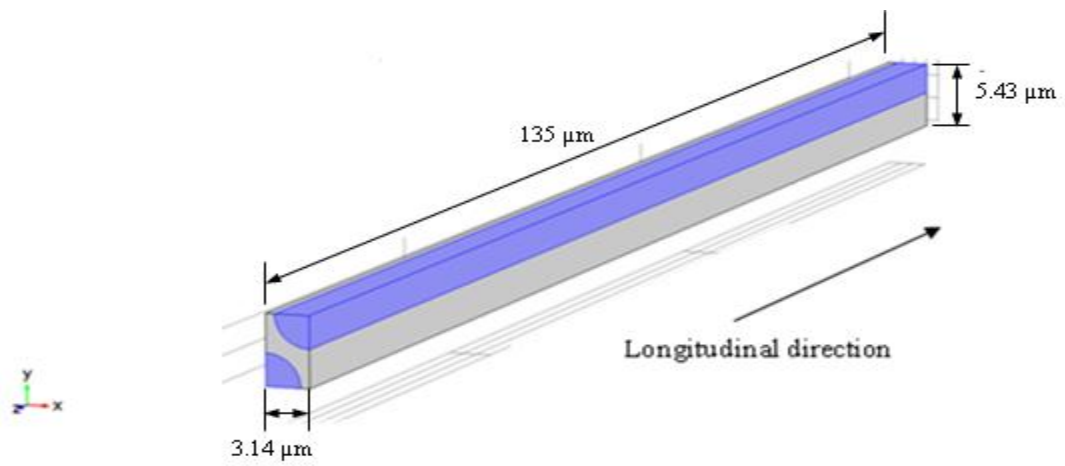
Figure 4. RVE geometry and direction notation (fibers are highlighted)
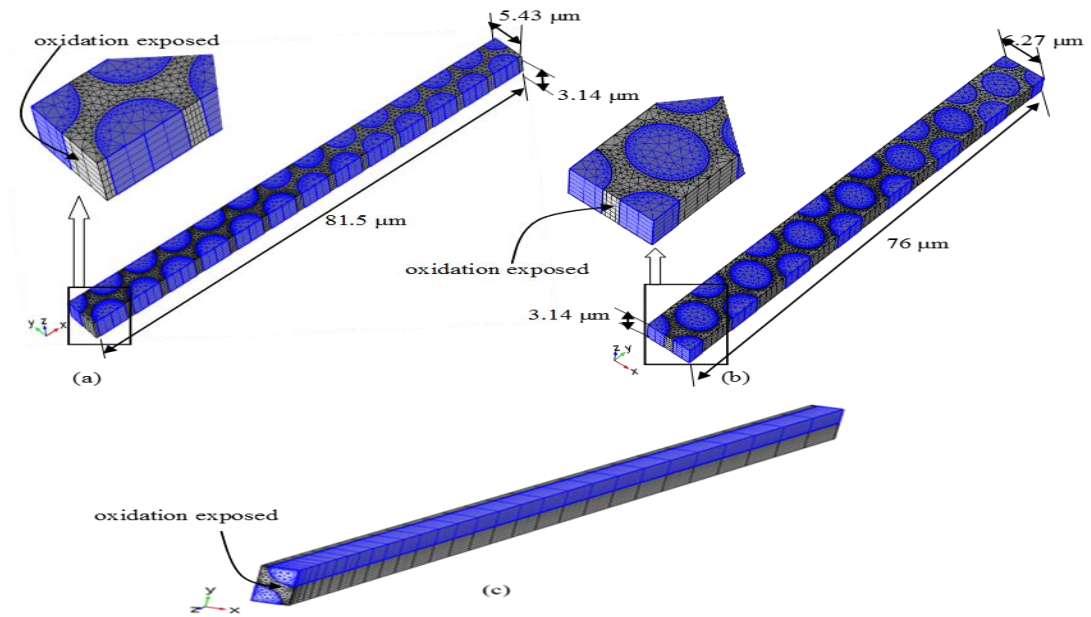
Figure 5. Mesh strategy for transverse and longitudinal thermo-oxidation
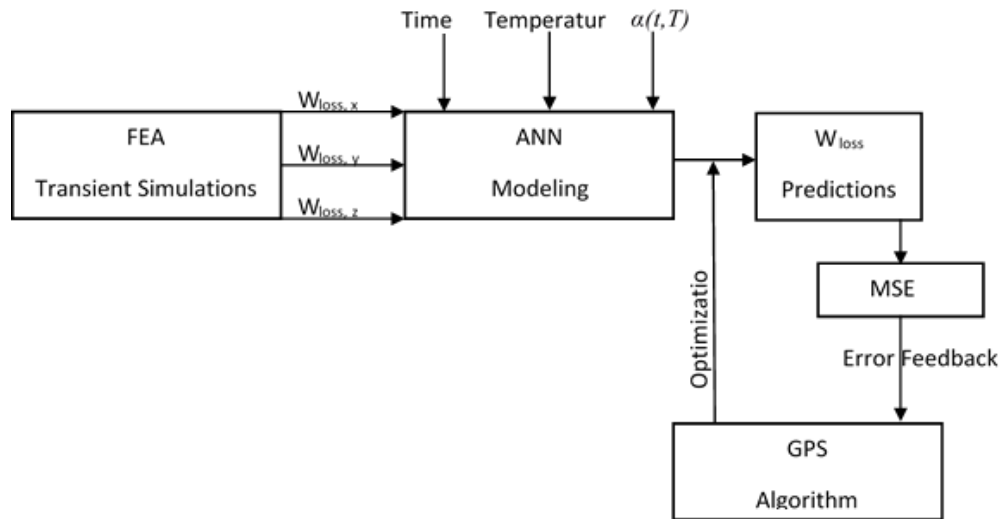
Figure 6. Thermo-oxidation parameter optimization procedure
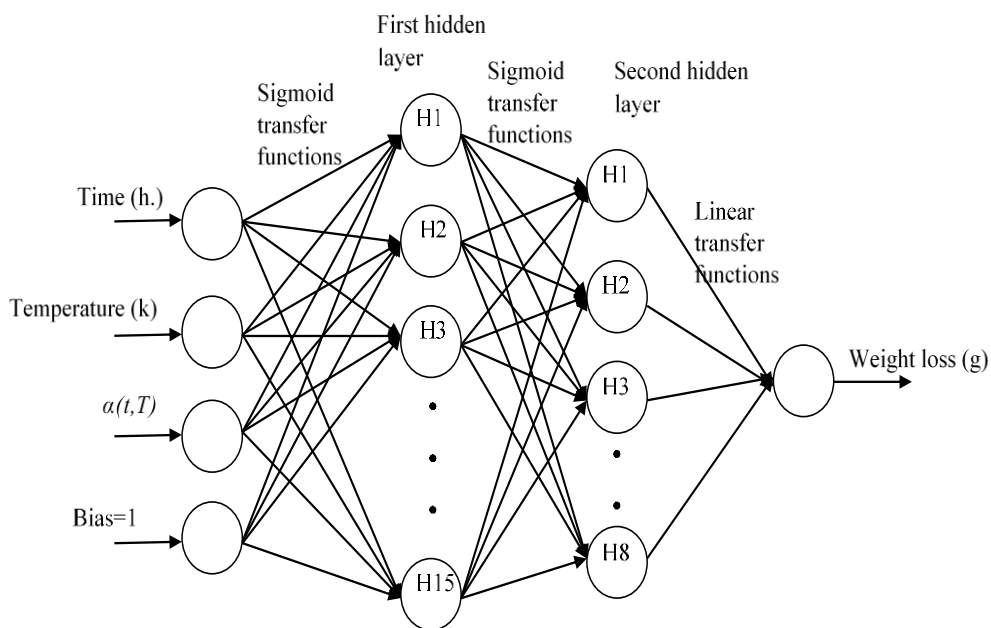
Figure 7. Multi-input, single output ANN architecture
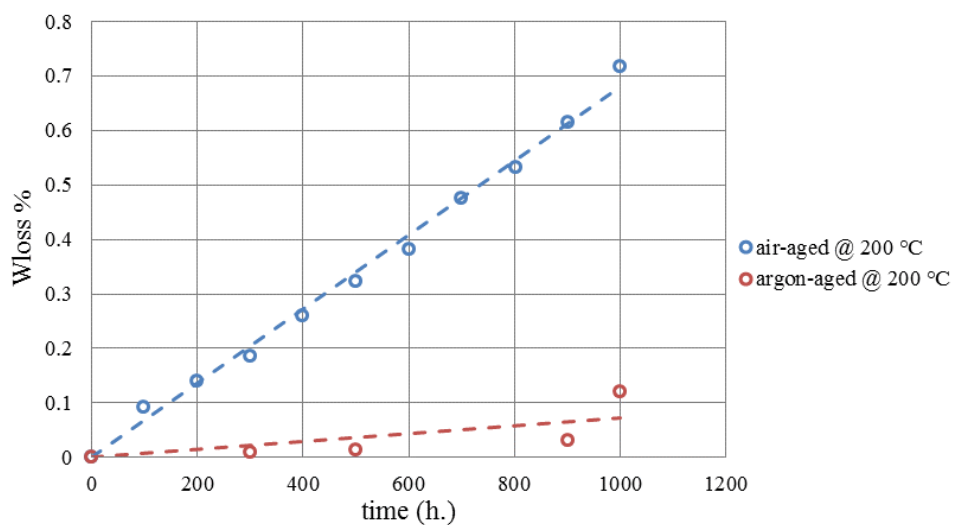
Figure 8. Weight loss % of 12-layer samples aged at 200 °C
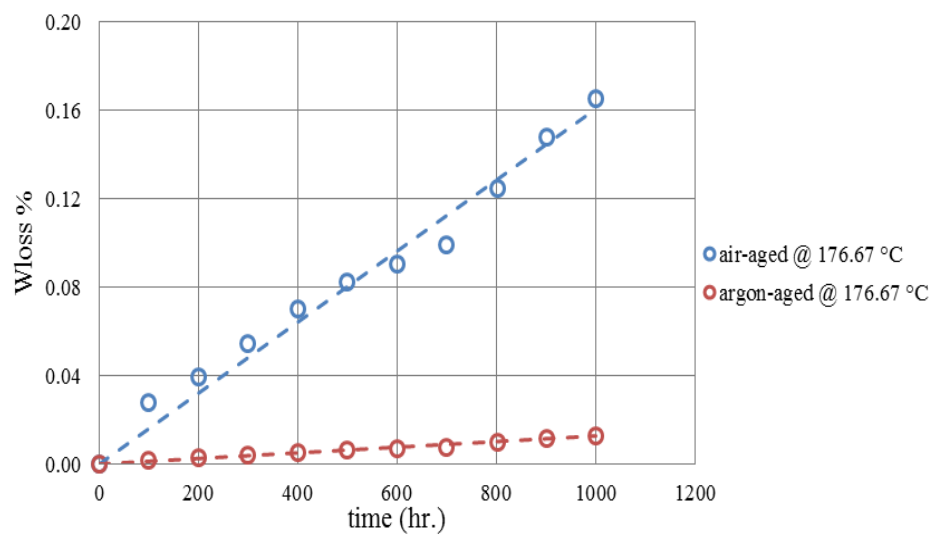
Figure 9. Weight loss % of 16-layer samples aged at 176.67 °C
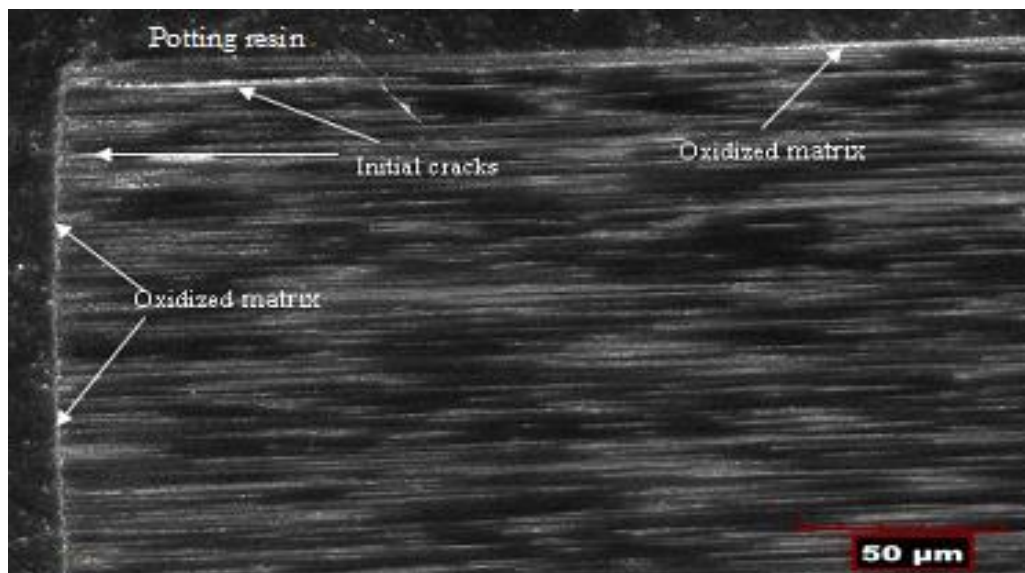
Figure 10. Dark field image of a sample aged for 100 hours
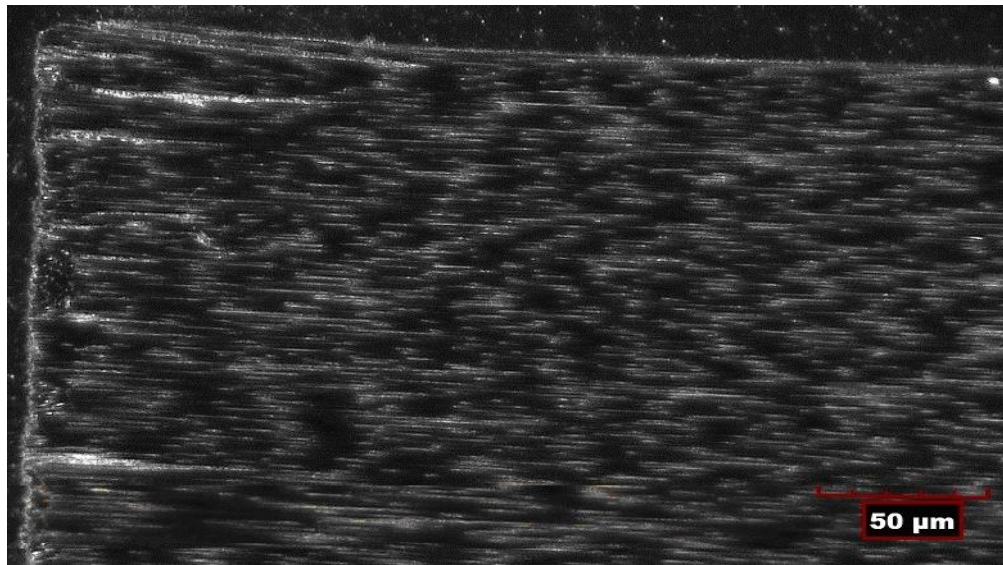
Figure 11. Dark field image of a sample aged for 500 hours
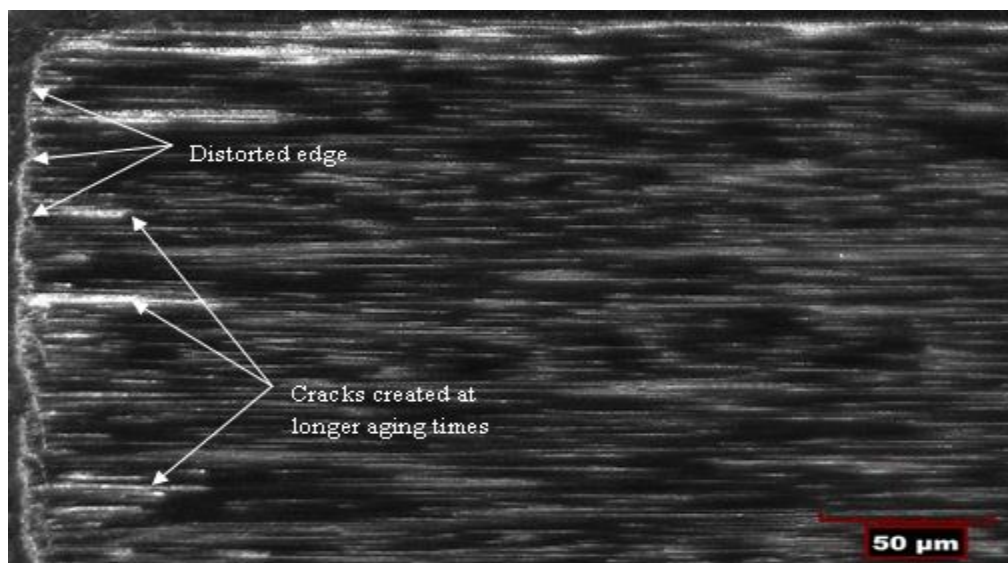
Figure 12. Dark field image of a sample aged for 1270 hours
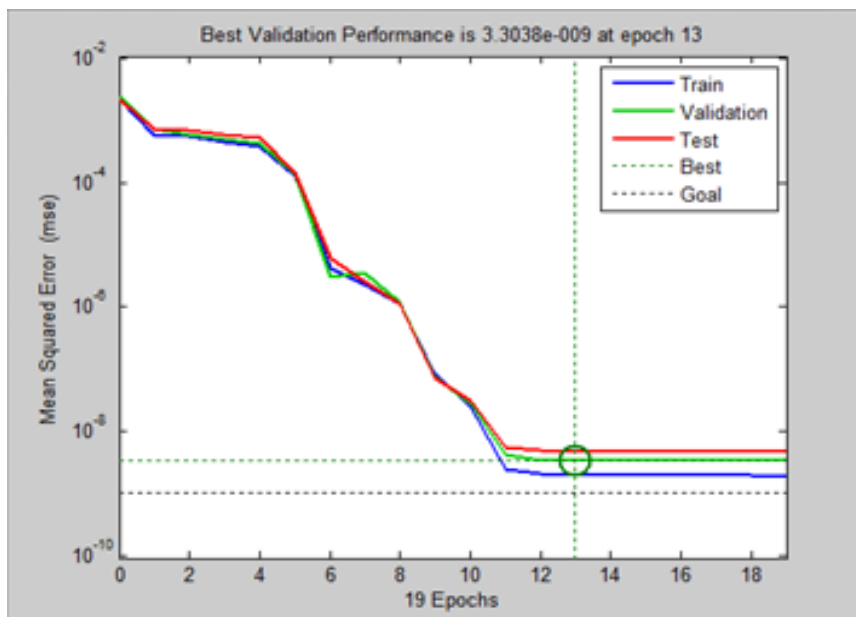
Figure 13. ANN performance curves
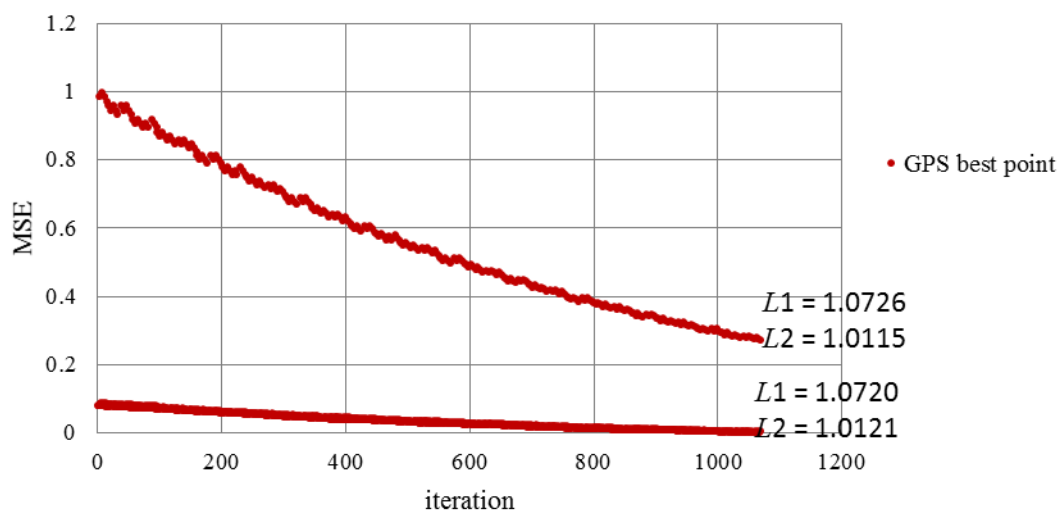
Figure 14. GPS performance curve
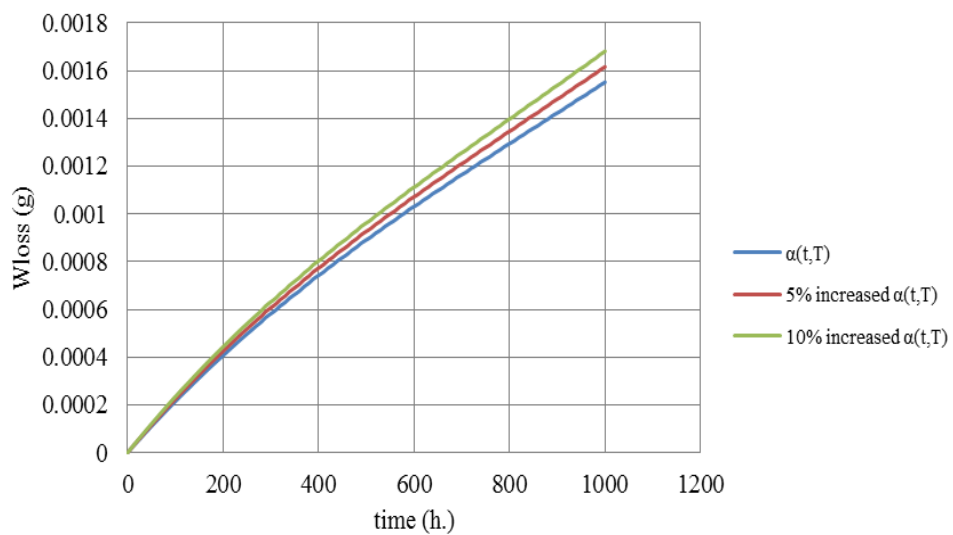
Figure 15. Uncertainty in proportionality parameter
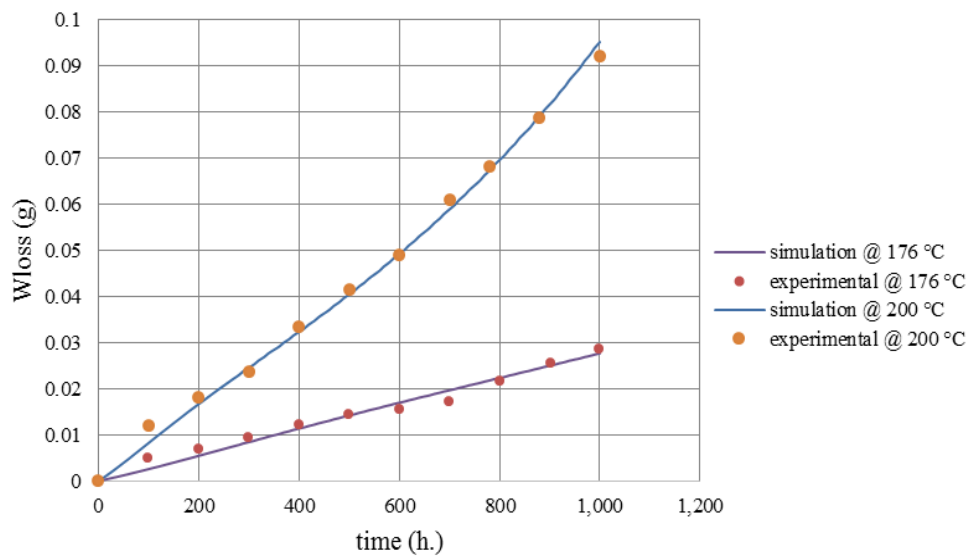
Figure 16. FEA versus experimental results as a function of aging time
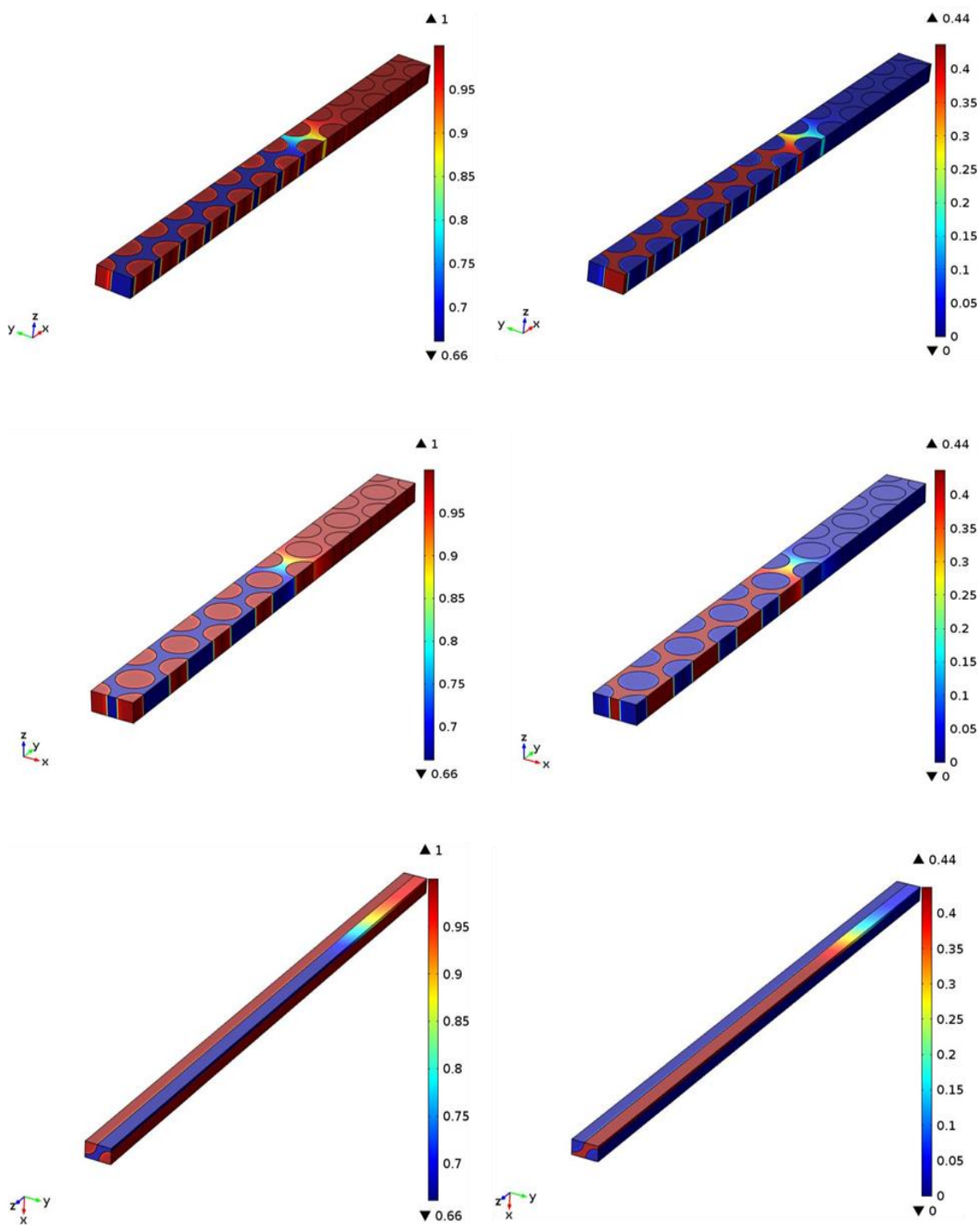
Figure 17. Oxidation state variable (left) and weight loss (right)
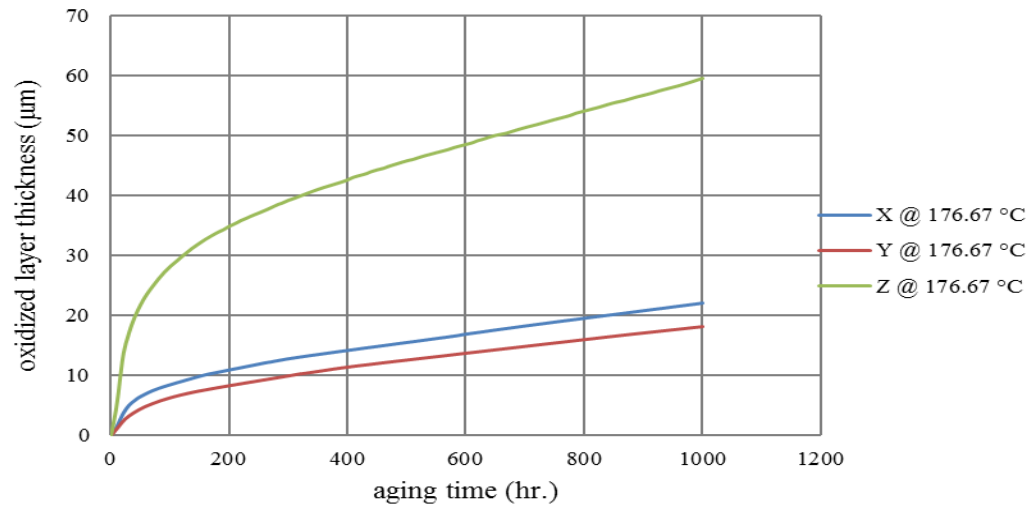
Figure 18. Thickness of oxidized layer at 176.67 °C vs. aging time
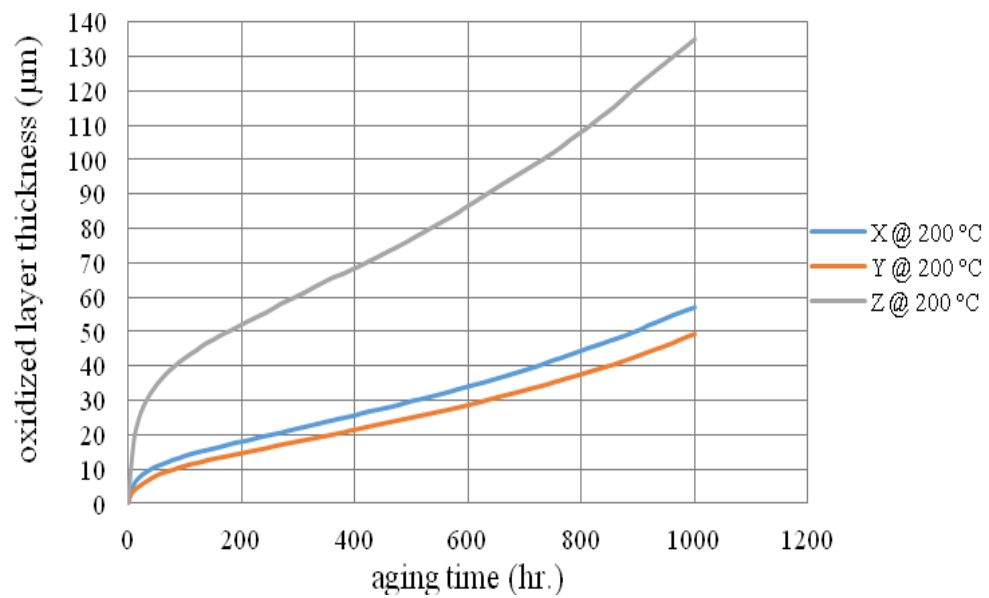
Figure 19. Thickness of oxidized layer at 200 °C vs. aging time
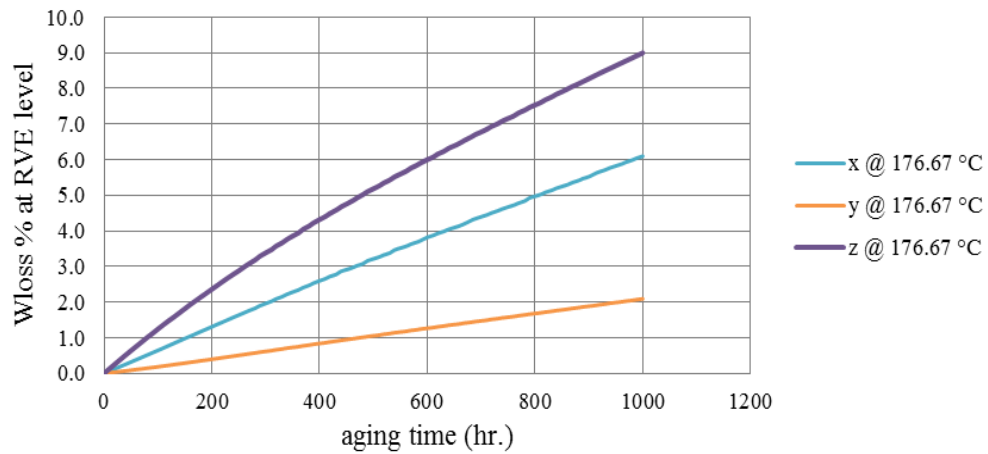
Figure 20. RVE-based weight loss % predictions at 176.67 °C vs. aging time
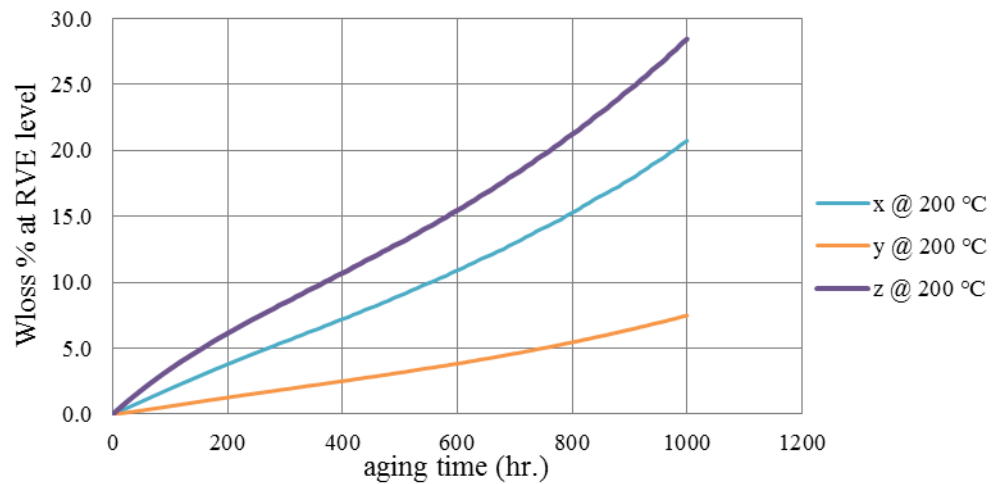
Figure 21. RVE-based weight loss % predictions at 200 °C vs. aging time
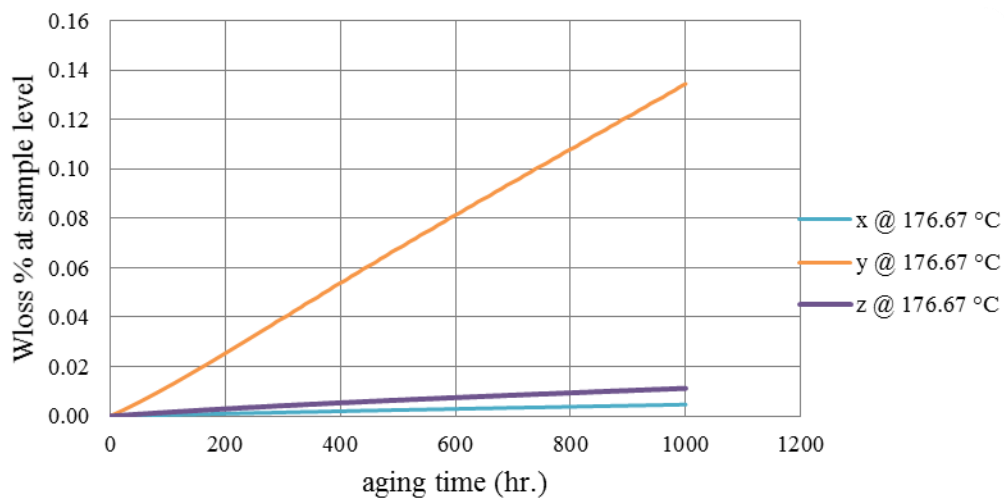
Figure 22. Weight loss % predictions at sample level vs. aging time
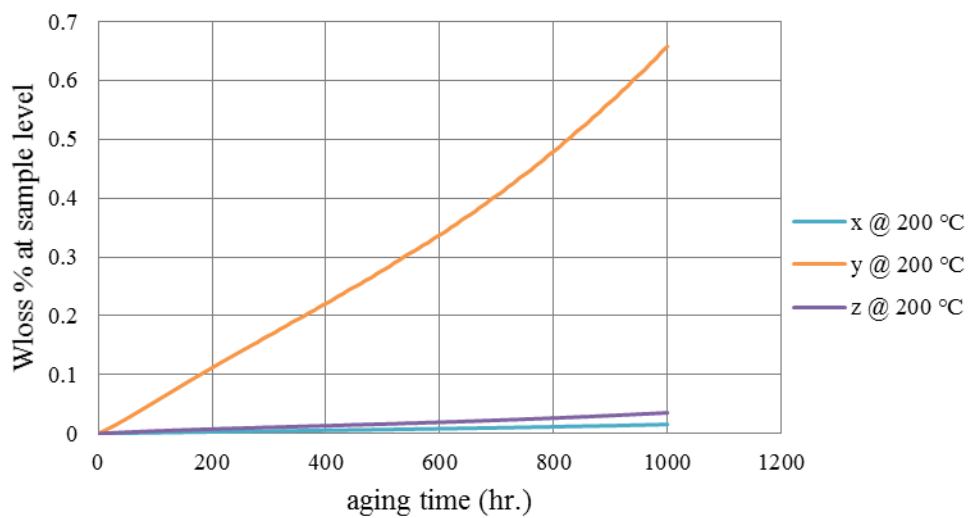
Figure 23. Weight loss % predictions at sample level vs. of aging time

Table 1. Parameters used in diffusion-reaction and weight loss simulation

Parameter	Symbol	Value
Diffusivity of the unoxidized matrix ($\varphi=1$)	D_0^{un}	1.62×10^{-4} mm^2/min
Diffusivity of the oxidized matrix ($\varphi=\varphi_{ox}$)	D_0^{ox}	1.94×10^{-4} mm^2/min
Longitudinal fiber diffusivity	D_L^f	$D_0^{un}/10^3$
Transverse fiber diffusivity	D_T^f	$D_0^{un}/10^5$
Density of laminate [*]	ρ_c	1.57 g/cm^3
Density of unoxidized polymer matrix [**]	ρ_o	1.24 g/cm^3
Fiber weight fraction[***]	W_f	65.3%
Density of fiber	ρ_f	1.78 g/cm^3
Fiber volume fraction[**]	v_f	57.66 %
Temperature dependence parameters [§]	A,B	0.0273, -11.89
Time dependence parameters [§]	C,D	4.5×10^{-5}, 7.5×10^{-7}
Homogenized longitudinal-z diffusivity[†]	D_Z^{eff}	6.86×10^{-4} mm^2/min
Homogenized transverse-x diffusivity[†]	D_X^{eff}	5.69×10^{-5} mm^2/min
Homogenized transverse-y diffusivity[†]	D_Y^{eff}	3.29×10^{-5} mm^2/min

[*] determined experimentally by water displacement according to ASTM D792 [13]   [§] equation (3)   [†] Section 4.2

[**] determined using calculation methods of ASTM D3171 [14]   [***]manufacturer's data sheet

Table 2. Network training data details

Input/output	Minimum	Maximum
Time (hr.)	0	1,000
Temperature (°C)	177.67	200
$\alpha(t,T)$ [**]	1.575×10^{-5} (t = 0,T=177.67°C)	6.695×10^{-4} (t=1,000,T=200°C)
Weight loss (g)	4.62×10^{-17}[*] (t= 0,T=177.67°C)	0.09423 (t =1,000,T=200°C)

[*] This value should be zero which reflects the FEA error   [**] Approximate function values

REFERENCES

1) Schoeppner, G.A., Tandon, G.P. and Pochiraju, K.V. Multiscale Modeling and Simulation of Composite Materials and Structures. Springer. 2008.

2) Boyd, J., Bongiovanni, C.L. and Thai, B. "Bismaleimide Resin with High Temperature Thermal Stability." U.S. Patent 2007/0117956 A1, May 24, 2007.

3) Decelle, J., Huet, N. and Bellenger, V. "Oxidation Induced Shrinkage for Thermally Aged Epoxy Networks." Polymer Degradation and Stability 81 (2003): 239–248.

4) Schoeppner, G.A., Tandon, G.P. and Ripberger, E.R. "Anisotropic Oxidation and Weight Loss in PMR-15 Composites." Composites: Part A 38 (2007): 890–904.

5) Bellenger, V., Decelle, J. and Huet, N. "Ageing of a carbon epoxy composite for aeronautic applications." Composites: Part B 36 (2005): 189–194.

6) Kung, H-K. "Effects of Surface Roughness on High-temperature Oxidation of Carbon-Fiber-Reinforced Polyimide Composites." Journal of Composite Materials 39 (2005): 1677–1687.

7) Chung, K., Seferis, J.C. and Nam, J.D. "Investigation of Thermal Degradation Behavior of Polymeric Composites: Prediction of Thermal Cycling Effect from Isothermal Data." Composites: Part A 31 (2000): 945–957.

8) Pochiraju, K.V., Tandon, G.P. and Schoeppner, G.A. "Evolution of Stress and Deformations in High-Temperature Polymer Matrix Composites During Thermo-oxidative Aging." Mechanics of Time-Dependent Materials 12 (2008): 45–68.

9) Antoun, B., Qi, H.J., Hall, R., Tandon, G.P., Lu, H., Lu, C., Furmanski, J. and Amirkhizi, A. Challenges in Mechanics of Time-Dependent Materials and Processes in Conventional and Multifunctional Materials, Volume 2. Springer. 2014.

10) Varghese, J. and Whitcomb, J. "Micromechanics of Oxidation in Composites with Impermeable Fibers." Journal of Composite Materials 43(2009):2011-2043.

11) Colin, X., Marais, C. and Verdu, J. "Thermal Oxidation Kinetics for a Poly (bismaleimide)." Journal of Applied Polymer Science 82(2001):3418–3430.

12) COMSOL Inc. Coefficient Form Partial Differential Equation (PDE) Module. Version 5.0.1.276.

13) ASTM Standard D792 − 13, 2013, "Standard Test Methods for Density and Specific Gravity (Relative Density) of Plastics by Displacement" ASTM International, West Conshohocken, PA, 2013, DOI: 10.1520/D0792-13, www.astm.org.

14) ASTM Standard D3171 − 11, 2011, "Standard Test Methods for Constituent Content of Composite Materials" ASTM International, West Conshohocken, PA, 2011, DOI: 10.1520/D3171-11, www.astm.org.

15) Gigliotti, M., Olivier, L., Vu, Dinh, Q. and Grandidier, J. "Local Shrinkage and Stress Induced by Thermo-Oxidation in Composite Materials at High Temperatures." Journal of the Mechanics and Physics of Solids 59 (2011): 696–712.

16) Lafarie-Frenot, M.C. "Damage Mechanisms Induced by Cyclic Ply-Stresses in Carbon–Epoxy Laminates: Environmental Effects." International Journal of Fatigue 28 (2006): 1202–1216.

17) Bowels, K.J., McCorkle, L. and Ingraham, L. "Comparison of Graphite-Fabric-Reinforced PMR-15 and Avimid N Composites after Long-Term Isothermal Aging at Various Temperatures" NASA TM 113116/REV1, 1998.

II. MULTI-SCALE MODELING OF THERMO-OXIDATION EFFECTS ON THE FLEXURAL BEHAVIOR OF CROSS-PLY BISMALEIMIDE COMPOSITES

Rafid M. Hussein, Sudharshan Anandan, Gurjot S. Dhaliwal and K. Chandrashekhara

Department of Mechanical and Aerospace Engineering

Missouri University of Science and Technology, Rolla, MO 65409

ABSTRACT

The present work investigates the oxidative aging damage of cross-ply bismaleimide composites. Micro/macro-scale thermo-oxidation behavior and flexural failure were simulated for 1,700 hours of aging. Thermo-oxidation behavior of the cross-ply laminates was modeled using a multi-fiber multi-layer representative volume element. Thermo-oxidation is a diffusion-reaction phenomenon that depends on temperature and oxidation state. The proportionality between oxidation state evolution and reaction rate was modeled using a new form of time-dependent parameter. A novel damage state was presented assuming a proportionality between the homogenized weight loss ratio per lamina and the elastic property reduction. Scanning electron micrographs showed that the onset of the "blunt" transverse (through-thickness) micro-cracking/debonding in the superficial layers was at 500 hours under 176.67 °C (350 °F). After about 1,700 hours of aging, the weight loss ratio was 0.5 % and the flexural modulus reduced by 19 %. Prior to 500 hours, where cracking was not noticeable in the "crack-free region", the strengths

reduction was not significant based on the numerical simulations. In the crack-free and oxidative damage dominated regions, elastic property numerical reduction was significant.

1. INTRODUCTION

Currently used design methodologies for high temperature composite structures rely on the reduction of the mechanical properties of the lamina to account for the severe environmental effects. Properties such as laminates' ultimate strength, notched strength and flexural strength are critical. Thermo-oxidation mainly affects the matrix-dominated properties of polymer composites namely the transverse and shear properties [1]. Polyimides and bismaleimides (BMIs) are commonly used high-temperature resins for aerospace applications. BMIs, due to their thermal stability at high temperatures and ease of manufacturing are a good alternative to epoxies and polyimides for extended use under severe environments [2].

Many researchers studied thermo-oxidation behavior of high temperature resins such as BMI, PETI-5 and PMR-15. The weight loss and oxidized layer thickness were modeled and characterized [3-5]. However, few researchers investigated the effects of thermo-oxidation on the mechanical properties. These investigations were also limited to specific problems like elastic constants and flexural stiffness degradation for unidirectional laminates. Roy et al. [6, 7] used continuum damage mechanics (CDM) analysis of a pre-existing fiber/matrix debond to model the damage evolution due to oxygen diffusion. The analysis was based on the introduction of a damage parameter that contributed to a reduction in the in-plane elastic constants. The effective bending stiffness was shown to

depend on the reduced elastic properties. Matrix debond analytical results showed a significant effect when the debond length to RVE span ratio reached 15 % in a 2D flexural sample. Upadhyaya et al. [8] investigated the long-term degradation in the inter-laminar strength of unidirectional IM-7/PETI-5 laminates subjected to oxidation at 300 °C up to 2,000 hours. An internal state variable (ISV) was used to account for the molecular oxidation damage. The experimental work included shear creep and three-point bending tests of aged and virgin replicates. It was assumed that the total diffused oxygen in to the polymer consists of a mobile phase and a bound phase. Diffusion-reaction modeling was implemented for the mobile part of oxygen while the bound part of oxygen was modeled using time integration of the reaction term for the mobile part. The local shear model predictions for the cohesive layer showed a significant decrease of 73 % and 68 % in shear modulus and strength after 2,016 hours of aging, respectively. Haque et al. [9] implemented a 2D viscoelastic cohesive layer model to simulate the changes in the flexural properties in a three-point bend test. Unidirectional IM7/BMI laminates were aged at 260 °C for 3,000 hours in air. It was observed that weight loss rate, flexural modulus and strength were significantly reduced in the laminates having fibers in the transverse direction. Meng et al. [10] developed a 3D finite element model of a three-point bend test for unidirectional, cross-ply and angle-ply carbon/epoxy laminates. The work focused on the free-edge stresses effect on the bending stiffness reduction using 3D classical lamination theory and Tsai-Hill criterion for failure initiation. The modeling results revealed significant transverse normal stresses and in-plane shear stress in the cross-ply and angle-ply laminates, respectively.

The current work presents a comprehensive investigation of the degradation mechanism effects in terms of elastic and strength properties under respective aging times. Weight loss simulation results for each time interval were considered in a three-point bending model to analyze the degradation in flexural behavior. A damage parameter was developed from the average thickness of oxidized layer and crack length. The damage parameter was assumed linearly-dependent on the reductions based on irreversible thermodynamics principles. A cross-ply BMI laminate was manufactured using out-of-autoclave (OOA) process. The laminate was sectioned in to weight loss and three-point bend samples to investigate thermal aging effects under diffusion-controlled conditions. Scanning electron microscopy images were acquired for aged laminates to discern the damage induced by thermal aging. Differential scanning calorimetry test was conducted to measure the glass transition temperature of aged and virgin samples.

2. MICRO/MACRO-SCALE MODELING OF THERMO-OXIDATION

Modeling of the transient thermo-oxidation aging was implemented in the homogenized RVE level to determine the oxidized layer and weight loss. Then, weight loss results were scaled by the respective area ratios to the macroscale level as detailed below. A multi-fiber multi-layer RVE was utilized for the micro-scale simulations of the cross-ply laminate. The RVE geometry has the fiber volume fraction of 57.66 %, as shown in Figure 1. The x-coordinate orientation of the RVE represented transverse-direction (through-thickness-direction). By introducing the homogenized properties of the RVE,

Fick's second law of diffusion with a reaction term, $R_{eff}(C, \phi^{eff})$, and a time-dependent

oxidation state variable, $\phi^{eff}(t)$, can be represented as the following equations:

$$\frac{\partial C(x,y,z,t)}{\partial t} = \vec{\nabla} \cdot (D_{eff}(\phi^{eff})\vec{\nabla}C(x,y,z,t)) - R_{eff}(C, \phi^{eff}) \tag{1}$$

$$\frac{d\varphi^{eff}}{dt} = -\alpha(t,T)R_{eff}(C, \varphi^{eff}) \tag{2}$$

where C is the oxygen concentration; D_{eff} is the effective diffusivity; and $\alpha(t,T)$ is a fitted

proportionality parameter depending on time and temperature. The proportionality

parameter was determined by fitting the simulation results to the experimental weight loss

results throughout the oxidation time.

Assuming that the fiber is unoxidized during thermo-oxidation, homogenization of

the diffusivity and reaction term in Equations (1-2) can be obtained using the rule of

mixtures [3]:

$$D_{eff}(\varphi^{eff}, T) = D_{eff}^{un}(T)\{\frac{\varphi^{eff} - \varphi_{ox}^{eff}}{1 - \varphi_{ox}^{eff}}\} + D^{ox}(T)\{\frac{1 - \varphi^{eff}}{1 - \varphi_{ox}^{eff}}\} \tag{3}$$

$$R_{eff}(C, \phi^{eff}, T) = R_0^{eff}(T)\{\frac{\phi - \phi_{ox}^{eff}}{1 - \phi_{ox}^{eff}}\}[\frac{2\beta C}{1 + \beta C}(1 - \frac{\beta C}{2(1 + \beta C)})] \tag{4}$$

$$R_0^{eff}(T) = V_m R_0^m(T) \tag{5}$$

$$\varphi_{ox}^{eff} = \varphi_{ox}^m(1 - V_f) + V_f \varphi_{ox}^f \tag{6}$$

where D_{eff}^{un} and D^{ox} are the unoxidized composite effective diffusivity and oxidized

matrix diffusivity represented in Arrhenius forms, respectively.

The RVE orthotropic effective diffusivity can be estimated using the averaging

method. The steady-state concentration field, $C(x, y, z)$, and the diffusivity tensor of the

matrix and fiber, $D(x, y, z)$, were used to estimate the effective diffusivity by volume averaging method [1]:

$$D_{eff}(i) = \int_0^a \int_0^b \int_0^c D_{iq}(x_1, x_2, x_3) \frac{\partial C(x_1, x_2, x_3)}{\partial x_i} dx_1 dx_2 dx_3 \qquad i, q = 1,2,3 \qquad (7)$$

where D_{eff} is the homogenized diffusivity; D_{iq} is the diffusivity tensor of fiber and matrix; a, b and c are the geometry limits of the scaled RVE element; and x_1, x_2, x_3 are x, y, z.

The RVE consisted of two cubes with three fibers each that distributed randomly in the matrix. Fibers were randomized in the RVE geometry using a Matlab code assuming that fiber diameter is 5 µm. Thermo-oxidation was considered as a localized phenomenon where the interaction between longitudinal- and transverse-oxidation was neglected. Accordingly, weight loss simulations were run in the longitudinal- and transverse-direction separately. However, the RVE thickness of x-direction was not the actual laminates' thickness, the area ratio of total weight loss accounted for the thickness scaling. This yielded that the three-fiber cube represents one layer thickness. The size of the RVE was also representative regarding diffusivity homogenization, where the diffusivity is not dependent on the RVE volume if the topology is kept the same. This means if each cube was duplicated to represent a full layer thickness, then the RVE x-dimension will be equal to two-layer thickness (real thickness) and the diffusivity will be the same. Thus, since the fiber volume fraction of the RVE was equivalent to the targeted laminate, the homogenized diffusivities were also equivalent.

Henry's Law for sorption was used to calculate oxygen concentration at the boundaries:

$$C|_b = S \times P \tag{8}$$

Solubility, S, is a temperature-independent parameter, $S = 3.61 \times 10^{-4}$ mol/m^3·Pa for BMI. Oxygen partial pressure, P, was calculated as 0.21 of the air pressure at the aging temperature.

The following integral was introduced for weight loss due to oxidation:

$$W_{loss}(t) = \rho_0 \iiint\limits_{matrix} (1 - \varphi)dv \tag{9}$$

where ρ_0 is the density of the unoxidized polymer matrix calculated from the unoxidized composite density (ρ_c). A scaling procedure was introduced by the respective surface area ratio of the sample to RVE. In all cases, the sample's surface area was calculated from initial measurements in the longitudinal- and transverse-simulations:

$$W_{loss} = W^r_{loss}(x) \times \frac{A^s_x}{A^r_x} + W^r_{loss}(y) \times \frac{A^s_y}{A^r_y} + W^r_{loss}(z) \times \frac{A^s_z}{A^r_z} \tag{10}$$

where W_{loss} is the total weight loss in the sample's scale; $W^r_{loss}(x)$, $W^r_{loss}(y)$ and $W^r_{loss}(z)$ are the weight loss per RVE due to oxidation in x, y, and z calculated using the volume integral of Eq. 9; and A^s_x and A^r_x are the areas of oxidation-exposed surface perpendicular to x-direction in the sample and the RVE, respectively. Similarly, A^s_y, A^s_z and A^r_y, A^r_z are the exposed surface areas in their respective scales and directions. A similar definition was introduced for A^s_y / A^r_y and A^s_z / A^r_z in their respective directions. All simulations in this section were implemented in COMSOL Multiphysics using the properties listed in Table 1.

3. MESO/MACRO-SCALE THREE-POINT BENDING SIMULATION

This part utilized the weight loss and thermo-oxidation results of the previous part using the scaling procedure and RVE weight loss results. Oxidative-induced shrinkage and residual stresses were not considered in this modeling as the aged samples were already damaged and the flexural behavior of the damaged/cracked laminates was the major point of this work. The mechanical behavior of virgin and aged cross-plied laminates under flexural loading was investigated using a 16-layer sample geometry, as shown in Figure 2.

A homogenized material having orthotropic mechanical properties in the meso-scale represented each layer (lamina). The top and bottom layers had the longitudinal direction oriented in y-axis. For intact laminates, the elastic and strength mechanical properties were taken from the manufacturer's datasheet. Due to the lack of experimental data and to account for thermal aging effects, the elastic and strength properties of each layer were reduced numerically by specific fractions. It was assumed that the thermal aging degradation in any layer was homogenous and results in an overall reduction of the sample properties, which is the basis of the CDM approach. CDM approach assumes homogenization for damage throughout the whole layers where a single layer damage is not considered separately. The reductions were assumed to be linearly-dependent on the instantaneous damage parameter of the degraded lamina. The linear dependence was based on the CDM mathematical formulations derived from the irreversible thermodynamics principles for isothermal aging [6, 7]:

$$E_1(t) = E_1^{\,o} + 2\beta(t) \times [A_1 - A_2 \nu_{12}^{\,o} + A_3 (\nu_{12}^{\,o})^2] \tag{11}$$

$$E_2(t) = E_2^0 + 2\beta(t) \times [A_3 - A_2 v_{21}^0 + A_1 (v_{21}^0)^2] \tag{12}$$

$$v_{12}(t) = v_{12}^0 + 2\beta(t) \times \frac{1 - v_{12}^0 v_{21}^0}{E_2^0} \left[\frac{1}{2} A_2 - A_3 v_{12}^0 \right] \tag{13}$$

$$G_{12}(t) = G_{12}^0 + 2\beta(t) \frac{A_4}{4} \tag{14}$$

where $E_1(t)$, $E_2(t)$, $v_{12}(t)$ and $G_{12}(t)$ are the reduced in-plane elastic properties of the aged lamina as a function of the aging time; E_1^0, E_2^0, v_{12}^0, v_{21}^0 and G_{12}^0 are the intact in-plane elastic properties of the lamina; $\beta(t)$ is the damage parameter due to thermo-oxidation cracking and debonding; and A_1, A_2, A_3 and A_4 are constants. By determining the constants' values, Equations (11-14) correlates the degraded elastic properties linearly to the damage parameter. For the present work, the damage parameter due to interfacial sliding was selected [24]:

$$\beta(t) = \frac{\pi^2 d^4 \eta^2}{64 V_f^2} C_d \tag{15}$$

where d is the fiber diameter; η is the crack number density (number of cracks per unit volume); C_d is the crack opening displacement averaged over the RVE volume. Assuming that the crack opening displacement is proportional to the crack length, l:

$$\beta(t) = \xi \eta^2 \langle d^4 l^2 \rangle \tag{16}$$

where ξ is a constant dependent on the fiber volume fraction and fiber stiffness; $\langle d^4 l^2 \rangle$ is the RVE volume averaged fiber diameter and crack length. The crack length can be defined as:

$$l = kd \frac{1 - \sqrt{V_f}}{\sqrt{V_f}} \tag{17}$$

where k is a constant. Thermo-oxidation is a transient phenomenon where the oxidized layer and cracking/debonding advance gradually throughout the aging time. The application of the damage terms in Equations (15-17) requires the introduction of a time-dependent crack length and constants. Cracks/debonds are shrinkage induced due to the evolution of the oxidized layer. The crack length was assumed dependent on the thickness of the oxidized layer, $\theta(t)$. To satisfy the requirements of Equation 16, crack length and thickness of oxidized layer were averaged over the RVE volume. The relationship between the average oxidized layer and crack length was assumed a second order polynomial of the form:

$$l(t) = A\theta(t)^2 + B\theta(t) + C \tag{18}$$

where A, B and C are constants. The experimental findings of aging G30/PMR-15 unidirectional composite at 288 °C [12] indicated that the average crack length and oxidized layer varied nonlinearly with time. The variation of the average crack length and oxidized layer thickness is shown in Figure 3. Combining Equations (15-18) yields:

$$\beta(t) = C_2(A\theta(t)^2 + B\theta(t) + C)^2 \tag{19}$$

where $C_2 = \eta^2 \xi d^4$. Determination of the polynomial and damage constants in Equation 19 for the current work will be discussed in the results part. It should be noted that the damage parameter $\beta(t)$ and the oxidized layer thickness $\theta(t)$ are also varying with location inside the matrix. The variation of the oxidation state variable $\phi^{eff}(t)$ with location is what produces the spatial distribution of the damage parameter.

For the current simulations, Poisson's ratio was assumed constant so that the reduction of Equation (13) was negligible. By introducing a reduction variable, R, that

equals the property change divided by the intact property and accounting for a constant Poisson's ratio:

$$R_{E1}(t) = \frac{2\beta(t)}{E_1^{\ 0}}\left[A_1 - \frac{1}{2}A_2\nu_{12}^{\ 0} \right] \tag{20}$$

$$R_{E2}(t) = \frac{2\beta(t)}{E_2^{\ 0}}\left[A_1(\nu_{21}^{\ 0})^2 + A_2\left(\frac{1}{2\nu_{12}^{\ 0}} - \nu_{21}^{\ 0}\right) \right] \tag{21}$$

$$R_{G12}(t) = \frac{2\beta(t)}{G_{12}^{\ 0}}\left[\frac{1}{4}A_4 \right] \tag{22}$$

where $R_{E1}(t)$, $R_{E2}(t)$, and $R_{G12}(t)$ are the instantaneous reductions of the longitudinal, transverse, and in-plane shear moduli, respectively. Three unknown constants A_1, A_2 and A_4 are required to determine the reductions in the in-plane elastic properties of a lamina undergoing isothermal aging.

After accounting for the elastic and strength properties' reductions, three-point bending simulations were implemented in Abaqus. Damage initiation due to bending load was modeled using Hashin's Criterion. By default, a linear softening for damage evolution was imposed. Damage evolution fracture energy constants for BMI were taken from the literature. The elastic, strength and fracture energy properties are listed in Table 2.

All three-point bending simulations were conducted using constant longitudinal and transverse fracture energies for aged and virgin laminates. Moduli and strengths of all plies were reduced accounting for the reduction in the whole sample flexural properties as it was measured experimentally. The mathematical formulations of the critical energy release rate of thermally-cracked cross-ply laminates [16] were used to test the effects of the elastic properties' reductions on the fracture energy. The application of equal reductions

to elastic and strength properties, to mimic the thermal aging effects, yielded a constant critical energy release rate that supported the current work assumption for fracture energy. Continuum shell elements were used to mesh the laminate, supports, and load cell. Rigid body constraints were imposed on the steel support and load cell pins to suppress their deformations and to allow a translational motion only. All contacts were assumed frictionless in the tangential behavior and hard in the normal behavior. The boundary conditions of the support pins were zero displacements and rotations, imposed on the reference point in all directions. A plane extending in x-axis through the middle of the sample's width was created and assigned a zero y-displacement boundary condition. The mid-span plane perpendicular to x-axis was constrained in its bottom line by assigning a zero x-displacement boundary condition. A predefined z-displacement boundary condition of 7 mm was imposed on the reference point of the load cell, allowing computation of the reaction force during the simulation. All cases were solved using the implicit solver with a minimum and maximum time increments of 1×10^{-12} and 0.1 s.

4. MATERIALS AND EXPERIMENTAL PROCEDURE

Composite laminates in the orientation $[0°/90°]_{8s}$ were manufactured using IM7G/AR4550 BMI unidirectional prepreg system from Aldila Composite Materials, suitable for OOA curing. Two half panels, of layup $[0°/90°]_{4s}$, were debulked separately for 60 minutes at a vacuum pressure of 28 in. Hg to ensure good prepreg compaction. The half panels were then combined to form the full panel with prepreg layup $[0°/90°]_{8s}$, sealed and placed in an oven. The layup was debulked for 120 minutes at a temperature of 50 °C

and a vacuum pressure of 28 in. Hg. The manufacturer recommended cure cycle was used. A set of three samples measuring 76.2 mm x 76.2 mm was cut using a low speed saw for weight loss measurements. Another set of 40 coupons measuring 100 mm x 12.7 mm x 2.8 mm was cut and used for three-point bending test. Three replicates per time interval were used for the bending test. Two coupons measuring 152.4 mm x 25.4 mm were used to cut the scanning electron microscopy (SEM) samples up on removal of the coupons from the oven. Samples were cleaned, and dried in an oven at 70 °C for 20 hours. Initial weights and dimensions were measured, and samples were placed in a convection oven for aging at 176.67 °C. Test samples were removed at regular intervals of 100 hours to measure the weight loss and cut the SEM samples. Samples were allowed to cool down for 15 min. inside the oven and then moved to a desiccator to cool down to room temperature under vacuum. Sample mass was measured using a high precision balance with a least count of 0.1 mg. SEM samples were embedded in epoxy and polished progressively. The SEM images were acquired by a dual-beam Helios 600 electron microscope using an accelerating voltage of 5 kV and a beam current of 43 pA. The working distance was in the range of 3.4 to 4.4 mm. Three-point bending test was conducted according to ASTM D790 [11]. The support span was set to 64 mm that corresponded to a span to depth ratio of about 27. The flexural modulus, E_B, was calculated using:

$$E_B = \frac{PL^3}{4Wbd^3} \tag{23}$$

where P is the maximum applied load; L is the span; W is the corresponding deflection at the center of the beam; b is the sample's width; and d is the sample's depth.

Extent of cross-linking in a polymer can be known from the glass transition temperature (T_g) [19, 21]. A DSC test was performed using Q2000 machine (TA

Instruments, New Castle, DE). Around 15 mg of sample was powdered and encapsulated in aluminum pan. The pan was subjected to increasing temperature to 400 °C at 20 °C/min, followed by cooling to 0 °C and again increasing the temperature to 400 °C. The glass transition temperature was recorded and has been discussed further in the results section.

5. RESULTS AND DISCUSSION

5.1 AGING EXPERIMENTS AND SIMULATION RESULTS

In Figures 4 and 5, the results of aging experiment and simulation are plotted over the aging time up to 1,700 hours at 176.67 °C. Figure 5 was graphically determined from Figure 4 by calculating the ratio of weight loss difference to the time change. The weight loss behavior was nonlinear with a changing rate up to the aging hours of the current work. The total weight loss during aging under oxidative environments like air is the sum of the pyrolysis and oxidative weight loss. Pyrolysis weight loss is due to polymer decomposition that takes place throughout the polymer volume. The oxidative weight loss is due to a superficial thermo-oxidation of the polymer matrix arising from oxygen diffusion-reaction. In the author's previous work on unidirectional composites [17], it was concluded that the weight loss under argon is about 8 % of the total weight loss measured for samples aged under air. However, the same ratio was considered for the pyrolysis weight loss of the current work, as the samples' volume was similar in both cases. The weight loss experimental results were the average of three replicates over the aging hours. After 1,670 hours, samples lost 0.5 % of its average original weight of 19.37g. Two distinct regions are shown in the weight loss rate behavior. The weight loss rate behavior shows a higher initial

rate up to 200 hours. The higher initial weight loss rate was reported in the literature for unidirectional and cross-ply modified-epoxy laminates [18] and for cross-ply epoxy laminates [19]. Another interesting observation in the rate behavior is that the average weight loss rate in the 900-1,700 hours region was 2.5 times the average in the 200-900 hours region. A change in the oxidation mechanism or oxidation exposed area is highly possible due to a progressive matrix shrinkage and/or debonding.

The degree of cure or cross-linking is highly correlated to the T_g, an increase in the cross-linking is accompanied by a T_g increase [22]. Incomplete BMI curing/crosslinking was reported in the literature and it was emphasized as a significant degradation mechanism responsible for properties reduction [20]. Similar effects of the cross-linking for polyimide matrix composites was also elaborated [21]. The DSC measurements of T_g vs. aging temperature is shown in Figure 6. T_g was increased by 10 °C when the aging time reached 500 hours where the cross-linking was expected to complete throughout the cross-linking dominated region (t<500 hours). The degradation in T_g in the oxidation-dominated region (t>500 hours) was attributed to the oxidation effects on the cross links. The detrimental effects of oxidation on the cross-linking density and mechanical properties for unidirectional IM-7/PETI-5 composites were reported in [8]. The effects of cross-linking were assumed similar for the BMI composites of the current work.

To simulate weight loss in the sample level, the weight loss in the RVE level should be scaled by the respective area ratios. The cross-ply RVE level simulation was conducted by considering the following form of oxidation proportionality parameter:

$$\alpha(t) = \left\{ \begin{array}{ll} 25 \times 10^{-5}, & t \leq 200 hr. \\ 1.8 \times 10^{-5} e^{(6.75 \times 10^{-7} \times t)}, & t > 200 hr. \end{array} \right\} \tag{24}$$

It is noteworthy that similar form of the oxidation proportionality for the second region (t >200 hr.) was used to simulate the aging behavior of unidirectional laminates at 200 °C in the author's previous paper [17]. The simulation results are in a good agreement with the experimental findings as shown in the previous two figures. The spatial distribution of oxidation in the RVE simulations after 1,500 hours are shown in Figures 7 and 8. For the longitudinal oxidation, only z-oxidation is depicted because the oxidation evolution was similar in the longitudinal z- and y-directions (perpendicular to sample edges). The oxidation state of 0.66 and 1 represent a completely oxidized and unoxidized matrix, respectively.

5.2 SCANNING ELECTRON MICROSCOPY ANALYSIS

The SEM samples were cut such that the area of interest was parallel to the side faces, as shown in Figure 9. The SEM images that acquired at 400 hours of aging did not show any micro-cracks/debonds or a significant matrix shrinkage as shown in Figure 10(a). Also shown is a resin-rich region at the interface between the surface layer of 90° and the second layer of 0° that was a manufacturing-related issue. The presence of damaged fiber ends was due to the cutting/polishing sequence that removed/cracked parts of the fiber ends. In Figure 10(b), the onset of micro-cracks/debonds was at around 500 hours that provided a strong evidence of the onset of aging damage due to thermo-oxidation. However, matrix shrinkage was not evident until the aging time of about 1000 hours. The shrinkage was localized at the resin-rich regions of the outer 90°-layer as shown in Figures 10(c) and 10(d). The micro-cracks/debonds were initiated at the interfaces of the internal fibers away from the oxidation-exposed surface. These "blunt" micro-cracks/debonds then

propagated to the superficial layer. This scenario of micro-cracks/debonds initiation/propagation was elucidated from the current SEM images that supported better understanding of the mechanism. This explained the rapid fluctuated increase in the weight loss rate beyond 1000 hours of aging, shown previously in the weight loss rate vs. aging time plot. As matrix shrinks, debonds initiate and interconnect due to excessive shrinkage forming a "blunt" micro-crack. Then, the "blunt" micro-crack opens to the outside oxidative air, leaving the crack surfaces connected to the sample's outer surfaces. Figure 10(d) shows the matrix shrinkage that preceded debonds initiation and micro-crack formation/opening. The internal layers did not show any discernible transverse debonds and/or micro-cracks where transverse oxidation was limited to the superficial layers only. The longitudinal oxidation cracking (at the end faces) was not characterized as its effect was considered insignificant where the bending load was applied transversely.

5.3 THREE-POINT BENDING EXPERIMENTS AND SIMULATION

This part dealt with the flexural behavior of the aged composite where oxidation simulation results were transferred from the previous part by considering oxidation effects on the mechanical properties globally. The reductions of Equations (20-22) were assumed linearly dependent on the thickness of oxidized layer by setting a damage parameter to unity. The evolution of the average oxidized layer was determined from the thermo-oxidation simulations. By assigning similar linearly-dependent reductions determined by try and error to all elastic properties, multiple three-point bending simulations were conducted for each aging hour to match the experimental findings. Initially, strength properties reduction was assumed equal to the elastic reduction for the whole aging hours.

Based on this assumption, the modulus simulation results did not agree for the region of aging (t<500 hours). When the strength properties reductions were assumed smaller than the elastic reductions for that region, the flexural modulus simulations matched to the experimental findings. Similar findings were reported in [21] for polyimide matrix composites that the room temperature longitudinal flexural and short beam shear strengths were constants during the early hundreds of aging hours. Also reported, that oxidation reduces the room temperature strengths and stiffness at early hundreds of aging hours.

Figure 11 shows three aged test coupons that failed due to bending stresses at the top and bottom plies. All coupons showed a failure at the middle span of facial plies with a significant evidence of bending failure as implied in the standard.

Figure 12 shows the damage variable of the matrix due to compression, DAMAGEMC, of a sample aged for 1,670 hours. A value of less than unity represents a failure/damage initiation in the matrix that attains a complete damage at a value of unity. The failure simulation analysis of the cross-ply laminates showed that the final failure (maximum load point) occurs when the matrix fails due to compression under the load cell. However, the other mechanisms of failure: matrix tension/shear and fiber tension/compression started earlier. The matrix failure due to the compression was critical especially for thermally aged laminates where matrix oxidation was expected. However, aged and virgin laminates showed similar damage behavior in simulation that matched with the experimental findings.

Figure 13 shows the experimental and simulation flexural modulus of the aged and virgin cross- ply laminates. The experimental results showed inconsistency in the modulus as aging time increased. The modulus decreased by 19 % as aging time approached 1,700

hours. For the first 200 hours, a sharp rate of modulus decrease was evident stemming from the cross-linking effect. Cross-linking progression degrades the mechanical properties of BMI composites during service at high temperatures because the unreacted sites are considered as defects [20]. This reflects a direct correlation between the weight loss/weight loss rate and flexural modulus decrease. The reduction in the flexural modulus over the first 500 hours was around 14 % that mainly attributed to the cross-linking mechanism where mechanically insignificant oxidation effect was expected in this region. Once the cross-linking was complete, the role of oxidation in the modulus degradation was significant by debonding/micro-cracking damage.

The simulation results were based on numerical reductions in the strength and elastic properties. For the aging time of 400 hours, the reduction was 13.5 % and 3 % in the elastic and strength properties, respectively. When aging time reached 1,670 hours, an equal reduction of 15.5 % was applied to the elastic and strength properties. The simulation results are acceptable compared to the fluctuations in the experimental findings. At early aging times and up to 400 hours, it was proposed that these reductions are not equal for the elastic and strength properties as discussed earlier. The reduction of the strengths at 400 hours was 77 % less than the reduction in the elastic properties to best fit the experimental modulus. In the literature, the degradation reduction was theoretically considered only in the elastic properties [6].

Figure 14 shows the experimental and simulation load-displacement curves of intact and 1,670-hour aged laminates. The simulation curves are in a good agreement with the experimental curves; however, the intact samples simulation behavior shows a discrepancy from the experimental behavior for the damage evolution interval that was out

of the scope of the current work. The load and displacement at the peak point are closely matched that was the basis for better flexural modulus predictions compared to the experimental findings.

5.4 DETERMINATION OF THE DAMAGE CONSTANTS

The average thickness of oxidized layer was determined from thermo-oxidation simulations and plotted in Figure 15. To determine the second order polynomial constants A, B and C, a Matlab code was used. Since the constants A_1, A_2 and A_4 were not changing from time to time and the reductions of Equations (20-22) were known, the unknowns A, B and C were then determined by solving the simultaneous equations. The polynomial equation was then determined:

$$l(t) = 2 \times 10^4 \, \theta(t)^2 - 0.58259 \theta(t) + 6.8773 \times 10^{-5} \qquad (25)$$

Once the above equation was determined, then similar procedure was used to determine the A_1, A_2 and A_4 constants. These constants are listed in Table 3. It should be noted that the reduction equations were based on a CDM approach that is only valid for a micro/macro-level damage. The damage in the early aging time up to 500 hours was a molecular damage, which is beyond the scope of the CDM approach.

6. CONCLUSIONS

The flexural behavior of aged cross-ply bismaleimide composites was investigated experimentally and numerically. An analysis of the degradation mechanisms: cross-linking

and oxidation in a multiscale approach was presented to gain a better understanding of the flexural behavior under aging. The cross-linking mechanism degraded the composite flexural behavior in the range (t<500 hours) that BMI composites showed a strong tendency to cross-link during aging. The simulation results showed that the cross-linking progression mainly affected the elastic properties at the mesoscale while, insignificantly affected the strength properties at the same level. Locally, oxidized layers have higher modulus, as shown by previous works, where this was limited to the surficial layers and it would not affect the stiffness overall. However, similar quantitative effect of oxidative damage on strength and elastic properties produced a better estimation of the flexural modulus in the macro-scale. The embrittlement of the oxidized layer and its effect on the cracking damage where strength and fracture energies are locally degraded was not considered in this work and will be investigated in a future work.

The multiscale approach of the current work investigated thermo-oxidative weight loss at the RVE microscale and scaled it to the sample macroscale using respective area ratios. Three-point bending test was simulated at the macroscale by reducing the elastic and strength properties in the lamina mesoscale. The oxidative damage was related to the lamina weight loss ratio in the mesoscale by introducing a time-dependent proportionality variable that was the basis for a novel damage parameter. The time-dependent proportionality variable was proposed to account for the numerical variations in the damage parameter. Simulated numerically and verified experimentally, the failure of the matrix due to compression was the critical mechanism of failure among the fiber tension/compression and matrix tension/shear. Experiments were conducted to collect the weight loss data at 176.67 °C for around 1,700 hours. Simultaneously, three-point bending

test coupons were also aged and tested to inspect the changes in the flexural properties. The micro-cracking/ debonding damage was monitored using SEM of aged coupons. After being aged for 1,700 hours, samples showed 0.5 % loss of the original weight and 19 % reduction in the flexural modulus. The cross-linking completion was at around 500 hours where the T_g plot showed the lowest rate of change with aging time. The formation of "blunt" micro-cracks around 500 hours revealed that the oxidative shrinkage reached a critical value. These "blunt" cracks extended and opened to connect with the external sample surfaces at around 1000 hours. Owing to the detrimental effect of oxidation on the cross-linking, the T_g plot showed a remarkable inclination up to 1500 hours (a drop of 44 °C vs. 1000 hours of aging in the oxidation-dominated region).
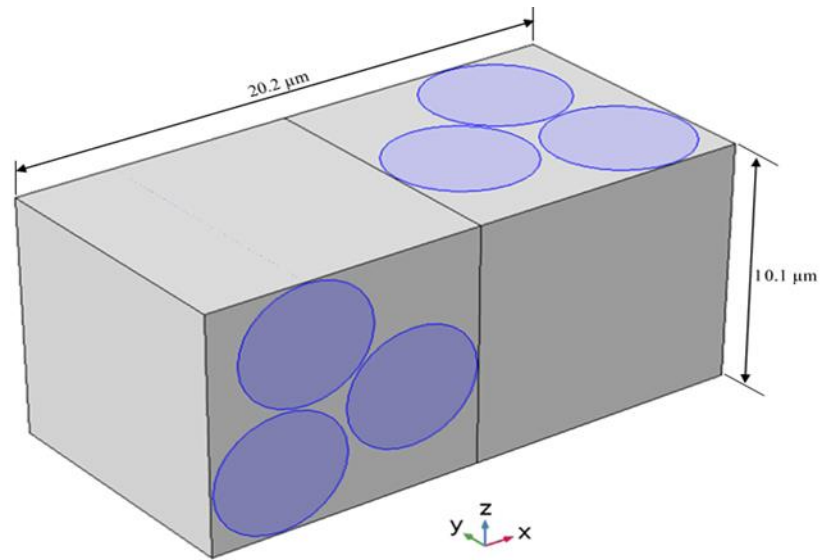
Figure 1. RVE geometry (highlighted fibers)
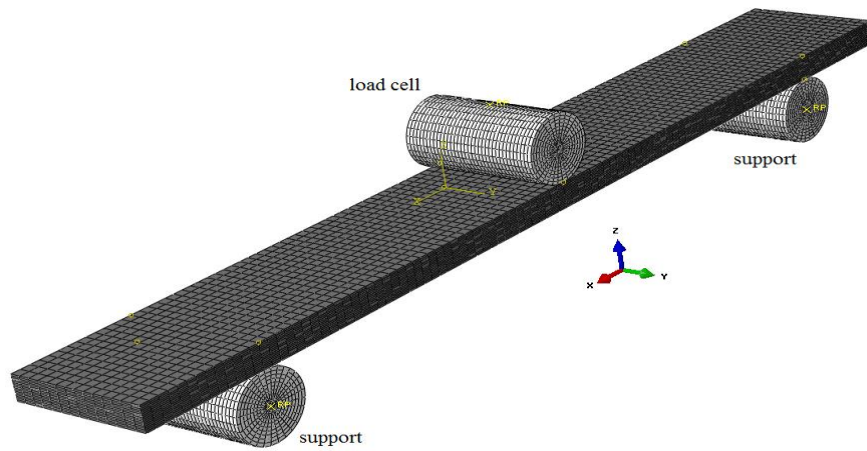
Figure 2. Three-point bending simulation assembly
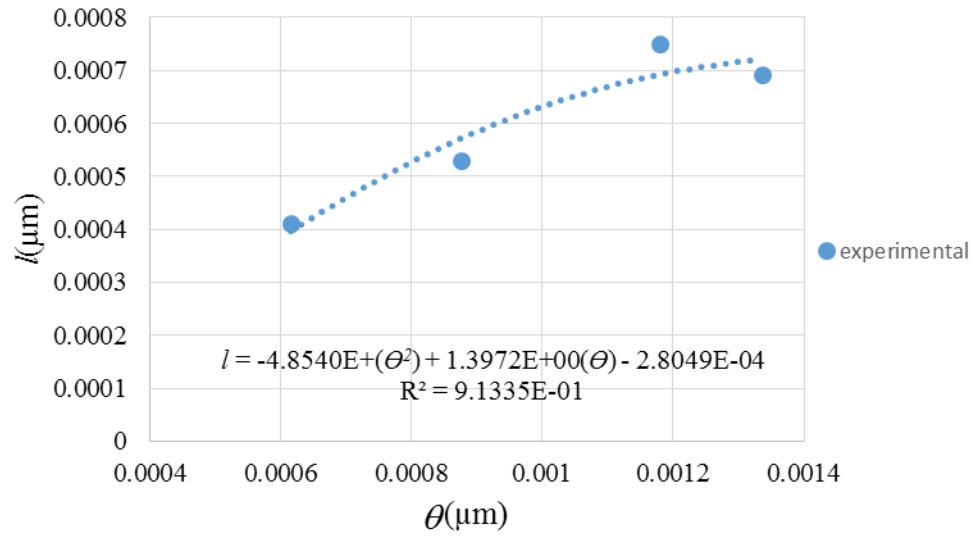
Figure 3. Average crack length vs. average oxidized layer thickness [12]
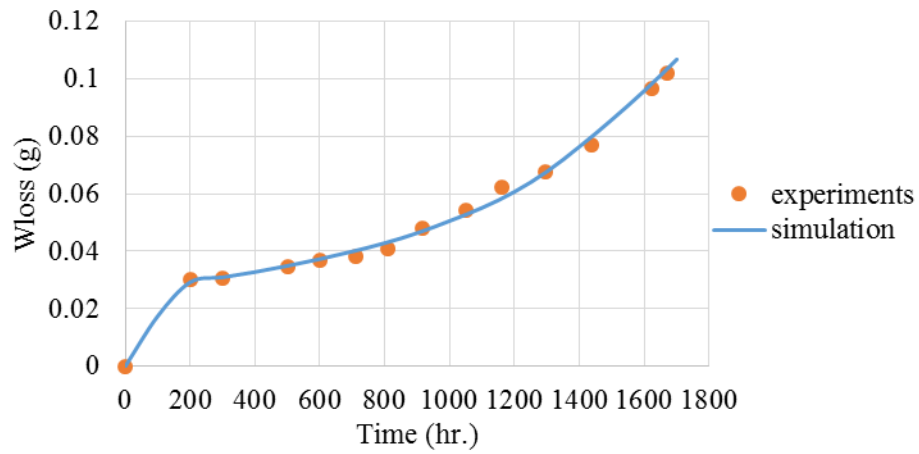
Figure 4. Weight loss vs. aging time of the cross-ply laminates
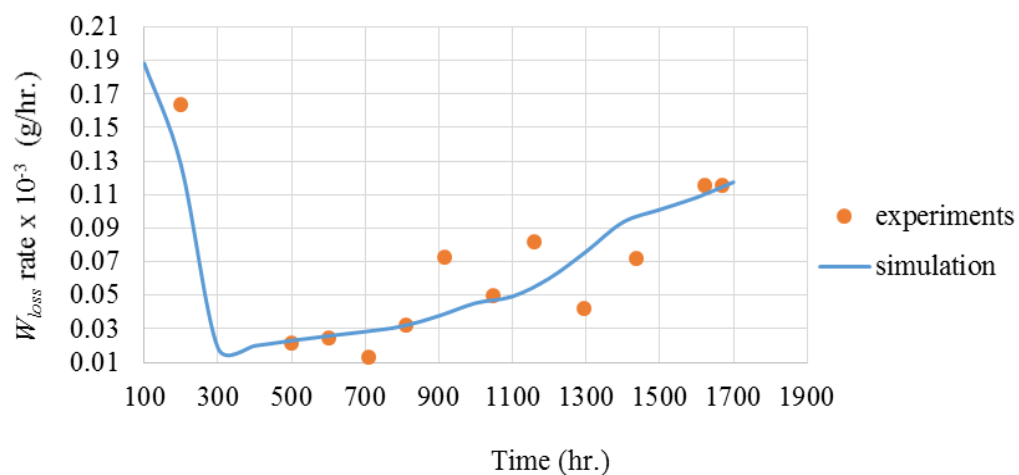
Figure 5. Weight loss rate vs. aging time of the cross-ply laminates
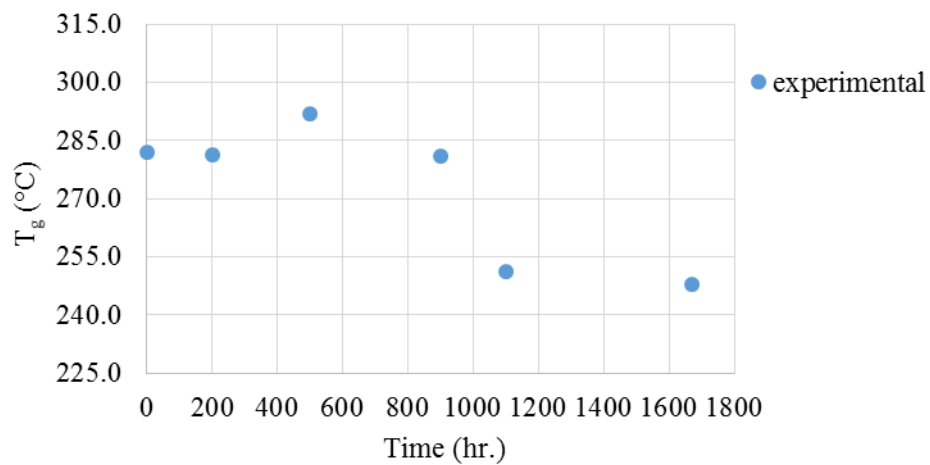
Figure 6. T_g vs. aging time of the cross-ply laminates
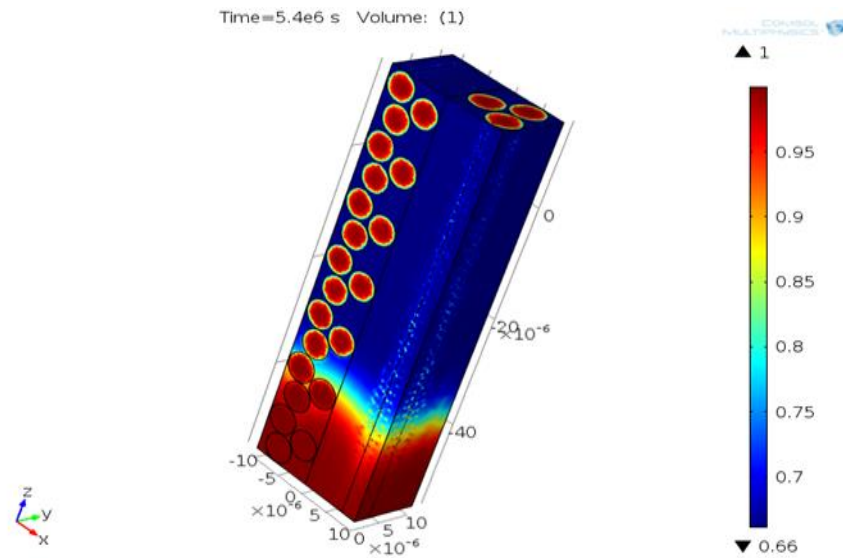
Figure 7. The oxidation state distribution after 1,500 hours in the longitudinal case
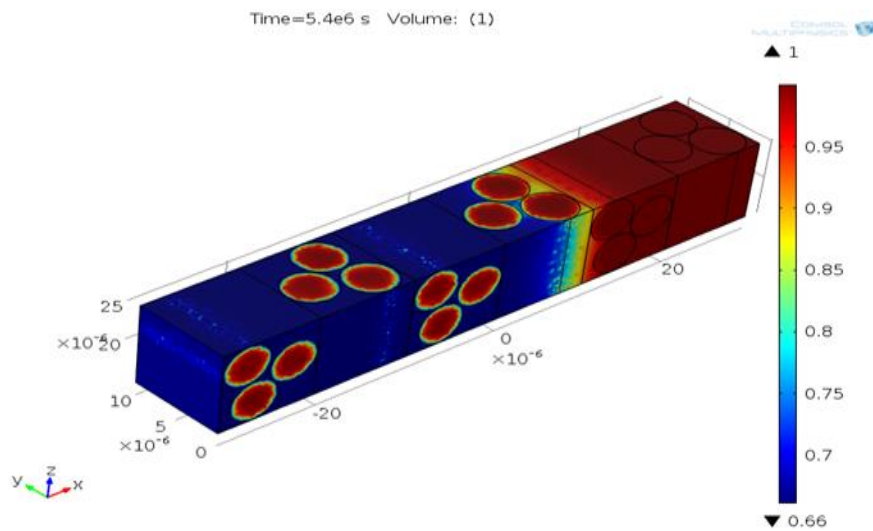
Figure 8. The oxidation state after 1,500 hours in the transverse case
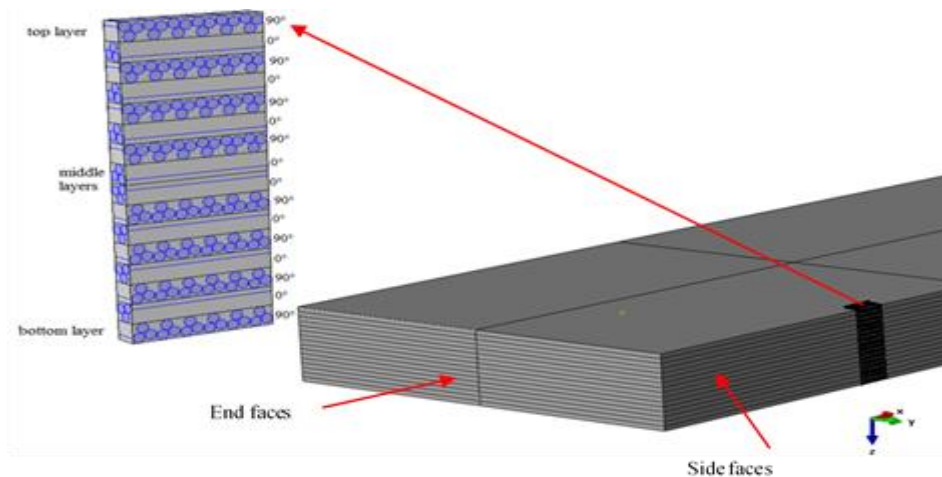
Figure 9. The SEM sampling for micro-cracks/debonds imaging
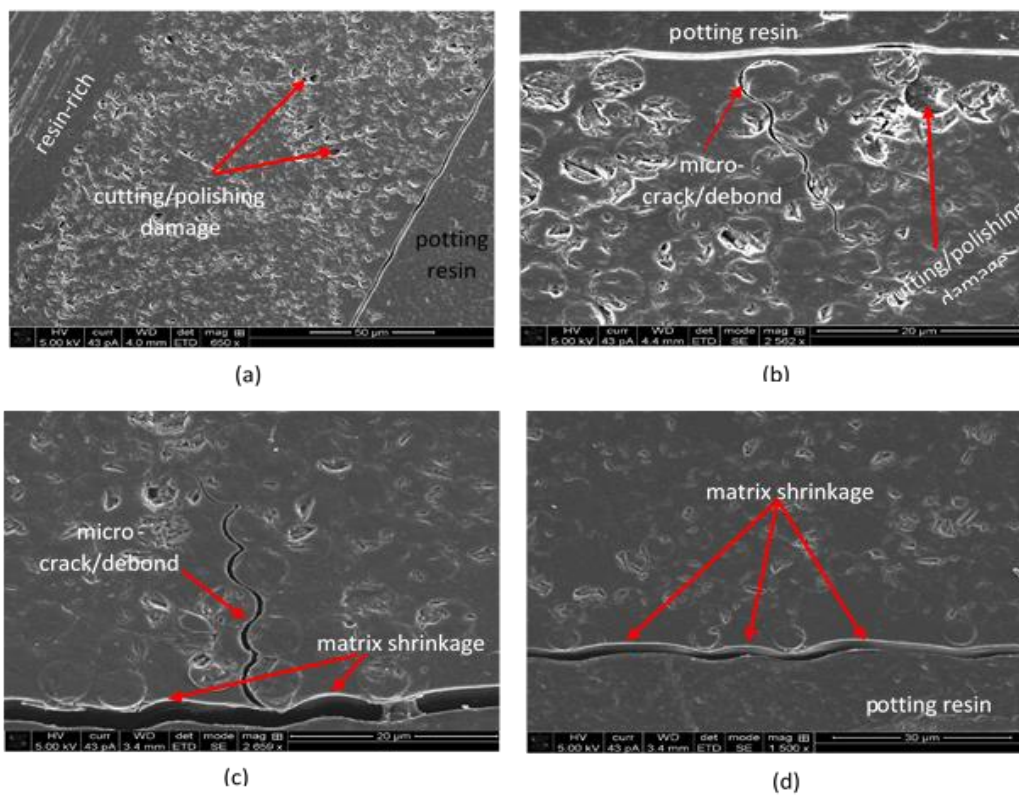
Figure 10. SEM images of aged samples
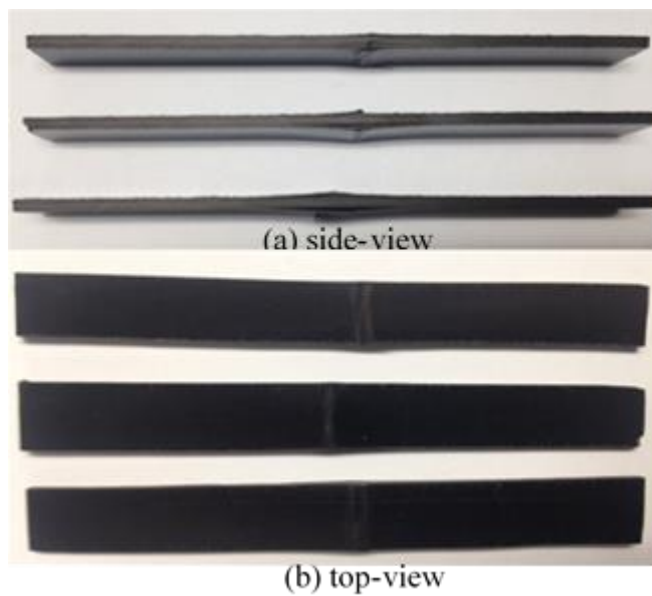
Figure 11. Samples failed by bending (aged for 1,100 hours)
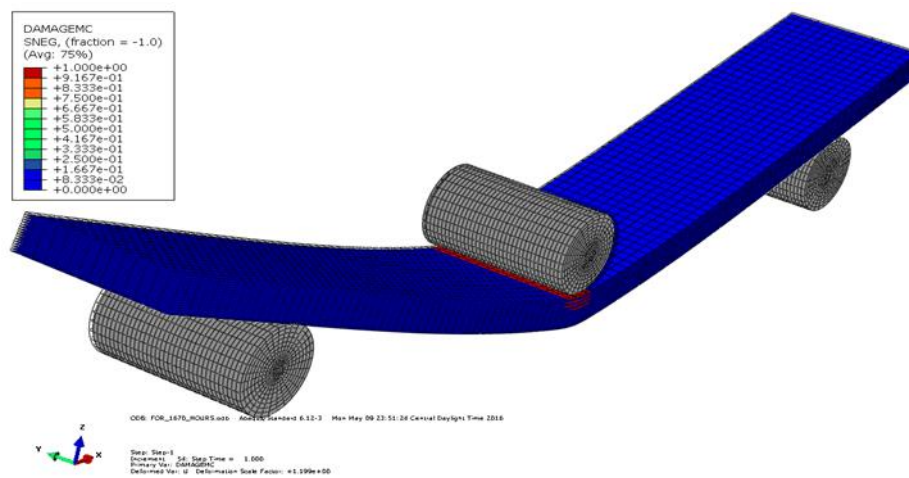
Figure 12. Matrix compression damage of a 1670-hour aged sample
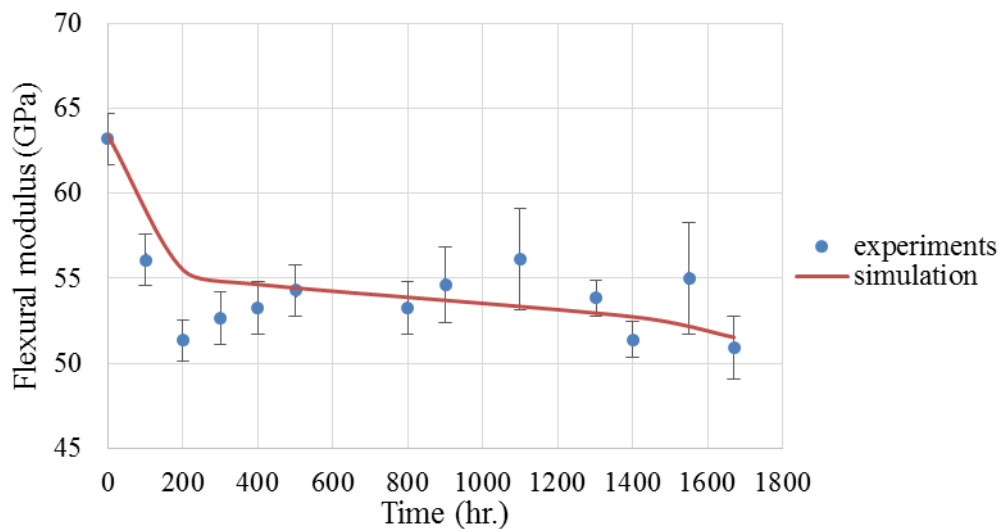
Figure 13. Flexural modulus of the cross-ply laminates vs. aging time
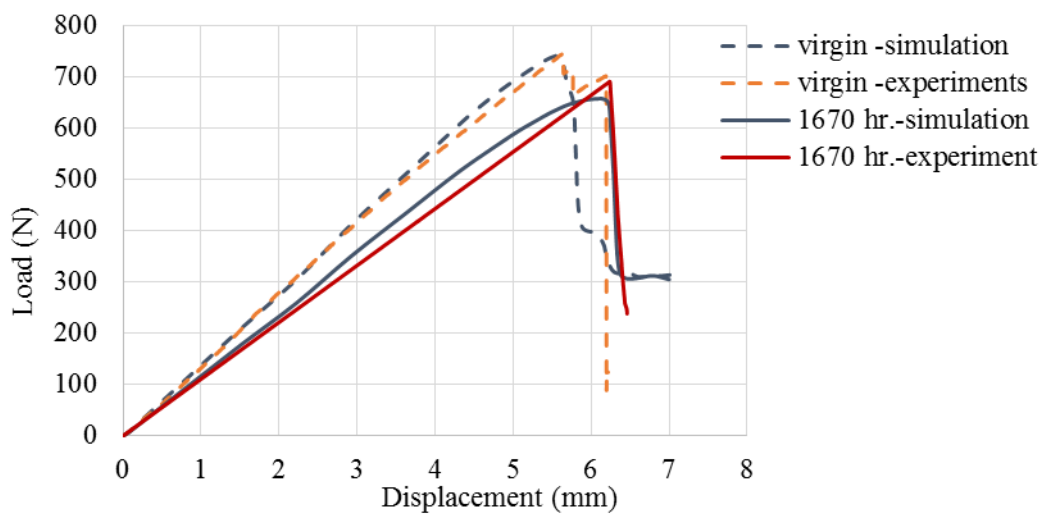
Figure 14. Load-displacement curves
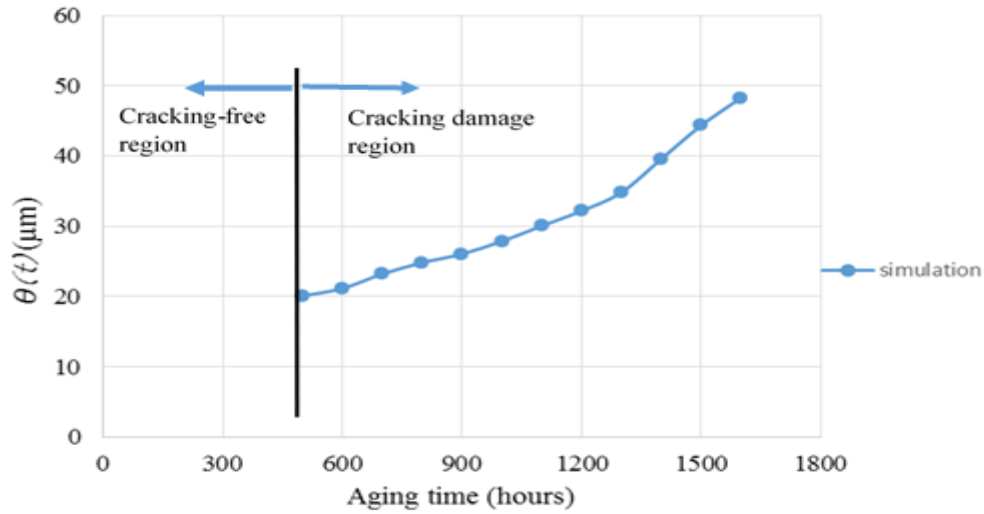
Figure 15. Average oxidized layer (through-thickness) vs. aging time

Table 1. Parameters used in diffusion-reaction and weight loss simulation

Parameter	Symbol	Value
Diffusivity of the unoxidized matrix (φ =1) [23]	D_0^{un}	1.62×10^{-4} mm^2/min
Diffusivity of the oxidized matrix ($\varphi = \varphi_{ox}$) [23]	D_0^{ox}	1.94×10^{-4} mm^2/min
Longitudinal fiber diffusivity[1]	D_L^f	$D_0^{un}/10^3$
Transverse fiber diffusivity[1]	D_T^f	$D_0^{un}/10^5$
Density of laminate *	ρ_c	1.57 g/cm^3
Density of unoxidized polymer matrix ***	ρ_o	1.24 g/cm^3
Fiber weight fraction**	W_f	65.3%
Density of fiber	ρ_f	1.78 g/cm^3
Fiber volume fraction***	V_f	57.66 %
Homogenized transverse-x diffusivity	D_X^{eff}	11.9×10^{-4} mm^2/min
Homogenized transverse-y diffusivity	D_Y^{eff}	62.7×10^{-4} mm^2/min
Homogenized longitudinal-z diffusivity	D_Z^{eff}	62.7×10^{-4} mm^2/min

* determined experimentally by water displacement according to ASTM D792   **manufacturer's data sheet

*** determined using calculation methods of ASTM D3171 [13]

Table 2. Material properties of the virgin unidirectional laminate

Property	Symbol	Value
Longitudinal tensile modulus[*]	$E_1^{\,0}$	142.03×10^9 Pa
Transverse tensile modulus[*]	$E_2^{\,0}$, $E_3^{\,0}$	11.03×10^9 Pa
Longitudinal Poisson's ratio[*]	$\nu_{12}^{\,0}$	0.29
Transverse Poisson's ratio[*]	$\nu_{21}^{\,0}$	0.4
Longitudinal shear modulus[*]	$G_{12}^{\,0}$, $G_{13}^{\,0}$	24.82×10^9 Pa
Transverse shear modulus[**]	$G_{23}^{\,0}$	3.94×10^9 Pa
Longitudinal tensile strength[*]	X^T	2.55×10^9 Pa
Longitudinal compressive strength[*]	X^C	1.74×10^9 Pa
Transverse tensile strength[*]	Y^T	48.26×10^6 Pa
Transverse compressive strength[*]	Y^C	45.1×10^6 Pa
Longitudinal shear strength[*]	S^L	1.61×10^8 Pa
Transverse shear strength[*]	S^T	2.25×10^8 Pa
Longitudinal tensile fracture energy[***]	F^{LT}	110×10^3 J/m^2
Longitudinal compressive fracture energy[***]	F^{LC}	25×10^3 J/m^2
Transverse tensile fracture energy[***]	F^{TT}	0.15×10^3 J/m^2
Transverse compressive fracture energy[***]	F^{TC}	0.45×10^3 J/m^2

[*] manufacturer's data sheet [**] determined using calculation methods of compliance terms [14] [***]Wang et al. [15]

Table 3. Constants for elastic reductions in the oxidation-dominated region

Constant	C_2A_1 (GPa)	C_2A_2 (GPa)	C_2A_4 (GPa)
Value	$-2.25\pm0.104\times10^9$	$1.38\pm0.064\times10^8$	$-1.58\pm0.073\times10^9$

REFERENCES

1) Schoeppner, G.A., Tandon, G.P. and Pochiraju, K.V. Multiscale Modeling and Simulation of Composite Materials and Structures, Springer, 2008.

2) Boyd, J., Bongiovanni, C.L. and Thai, B. ,Bismaleimide Resin with High Temperature Thermal Stability, U.S. Patent 2007/0117956 A1, May 24, 2007.

3) Pochiraju, K.V., Tandon, G.P. and Schoeppner, G.A., Evolution of Stress and Deformations in High-Temperature Polymer Matrix Composites During Thermo-oxidative Aging, Mechanics of Time-Dependent Materials, vol.12, p.p. 45–68, 2008

4) Schoeppner, G.A., Tandon, G.P. and Ripberger, E.R., Anisotropic Oxidation and Weight Loss in PMR-15 Composites, Composites: Part A , vol.38, p.p. 890–904, 2007.

5) Colin, X., Marais, C. and Verdu, J., Thermal Oxidation Kinetics for a Poly (bismaleimide), Journal of Applied Polymer Science , vol. 82, p.p. 3418–3430, 2001.

6) Roy, S., Sing, S. and Schoeppner, G.A., Modeling of Evolving Damage in High Temperature Polymer Matrix Composites Subjected to Thermal Oxidation, Journal of Materials Science , vol. 43, p.p. 6651–6660, 2008.

7) Roy, S. and Sing, S., Prediction of Thermo-Oxidative Degradation in Polymer Matrix Composites Using Micromechanical Modeling and Homogenization at the Macro-Scale, Mechanics of Advanced Materials and Structures , vol.19, p.p. 68–78, 2102.

8) Upadhyaya, P., Sing, S., and Roy, S.,A Mechanism-Based Multi-Scale Model for Predicting Thermo-Oxidative Degradation in High Temperature Polymer Matrix Composites, Composites Science and Technology , vol. 71, p.p. 1309–1315, 2011.

9)   Haque, M. H., Upadhyaya, P., Roy, S., Ware, T., Voit, W. and Lu, H.,The Changes in Flexural Properties and Microstructures of Carbon Fiber Bismaleimide Composite After Exposure to a High Temperature, Composite Structures , vol. 108, p.p. 57–64, 2014.

10) Meng, M., Le, H.R., Rizvi, M.J. and Grove, S.M., 3D FEA Modeling of Laminated Composites in Bending and Their Failure Mechanisms, Composite Structures , vol. 119, p.p. 693–708, 2015.

11) An, N. and Pochiraju, K., "Modeling Damage Growth in Oxidized High-Temperature Polymeric Composites," *The Journal of the Minerals, Metals & Materials Society (TMS)*, Vol. 65, pp. 246–255, 2013.

12) Liang, J. and Pochiraju, K., "Oxidation-Induced Damage Evolution in a Unidirectional Polymer Matrix Composite," *Journal of Composite Materials*, Vol. 49, pp. 1393–1406, 2015.

13) ASTM Standard D317−11, 2011, "Standard Test Methods for Constituent Content of Composite Materials" ASTM International, West Conshohocken, PA, 2011.

14) Tuttle, M.E., Structural Analysis of Polymeric Composite Materials, CRC Press 2003.

15) Wang, C., Gunnion, A., Orifici, A. and Rider, A., Residual Strength of Composite Laminates Containing Scarfed and Straight-Sided Holes, Composites Part A: Applied Science and Manufacturing, vol. 42, p.p. 1951-1961, 2011.

16) Vu, DQ., Gigliotti, M., and Lafarie-Frenot, M.C., The Effect of Thermo-Oxidation on Matrix Cracking of Cross-Ply [0/90]S Composite Laminates, Composites Part A, vol. 44, p.p. 114-121, 2013.

17) Hussein, R. M., Anadan, S., and Chandrashekhara, K., Anisotropic Oxidation Prediction using Optimized Weight Loss Behavior of Bismaleimide Composites, Journal of Materials Science, vol. 51, p.p. 7236–7253, 2016.

18) Chung, K., Seferis, J.C. and Nam, J.D., Investigation of Thermal Degradation Behavior of Polymeric Composites: Prediction of Thermal Cycling Effect from Isothermal Data, Composites: Part A, vol. 31, p.p. 945–957, 2000.

19) Lafarie-Frenot, M.C., Damage Mechanisms Induced by Cyclic Ply-stresses in carbon-epoxy laminates: environmental effects, International Journal of Fatigue, vol. 28, p.p.1202–1216, 2006.

20) Scheirs, J., Compositional and Failure Analysis of Polymers a Practical Approach, Wily, 2000.

21) McManus, H. L. and Chamis, C.C., Stress and Damage in Polymer Matrix Composite Materials Due to Material Degradation at High Temperatures, NASA Technical Memorandum 4682, 1996.

22) Painter, P.C. and Coleman, M.M., Fundamentals of Polymer Science: An Introductory Text, 2nd Edition, CRC Press, 1997.

23) Antoun, B., Qi, H.J., Hall, R., Tandon, G.P., Lu, H., Lu, C., Furmanski, J. and Amirkhizi, A., Challenges in Mechanics of Time-Dependent Materials and Processes in Conventional and Multifunctional Materials, vol. 2, Springer, 2014.

24) Talreja, R., "Multi-Scale Modeling in Damage Mechanics of Composite Materials." Journal of Materials Science, vol. 41, p.p. 6800–6812, 2006.

III. THERMO-OXIDATIVE INDUCED DAMAGE IN POLYMER COMPOSITES: MICROSTRUCTURE IMAGE-BASED MULTI-SCALE MODELING AND EXPERIMENTAL VALIDATION

Rafid M. Hussein and K. Chandrashekhara

Department of Mechanical and Aerospace Engineering

Missouri University of Science and Technology, Rolla, MO 65409

ABSTRACT

A multi-scale modeling approach is presented to simulate and validate thermo-oxidation shrinkage and cracking damage of a high temperature polymer composite. The multi-scale approach investigates coupled transient diffusion-reaction and static structural at macro- to micro-scale. The micro-scale shrinkage deformation and cracking damage are simulated and validated using 2D and 3D simulations. Localized shrinkage boundary conditions for the micro-scale simulations are determined from the respective meso- and macro-scale simulations, conducted for a cross-ply laminate. The meso-scale geometrical domain and the micro-scale geometry and mesh are developed using the object oriented finite element (OOF). The macro-scale shrinkage and weight loss are measured using unidirectional coupons and used to build the macro-shrinkage model. The cross-ply coupons are used to validate the macro-shrinkage model by the shrinkage profiles acquired using scanning electron images at the cracked surface. The macro-shrinkage model deformation shows a discrepancy when the micro-scale image-based cracking is computed. The local maximum shrinkage strain is assumed to be thirteen times the maximum macro-

shrinkage strain of 2.5×10-5, upon which the discrepancy is minimized. The micro-crack damage of the composite is modeled using a static elastic analysis with extended finite element and cohesive surfaces by considering the modulus spatial evolution. The 3D shrinkage displacements are fed to the model using node-wise boundary/domain conditions of the respective oxidized region. Micro-crack simulation results: length, meander, and opening are closely matched to the crack in the area of interest for the scanning electron images.

1. INTRODUCTION

The investigation of mechanical behavior and damage of composites entails the analysis of fiber and matrix and their respective spatial distribution in the composite domain. The distribution of fibers in the matrix is either random or indeterminate. Micro-scale damage is localized and dependent on the microstructural characteristic. An isomorphic microstructure can be built to closely model the composite behavior using finite element analysis (FEA). The National Institute of Standards and Technology (NIST) developed an object oriented finite element analysis (OOF) tool to analyze materials' behavior using microstructural images [1–4]. In the field of polymer composites/nanocomposites, OOF was used to investigate mechanical properties, especially the elastic modulus.

Goel et al. [5] investigated the elastic modulus of a chopped glass fiber and polypropylene matrix thermoplastic composite. Optical images were acquired for polished samples and meshed using triangular elements with OOF. The fiber volume fraction was

calculated from the images and used to estimate the modulus using analytical models. The analytical results showed a discrepancy from the experimental measurements. However, the predicted moduli using OOF were in a good agreement with the experimental findings. Dong and Bhattacharyya [6–7] built a model to determine the tensile modulus of polypropylene/organoclay nanocomposites at various clay contents using OOF. Scanning/transmission electron microscopy was utilized to capture the microstructural images. Quadrilateral mesh was generated for the images acquired by scanning and transmission electron microscopy in OOF and used for FEA simulations. Experimental results of the modulus were compared to the FEA results and six analytical models using different aspect ratios. In all cases, OOF-based modulus results showed a close match to the experimental outcomes.

High-temperature polymer matrix composites are susceptible to superficial thermal oxidation. During the propagation of oxidized layer, weight loss, density increase, and volumetric shrinkage take place. Due to volumetric shrinkage, strain and stress fields are built up, leading to matrix cracking [8]. Initiation and evolution of thermo-oxidation-induced cracking/damage at the micro-scale has not been investigated comprehensively in the literature. In the micro-scale, most of the previous investigations focused on the measurement/simulation of the shrinkage stresses/strains. Schoeppner et al. [9] presented a study on G30-500/PMR-15 unidirectional composites using representative volume elements (RVE) as a basis for diffusivity homogenization and oxidation shrinkage simulation. Simulation results determined that the peak stress due to lamina shrinkage after 200 hours of oxidation was located at the fiber matrix interface. Localized shrinkage due to thermo-oxidation of IM7/977-2 carbon/epoxy unidirectional laminate was studied by

Gigliotti et al. [10]. Viscoelastic polymer matrix behavior was coupled with a mechanistic diffusion-reaction scheme to model the local shrinkage of epoxy. Local shrinkage was measured using confocal interferometric spectroscopy and compared to the simulation. Results of shrinkage profiles indicated that volumetric shrinkage increased when the distance between fibers was increased.

Damage induced by thermo-oxidation was studied by a few investigators focusing on a homogenized composite domain. An and Pochiraju [11] simulated the oxidation and damage growth of bismaleimide (BMI) resin and cross-ply laminates. The analysis was implemented in the macro-scale for a neat resin plate subjected to bending and a laminated plate with a hole subjected to a tensile loading. The extended finite element method (XFEM) was used to simulate the crack propagation for the neat resin case, while the Hashin-Rotem law was used for damage initiation of the laminate case. Liang and Pochiraju [12] presented a simulation scheme for the isothermal oxidation damage of unidirectional carbon polyimide composites. The shrinkage strain was assumed orthotropic and homogenized for the unidirectional laminate. Damage initiation was analyzed using Hashin's failure criteria. XFEM, cohesive elements, and a traction-separation law were used for modeling crack initiation and propagation. The cracking growth simulation results were compared to axial and transverse oxidation cracking measurements. The results matched closely for the aging time up to 1600 hours. Daghia et al. [13] investigated the damage evolution in the transverse direction of oxidized superficial layers in thin cross-ply epoxy plates using a finite fracture mechanics approach. The damage kinetics was modeled in the meso-scale assuming a constant thickness of the oxidized layer to be half of the superficial ply thickness. A 2D FEA model was built to compute the strain energy change prior to and

after cracking to be used for the calculation of the strain energy release rate. Cracks were artificially introduced, and the strain energy release rate was computed by considering thermal and oxidation shrinkage strains for soaking and cooling to room temperature.

In the current work, thermo-oxidation and oxidation shrinkage were investigated using a multi-scale approach. A 3D multi-scale simulations were conducted for macro-, meso- and, micro-scale. The macro- and meso-scale simulations were used to determine the local boundary conditions to simulate the shrinkage and damage in the micro-scale. Two micro-scale cases were investigated: a 2D case for oxidative shrinkage using an image-based mesh created by OOF, and a 3D case for oxidative cracking by extending the 2D image-based geometry of the first case to 3D. In the 2D case, the oxidative shrinkage was simulated and compared to the shrinkage in the scanning electron image. In the 3D case, the cracking damage was modeled using a mixed-mode model and an XFEM approach. Aging experiments were conducted to measure weight loss and volumetric shrinkage using unidirectional bismaleimide laminates at 200 °C up to 1000 hours. Weight loss and volumetric shrinkage simulation results were then compared to the experimental findings. Another set of cross-ply laminate coupons were aged at 176 °C and used to validate the macro-shrinkage model in the micro-scale using scanning electron images.

2. MODELING OF THERMO-OXIDATION

Modeling of the transient thermo-oxidation was implemented in the homogenized RVE level to determine the oxidized layer and weight loss. The micro-scale weight loss results were scaled by respective area ratios to the macro-scale as detailed below. This

procedure can be used for any lay-up configuration; however, the RVE geometry should represent the microstructural aspects of the considered laminate. For a unidirectional laminate, the RVE geometry consisted of two fiber quarters centered at the rectangular matrix corners with dimensions 3.14 µm x 5.43 µm x 135 µm with fiber volume fraction of 57.66 %, as shown in Figure 1. The x- and y-coordinate of the RVE represented transverse direction (perpendicular to fibers). By introducing homogenized properties of the RVE, Fick's second law of diffusion with a reaction term, $R_{eff}(C, \phi^{eff})$, and a time-dependent oxidation state variable, $\phi^{eff}(t)$, can be represented as the following equations:

$$\frac{\partial C(x, y, z, t)}{\partial t} = \vec{\nabla} \cdot (D_{eff}(\phi^{eff})\vec{\nabla}C(x, y, z, t)) - R_{eff}(C, \phi^{eff}) \tag{1}$$

$$\frac{d\varphi^{eff}}{dt} = -\alpha(t, T)R_{eff}(C, \varphi^{eff}) \tag{2}$$

where C is the oxygen concentration; D_{eff} is the effective diffusivity; and $\alpha(t, T)$ is a fitted proportionality parameter depending on time and temperature. The proportionality parameter was determined by fitting weight loss simulation results to the respective experimental outcomes throughout the oxidation time. Thermo-oxidation modeling proceeds in time and space domains following the three-zone model representation. Assuming that the fiber is unoxidized during thermo-oxidation, homogenization of the diffusivity and reaction term in Equations (1) and (2) can be obtained using the rule of mixtures [14]:

$$D_{eff}(\varphi^{eff}, T) = D_{eff}{}^{un}(T)\{\frac{\varphi^{eff} - \varphi_{ox}^{eff}}{1 - \varphi_{ox}^{eff}}\} + D^{ox}(T)\{\frac{1 - \varphi^{eff}}{1 - \varphi_{ox}^{eff}}\} \tag{3}$$

$$R_{eff}(C, \phi^{eff}, T) = R_0^{eff}(T)\{\frac{\phi - \phi_{ox}^{eff}}{1 - \phi_{ox}^{eff}}\}[\frac{2\beta C}{1 + \beta C}(1 - \frac{\beta C}{2(1 + \beta C)})] \tag{4}$$

$$R_0^{eff}(T) = V_m R_0^m(T) \tag{5}$$

$$\varphi_{ox}^{eff} = \varphi_{ox}^m(1-V_f) + V_f \varphi_{ox}^f \tag{6}$$

where D_{eff}^{un} and D^{ox} are the unoxidized composite effective diffusivity and oxidized matrix diffusivity represented by Arrhenius forms, respectively. In the present simulation, the rule of mixtures was applied to the reaction rate constant, $R_0^m(T)$, and the oxidation state variable, φ_{ox}^m of matrix. As the fiber was assumed unoxidized, φ_{ox}^f was set equal to unity. In isothermal oxidation, temperature is constant in Equations (3) and (5).

The RVE orthotropic effective diffusivity can be estimated using the averaging method by solving a steady-state simulation for a unit volume RVE. The steady-state concentration field, $C(x, y, z)$, and the diffusivity tensor of the matrix and fiber, $D(x, y, z)$, were used to estimate the effective diffusivity by the volume averaging method [15]:

$$D_{eff}(i) = \int_0^a \int_0^b \int_0^c D_{iq}(x_1, x_2, x_3) \frac{\partial C(x_1, x_2, x_3)}{\partial x_i} dx_1 dx_2 dx_3 \qquad i, q = 1,2,3 \tag{7}$$

where D_{eff} is the homogenized diffusivity; D_{iq} is the diffusivity tensor of fiber and matrix; a, b, and c are the geometrical limits of the scaled RVE; and x_1, x_2, x_3 are x, y, z.

Henry's law for sorption was used to calculate oxygen concentration at the boundaries:

$$C\big|_b = S \times P \tag{8}$$

Solubility, S, is a temperature-independent parameter where $S = 3.61 \times 10^{-4}$ mol/m^3·Pa for BMI. Oxygen partial pressure, P, is calculated as 0.21 of the air pressure at the aging temperature.

The following integral was introduced for weight loss due to oxidation by considering an infinitesimal homogenized element of volume $dv = dxdydz$ undergoing thermal oxidation:

$$W_{loss}(t) = \rho_o \iiint\limits_{matrix} (1 - \varphi)dv \tag{9}$$

where ρ_0 is the density of the unoxidized polymer matrix calculated from the unoxidized composite density (ρ_c). A scaling procedure was introduced by the respective surface area ratio of the sample to RVE. In all cases, the sample's surface area was calculated from initial measurements in the longitudinal and transverse simulations:

$$W_{loss} = W_{loss}^r(x) \times \frac{A_x^s}{A_x^r} + W_{loss}^r(y) \times \frac{A_y^s}{A_y^r} + W_{loss}^r(z) \times \frac{A_z^s}{A_z^r} \tag{10}$$

where W_{loss} is the total weight loss in the sample's scale; $W_{loss}^r(x)$, $W_{loss}^r(y)$, and $W_{loss}^r(z)$ are the weight loss per RVE due to oxidation in x, y, and z calculated using the volume integral of Equation (9); and A_x^s and A_x^r are the areas of oxidation-exposed surface perpendicular to x-direction in the sample and the RVE, respectively. Similarly, A_y^s, A_z^s and A_y^r, A_z^r are the exposed surface areas in their respective scales and directions. The surface area ratio of the sample to the RVE was considered equivalent to a unique number that defines the number of RVEs in a surface area. Then, A_x^s / A_x^r was equivalent to the number of RVEs in the oxidation-exposed surfaces perpendicular to x-direction. A similar definition was introduced for A_y^s / A_y^r and A_z^s / A_z^r in their respective directions. The number of RVEs was constant based on the initial sample's area, even though matrix shrinkage had taken place throughout the oxidation process. The presence of cracks due to matrix shrinkage and residual stresses had an effect on the area ratios; however, the crack surface

area was hard to measure or calculate precisely. Fitting the simulation results to experimental results by introducing $\alpha(t,T)$ can handle the effect of the growing crack in the surface area. Time and temperature dependence of $\alpha(t,T)$ were assumed isotropic in longitudinal and transverse thermo-oxidation. All simulations in this section were implemented in COMSOL Multiphysics using the properties listed in Table 1.

3. MODELING VOLUMETRIC SHRINKAGE STRAINS

Shrinkage of matrix during thermo-oxidation produces strains in the composite, which varies linearly with $\varphi^{eff}(t)$ [16]:

$$\varepsilon_s(\phi^{eff}) = \varepsilon_s^{ox} \times \left(\frac{1 - \phi^{eff}}{1 - \phi_{ox}^{eff}} \right) \tag{11}$$

where ε_s is the linear shrinkage strain of the matrix due to oxidation. For a completely oxidized matrix, shrinkage strain attains its maximum value of ε_s^{ox}. The shrinkage strain of Equation (11) is isotropic and depends only on $\varphi^{eff}(t)$. Volumetric shrinkage measurements of unidirectional samples will be used to determine ε_s^{ox} by fitting simulation results to the experimental outcomes. It should be noted that the maximum shrinkage strain is a matrix property, which is lay-up and temperature-independent in the service temperature range of BMIs.

The volumetric shrinkage was modeled in the RVE micro-scale for the three principal directions of x, y, and z corresponding to transverse-x and -y and longitudinal-z. The volumetric shrinkage in the sample macro-scale, S_V, was determined using:

$$S_V = \frac{\Delta V}{V} \qquad (12)$$

where ΔV is the total change in volume due to oxidation shrinkage for a sample of initial volume V, as shown in Figure 2. It should be noted that the notation of Equation (10) was used in this figure. The later definition of volumetric shrinkage can be expanded as follows:

$$S_V = \frac{\Delta V}{V} = \frac{\Delta V_{Tx}}{V} + \frac{\Delta V_{Ty}}{V} + \frac{\Delta V_{Lz}}{V}$$

where ΔV_{Tx}, ΔV_{Ty} and ΔV_{Tz} are the components of volume change in x, y, and z. Reformulating the last equation by introducing the number of RVEs in a principal direction results in:

$$\frac{\Delta V_{Tx}}{V} = \frac{\Delta V_{RVEx} \times N_{RVEx}}{V_{RVEx} \times N_{RVEx}}$$

where ΔV_{RVEx} is the change in RVE volume due to oxidation in the x-direction and N_{RVEx} is the number of RVEs in the respective x-direction. Similar definitions for the change in volume and number of RVEs were used for the y- and z-directions. Substituting the last definitions of all principal directions in Equation (12) yields the total volumetric shrinkage in the sample scale:

$$S_V = \frac{\Delta V_{RVEx}}{V_{RVEx}} + \frac{\Delta V_{RVEy}}{V_{RVEy}} + \frac{\Delta V_{RVEz}}{V_{RVEz}} \qquad (13)$$

Elastic properties of the composite laminate for the oxidative shrinkage simulations are listed in Table 2. The simulation results were compared to the experimental measurements of the samples' shrinkage to determine the maximum oxidative shrinkage strain, ε_s^{ox}. This parameter was later used in the multi-scale modeling of the next part.

4. MULTI-SCALE MODELING OF SHRINKAGE DAMAGE

The analysis of this section was performed to investigate the volumetric shrinkage and cracking damage of the surface layer of a cross-ply laminate aged under 176 °C for 1000 hours. The homogenized diffusivities and proportionality parameter $\alpha(t,T)$ for the cross-ply laminate were determined elsewhere [25] and are listed in Table 3.

The important step in modeling a multi-scale domain is determining the boundary conditions for the meso- and micro-scale subdomains from the macro-scale domain. The modeling procedure of the current work was a 3D macro-scale simulation in the sample level, a 3D meso-scale simulation followed by two micro-scale simulations in 2D and 3D domains. Transient thermo-oxidation and static structural problems were solved at all scales by introducing the shrinkage strains of the previous section.

4.1 MACRO-SCALE MODELING

The geometrical domain of this simulation was equivalent to the real SEM sample in length dimension of 1 in. (0.0254 m). However, the depth was reduced to 1 mm to save computational time as shown in Figure 3. Due to symmetry, the macro-scale geometry was built using only the top 8 layers with smeared properties. For thermo-oxidation, the oxygen concentration boundary condition of $C_b = 7.678$ mol/m^3 was assigned to the faces pointed to by dashed arrows in the figure.

It should be noted that the front face of the laminate was assigned oxidation-free boundary condition as samples were cut periodically for 1000 hours, rendering the front face intact by oxidation. The top surface of the top layer, pointed to by the dashed arrow,

was assigned a displacement constraint in the x- and z-direction, allowing shrinkage displacement in the y-direction only. Due to symmetry, the bottom surface of the domain was constrained in the y-direction only by assigning a zero y-displacement.

4.2 MESO-SCALE MODELING

The meso-scale domain is shown in Figure 4 with the top layer highlighted and enlarged. The length and width were 1×10^{-4} m for the x-z cross-section. The depth composed of 8 layers, as was the macro-scale domain. Thermo-oxidation simulation was conducted by assigning an oxygen boundary condition of C_b for the top face of the first layer, as pointed to by a dashed arrow in Figure 4.

Fiber locations in the first layer were determined from the coordinates of the OOF mesh, shown in the next section, and extruded through the depth to generate 3D fiber and matrix domains. Extra fibers were added by duplication of the original fibers to the left, right, and bottom of the OOF mesh fibers to consider the effect of adjacent fibers on the micro-scale case. The left and right faces perpendicular to the x-direction, layers 2-8 from top to bottom, were assigned displacement boundary conditions in three principal directions. These boundary conditions were taken from the results of the macro-scale simulation and assigned to the respective faces. The bottom surface of layer 8 was constrained by assigning a zero displacement in the y-direction as in the macro-scale case.

4.3 MICRO-SCALE MODELING

The micro-scale models simulated 2D oxidative shrinkage and 3D cracking damage. The 2D case used an OOF-generated mesh to solve for the oxidative shrinkage.

The 3D case utilized the geometrical distribution of fibers in the OOF mesh to build the 3D geometry for crack simulation.

4.3.1 2D Micro-Scale. A 2D transient thermo-oxidation was run to determine the oxidation distribution using a quad-based mesh generated for a scanning electron micrograph of a superficial layer in a cross-ply laminate. The laminate was aged for 500 hours under the conditions described in the experimental part of this work. The simulation aimed to analyze the local shrinkage due to oxidative strain. The mesh was created using OOF by pixel discretizing of the image shown in Figure 5.

This mesh was generated using 80 quad elements for the x- and y-direction of the mesh skeleton. The skeleton elements of the fiber/matrix interface region was refined once using a default refinement to ensure a good mesh representation of the interface region. The final mesh consisted of about 25,000 quad elements grouped by 36-fiber and a matrix domain. The mesh was imported to Nastran and the element type was converted to CQUAD4, which is a 4-node plain strain element that is compatible with Comsol.

The oxidation evolution over 1000 hours was simulated using a two-coefficient form partial differential model for fiber and matrix domains. The oxygen boundary condition of Cb was imposed on the top line of the mesh only where oxidation evolves in y-direction. The oxidized layer shrinkage followed the linear strain that was introduced as the input for a static elastic model. The displacement boundary conditions for the elastic structural model were taken from the meso-scale model and imposed as a linear-spline function generated using Comsol. These boundary conditions were imposed on the left, right, and bottom lines of the mesh.

4.3.2 3D Micro-Scale. Oxidation-induced cracking was modeled in a 3D domain to account for a mixed-mode cracking where the displacement in the z-direction was considered as shown in Figure 6. Orange arrows represent the oxidized layer nodes of the matrix (colored green), blue arrows represent fiber constraints. The 3D domain was created in Abaqus using the geometrical distribution of fibers in the OOF mesh. The 3D micro-domain was created in the mid-distance of depth (z-direction) of the first layer in the meso-scale domain. The dimensions of the micro-domain were 33.75 µm x 32 µm x 0.5 µm. Due to the limitations of a small geometric representation in Abaqus, the unit length was set to 1 µm, and all material properties were scaled accordingly. The boundary conditions were imported from Comsol in the input file per node by creating sets for completely oxidized nodes. A total of 2886 sets were created and assigned displacement boundary conditions in a 3D frame for the matrix nodes only (marked by orange arrows). Only fiber nodes of the front surfaces were constrained by assigning zero displacement in the z-direction. As fibers are unoxidized and have a larger modulus compared to a matrix, the fiber faces' constraint was warranted.

In the present work, the crack initiation and propagation were modeled using the XFEM under the traction-separation cohesive behavior. The crack interaction was defined using a separate set to include the enrichment degrees of freedom for the XFEM crack, as shown in Figure 7(a). No constraints were imposed on the crack path, which was arbitrary and solution-dependent in the defined set. The crack interaction set was also created to localize cracking damage and take into consideration the strength and toughness variability throughout the composite. Mechanical properties of a composite vary from point to point due to microstructural heterogeneity [23]. Lamina strength variation is dependent on fiber

spacing, void distribution, and microstructural changes due to oxidation [24]. However, mechanical properties of all elements inside all sets were assumed constant.

In the XFEM, the finite element approximation is enriched with discontinuous terms to account for the crack tip and crack surface singularities. For a 1D standard XFEM approximation [19]:

$$u(x) = \sum_{j=1}^{n} u_j \psi_j(x) + \sum_{j=1}^{m} a_j \psi^*_j(x) H_j(x) \tag{14}$$

where u_j, $\psi_j(x)$ and $H_j(x)$ are the nodal displacement, normal shape function and the enrichment function. The function $\psi^*_j(x)$ is also a normal shape function that can be equal to $\psi_j(x)$. The enriched degree of freedom, a_j is defined for each node in the enriched domain of nodes m. Details of the XFEM derivation and implementation for the fracture and delamination in composites are out of the scope of the current work and can be found in [20, 21].

The fiber/matrix interface was defined as a cohesive surface transmitting the shrinkage displacements to the fibers. The evolution of the oxidized layer was accompanied by a change in elastic properties that was proportional to the oxidation state. The modulus evolution after 1000 hours of aging was accounted for by defining three materials' sets in Abaqus. These materials' sets represented the completely oxidized (blue-colored), active oxidation (gray-colored), and intact matrix (green-colored) materials marked by colored elements from top to bottom, as shown in Figure 7(b). The modulus evolution was assumed linearly-dependent on the oxidation state for the range 4.6 GPa $\leq E(\phi) \leq$ 5.2 GPa [11].

A maximum principal stress criterion was adopted to determine the failure initiation of the matrix and cohesive interfaces. The damage evolution was modeled using a bilinear

traction-separation law with a mixed mode behavior, as shown in Figure 8. Oxidation shrinkage induces stresses elastically until the critical maximum principal stress, Smax, is reached where cracking damage starts and evolves up to the maximum separation, δmax, which is determined by the fracture energy, G(δ). A fracture energy-based Benzeggagh–Kenane (BK) criterion was selected for the mixed-mode cracking behavior with the power parameter set to unity. Due to the mixed-mode fracture, normal and shear mode energies were assumed constant and independent of the oxidation state. The cohesive surfaces between the fibers and matrix were assigned stiffness constants of unity. The damage initiation maximum stresses and fracture energies of the matrix, cohesive surfaces are listed in Table 4.

5. EXPERIMENTAL PROCEDURE

Unidirectional test specimens measuring 3 in. x 3 in. (76.2 mm x 76.2 mm) were cut from a unidirectional laminate using a low speed saw. Samples were dried in a convection oven at 70 °C for 20 hours. Initial weights and dimensions were measured, and samples were placed in the oven for aging at 200 °C. Test samples were removed at regular intervals so that the weight loss and volumetric shrinkage could be recorded. A pressure vessel was required to conduct aging studies in argon. A cylindrical steel vessel, 50 cm long with an inside diameter of 10 cm, was used (Figure 9). Samples were placed inside the pressure vessel, which was then filled with argon at 38.32±3 kPa at room temperature. The pressure inside the vessel was about 101.32 kPa at 176 °C.

Seven samples were used to obtain weight loss measurements, four in air and three in argon. Two samples were used for measuring volumetric shrinkage in both cases. Samples were allowed to cool down for 15 minutes inside the oven and moved to a desiccator. Samples were then allowed to cool down to room temperature under vacuum. As recommended by ASTM D2126, fifteen measurements were taken per sample using a micrometer to calculate volumetric shrinkage. Sample mass was measured using a high precision balance with a least count of 0.1 mg.

Two coupons of a cross-ply laminate measuring 6 in. x 1 in. (152.4 mm x 25.4 mm) were also aged under similar conditions. These were used to cut the scanning electron microscopy (SEM) samples upon removal of the coupons from the oven. SEM samples were embedded in epoxy and polished progressively. The SEM images were acquired by a dual-beam Helios 600 electron microscope using an accelerating voltage of 5 kV and a beam current of 43 pA. The working distance was in the range of 3.4 to 4.4 mm.

6. RESULTS AND DISCUSSION

6.1 THERMO-OXIDATION MODELING AND EXPERIMENTS

Results of thermo-oxidative aging are shown in Figure 10(a). The weight loss of samples in air was higher than the weight loss in argon for all aging hours. The average weight loss ratio was 0.72 % and 0.12 % at 1000 hours for air-aged and argon-aged coupons. The weight loss of both cases was linearly-dependent on aging time with a constant rate. These results indicate that the major cause of weight loss is an oxidation

reaction. The contribution of polymer decomposition to weight loss in argon was insignificant.

A comparison of the weight loss simulation results and experimental findings are shown in Figure 10(b). The depicted results in the figure represent the total weight loss by incorporating the average percent contribution of polymer decomposition weight loss. Since the weight loss rate was approximately constant for the aging hours of this work, it was assumed that the proportionality parameter is one equation. Details of the weight loss simulation and scaling can be found in the author's previous work [26]. The proportionality parameter was estimated by fitting simulation and experimental weight loss:

$$\alpha(t) = 4.5 \times 10^{-5} e^{(7.5 \times 10^{-7} \times t)} \tag{15}$$

where t is the aging time in seconds.

Volumetric shrinkage was measured using the volume difference between aged and unaged samples. The average volumetric shrinkage of two samples was taken as the final result. Measurements were started at 500 hours when relatively measurable shrinkage was expected, as shown in Figure 11(a). The contribution of oxidation in weight loss and volumetric shrinkage is the difference between air-aged and argon-aged outcomes. The contribution of oxidation in weight loss was much higher than its contribution in volumetric shrinkage where polymer decomposition contributed significantly in the later. However, oxidative shrinkage was more significant in producing micro-cracks due to the constraint of the un-oxidized region. Polymer decomposition shrinkage was insignificant in producing micro-cracking damage as it happened through the whole polymer volume. In Figure 11(b), the maximum oxidative macro-shrinkage strain was determined by fitting the simulation and experimental results:

$$\varepsilon_s^{ox} = 2.5 \times 10^{-5} \tag{16}$$

The simulation results are closely fitted to the experimental measurements using the proposed maximum shrinkage strain. Similar to the weight loss behavior, the shrinkage behavior followed a constant rate for linear dependence on aging time.

6.2 MULTI-SCALE MODELING RESULTS

All simulations in this section were run at 176 °C up to 1,000 hours to validate the oxidation shrinkage and cracking damage using 16-layer cross-ply numerical samples.

6.2.1 Macro-Scale and Meso-Scale Simulations. The oxidation state and shrinkage displacement fields of the macro-scale are shown in Figure 12 for half of the domain, due to symmetry. The meso-domain is enlarged to show dimensions and location. The 3D displacement boundary conditions of the left and right faces of the meso-scale domain were extracted from the macro-scale results and converted to 2D linear interpolation functions. Layers 1-8 from top to bottom are shown in Figure 12(a). The displacement spike at the corner of the domain resulted from the numerical interaction between shrinkage in the z- and x-directions. However, the effect of the spike was minimal on the extracted boundary displacements. As mentioned in the modeling section, the interpolated boundary conditions will be applied to the right and left faces of layers 2-8 for the meso-scale simulation.

In Figure 13, the oxidation state and shrinkage displacement evolution for the meso-scale simulation are shown. The first layer was enlarged to show the displacement and oxidation fields of the micro-domain. The 3D displacement boundary conditions for the micro-scale model were extracted from the results of the meso-scale simulation. The

displacement boundary conditions were extracted for the front face of the micro-domain; front face is perpendicular to the y-direction, as shown in Figure 13(b). The effect of fiber distribution on the shrinkage displacement is significant. The maximum shrinkage was located at the resin-rich region of the oxidized superficial layer. These boundary conditions were then applied to the 3D and 2D micro-scale simulations to investigate the shrinkage deformation and cracking, respectively.

6.2.2 Micro-Scale Simulation (2D). The oxidation state, displacements in the x- and y-directions (u and v), and the second principal stress ($\sigma 22$) distribution for 500 hours of aging are shown in Figure 14. The results of this part were based on a local maximum shrinkage strain, as will be discussed later. In Figure 14(a), the oxidation state evolution is plotted for the composite domain. The completely oxidized layer evolved for a couple of microns, leading to the shrinkage of the exposed surface. The average oxidized layer thickness was about 7.5 µm. The oxidation shrinkage displacements are shown in Figure 14(b and c). The area of interest is marked by the arrow, where the region was under compression due to u displacement and downward stretch due to v displacement. The combined effect of the shrinkage displacements produced a compressive second principal stress ($\sigma 22$), as shown in Figure 14(d). However, there were tensile stresses located at the fiber/matrix interfaces where the failure was expected to start. The concentration of stresses also favors the failure to start at the inner interfaces instead of the oxidation-exposed edge/surface. The magnitude of the tensile/compressive stresses were dependent on the elastic properties difference between fiber and matrix and the evolved shrinkage strain. It should be noted that the fiber volume fraction was also calculated for the simulated domains which yielded a value close to the globally calculated fiber volume fraction.

The global maximum shrinkage strain $\varepsilon_s^{ox} = 2.5 \times 10^{-5}$ was used first to simulate the shrinkage deformations and stresses. Simultaneously, cracking damage simulations were run, which showed that the global shrinkage strain was smaller to produce a crack of around 30 µm during the first 500 hours of aging. Since the maximum shrinkage strain was a matrix property and due to the heterogeneity in matrix properties discussed earlier, it was assumed that the maximum shrinkage strain had a local variation. When the maximum shrinkage strain was scaled up by 13 to $\varepsilon_s^{ox}(local) = 3.25 \times 10^{-4}$, the cracking meander and length matched closely. Accordingly, this local value was used to produce the results in Figure 14.

6.2.3 Micro-Scale Simulation (3D). The oxidative micro-cracking or "spontaneous cracking" steps and mechanism are presented in this section. Multiple crack initiations were proposed using three materilas' sets intersecting an XFEM crack set. The implicit solver was used to march through the time steps of boundary/domain displacement ramp. The cracking progress through the XFEM domain is shown in Figure 15.

The maximum principal stress was satisfied at multiple locations leading to multiple crack initiations at the fiber/matrix region, as shown in Figure 15 (a). The evolution of these micro-cracks led to the formation of the final crack shown in Figure 15 (b). The maximum principal stress criterion was reached at multiple elements where the STATUSXFEM had a value greater than zero. The STATUSXFEM continued to increase until it reached a value of unity (Figure 15 (b)) in one of the elements that was completely damaged based on the traction-separation law.

However, the real crack in the SEM image was a single crack, though multiple micro-cracks initiations were also possible. The degradation of the fiber/matrix interfacial strength due to oxidation and polymer decomposition was sparse due to the spatial distribution of fibers in the matrix. Further, the average oxidized layer thickness by simulation was 7.5 µm, which was 25 % of the crack length of 30 µm, based on the SEM image measurement. These results raise the possibility of crack initiation due to interfacial strength degradation rather than matrix oxidation. Matrix oxidation formed a stiffer oxidized layer with a higher modulus than the unoxidized matrix, which was also a possible reason behind the cracking of the inner matrix/interfaces. However, multiple crack initiations and interfacial debondings were not recognized by SEM, which requires timely monitoring with further investigation. The fracture energy and the maximum principal stress were reduced in the order of 10^{-6} and 10^{-12} of the values used in the literature for BMI [11]. The literature strength values were smeared for a laminate that does not reflect the local variation in the micro-scale. The remarkable reduction was attributed to the effect of polymer embrittlement induced by thermo-oxidation. Reducing the material's properties was practical, since previous studies showed a dramatic decrease of 98% in the ductility of polypropylene tensile coupons after 150 hours exposure at 90 °C [22]. However, the validity of the tensile coupons was limited to the sample scale where tests are generally conducted. Precise measurements of the local properties for a composite is challenging and requires efficient simulation to investigate the degradation and damage reaching better assessments of the composite behavior at lower scales.

The crack length, meander, and opening are well simulated using the multi-scale approach of the current work, as shown in Figure 16. However, the crack length did not

exactly match. The shrinkage of the real SEM image was not directly comparable to the simulation shrinkage due to the difference in scale. The shrinkage displacement of 1.809×10^{-3} µm happened at 500 hours of aging, leading to the crack formation. It should be noted that the results were based on assumed fracture energy and maximum principal stress, the determination of which is challenging. The real scenario of damage events was assumed and simulated, but it needs to be generalized for multiple cases where the issue of the locality is challenging.

7. CONCLUSIONS

High-temperature polymer matrix composites are used under extreme environments where thermo-oxidation is the dominating degradation mechanism. Better understanding of the degradation and the associated shrinkage and cracking damage is required to predict the mechanical behavior and service life. In the current work, a multiscale approach was proposed to simulate the shrinkage deformation and micro-scale cracking damage. The effects of the global thermo-oxidation on the local boundary conditions were considered by running macro- and meso-scale simulations and extracting the induced 3D displacements (u, v, and w). These displacement boundary conditions were then applied to the respective micro-scale simulations utilizing an OOF-generated mesh and geometry. The oxidative macro-shrinkage strain was assumed linearly dependent on the oxidation state variable and attains its maximum value $\varepsilon_s^{ox} = 2.5 \times 10^{-5}$ when the matrix is completely oxidized. The maximum shrinkage strain was assumed as a material property determined by measuring the volumetric shrinkage of a unidirectional coupons

aged under 200 °C. However, the local value of the maximum shrinkage strain was $\varepsilon_s^{ox}(local) = 3.25 \times 10^{-4}$ and had the local crack matched to the SEM image measurements. This suggested a distribution of the form $\varepsilon_s^{ox}(local) = f(x, y, z)$ similar to all material properties.

Since testing is not practical at the local scale, powerful simulation schemes are necessary under reasonable assumptions especially, the boundary conditions. The micro-cracking was validated using a 3D static simulation to the OOF- generated/replicated mesh and geometrical domain. Despite, the transient nature, cooling/heating cycles during aging, and the evolution of the thermal transport and thermal expansion coefficient being not considered, the cracking simulation results were good. The reduction in the fracture energy and the maximum principal stress was in the order of 10^{-6} and 10^{-12} of the smeared values used in the literature for BMI. This was attributed to the oxidation-induced embrittlement and the effects of local stress concentration at the fiber/matrix interface. The interfacial strength was also considered to be in the same level of reduction for the cohesive surface contacts. Not only was the crack length closely simulated, but also the crack meander and opening. However, the procedure was validated for a real crack; a plethora of future validation cases are required to generalize the approach.
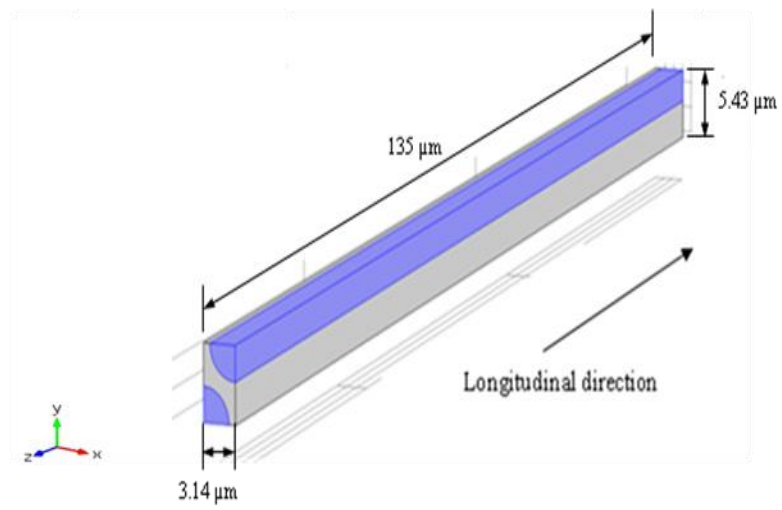
Figure 1. RVE geometry of a unidirectional lay-up (fibers are highlighted)
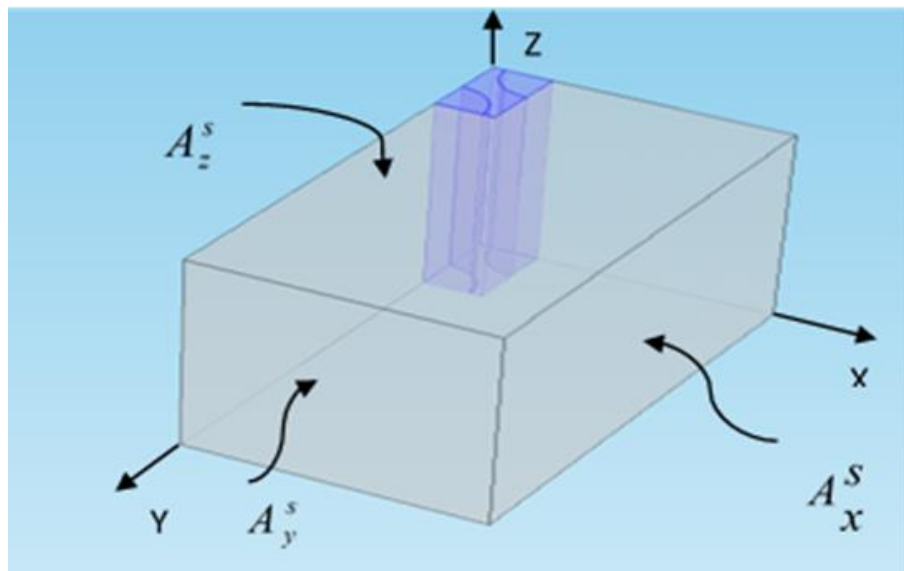

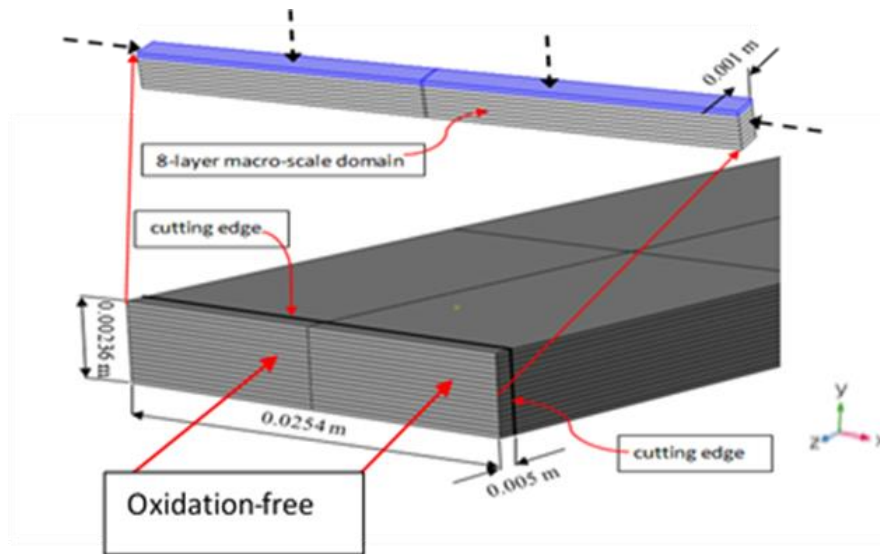Figure 2. Schematic of a unidirectional sample with initial volume *V*

Figure 3. Eight-layer macro-scale domain (top layer is highlighted)
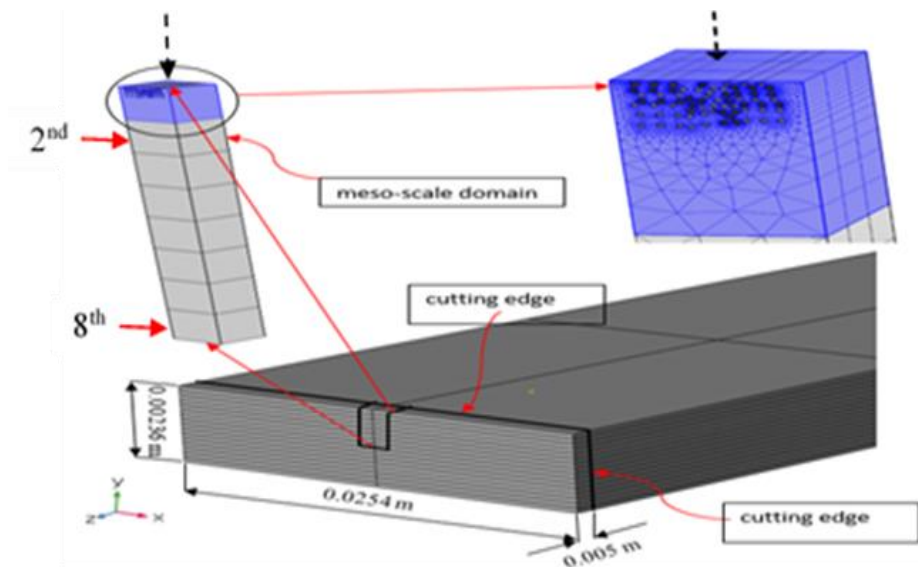

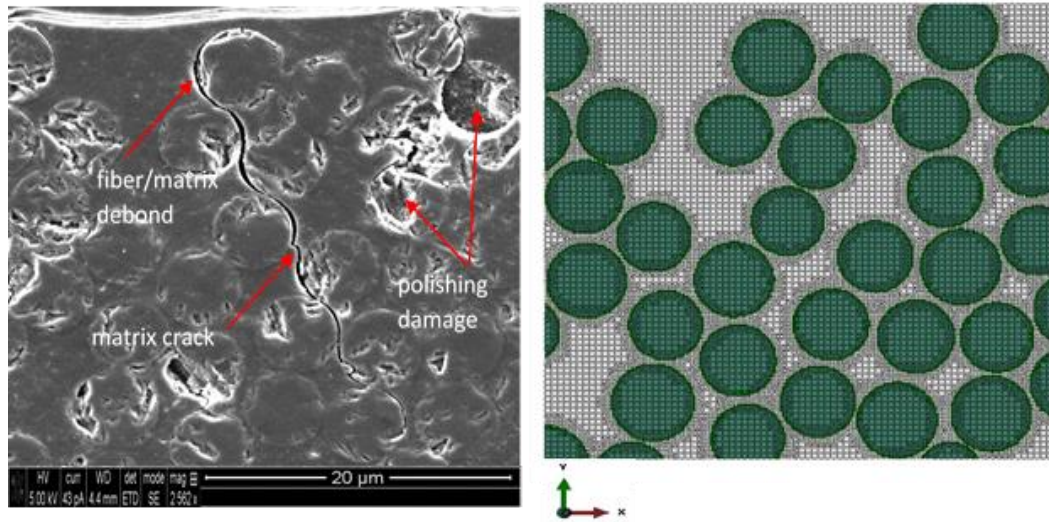Figure 4. Meso-scale domain (top layer matrix is highlighted)

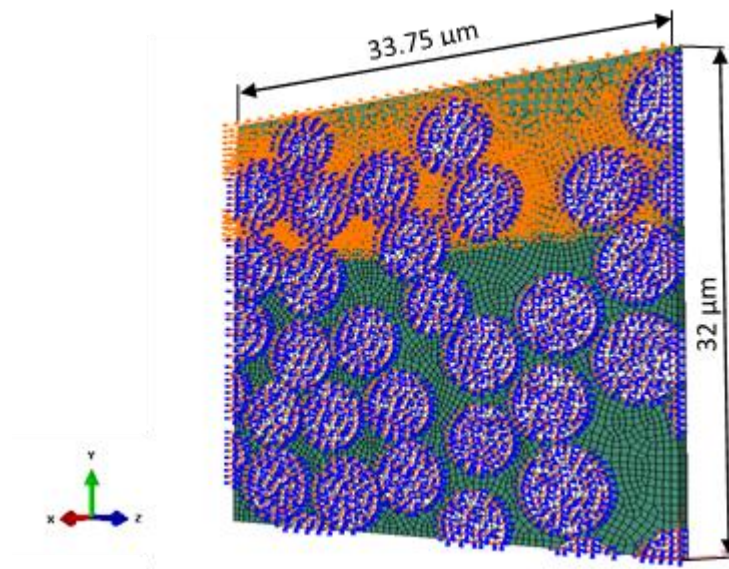Figure 5. The scanning electron micrograph and the respective OOF mesh

Figure 6. 3D damage model and boundary conditions
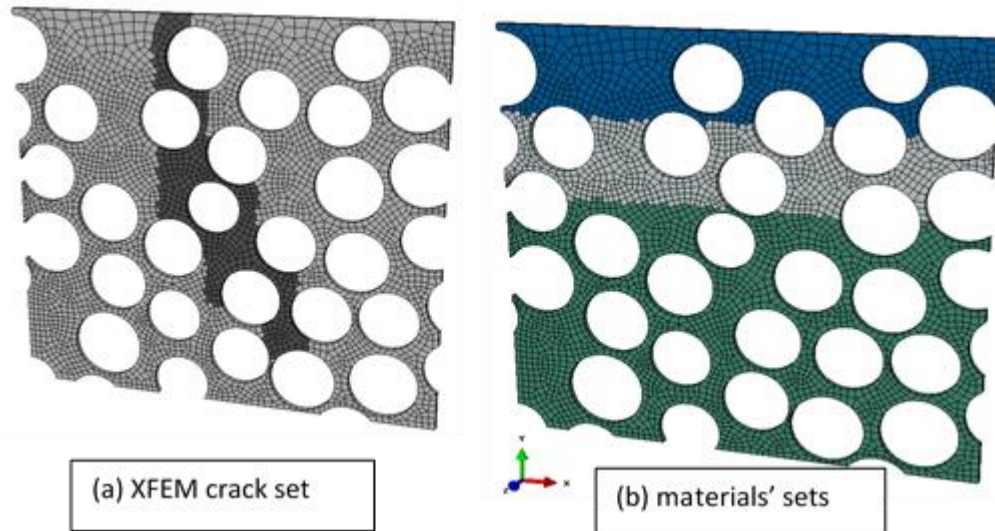
Figure 7. Matrix materials' and XEFM crack sets
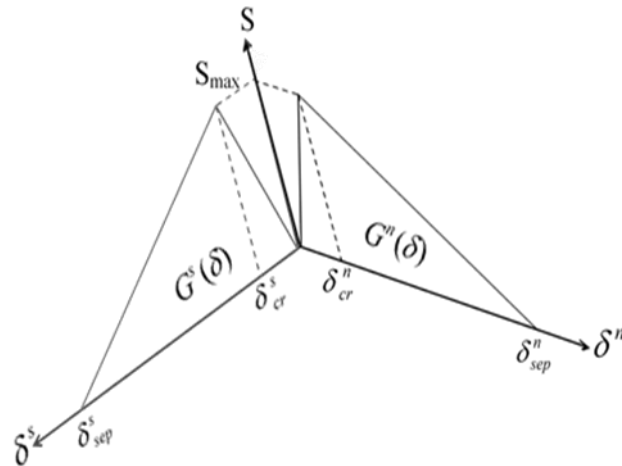
Figure 8. Traction-separation law for damage evolution

Figure 9. Chamber setup used for argon aging
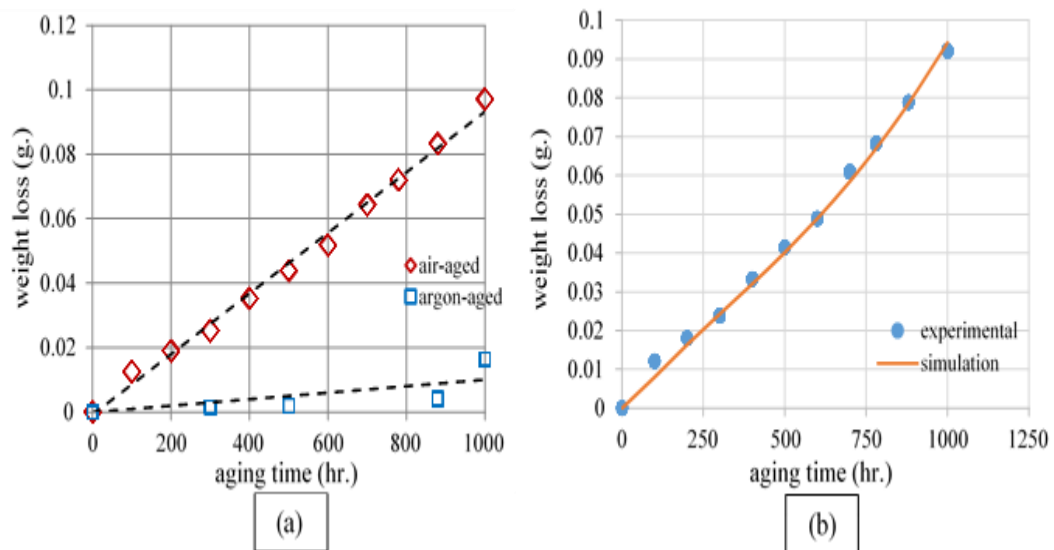
Figure 10. Weight loss results (a) experimental and (b) comparison with simulation
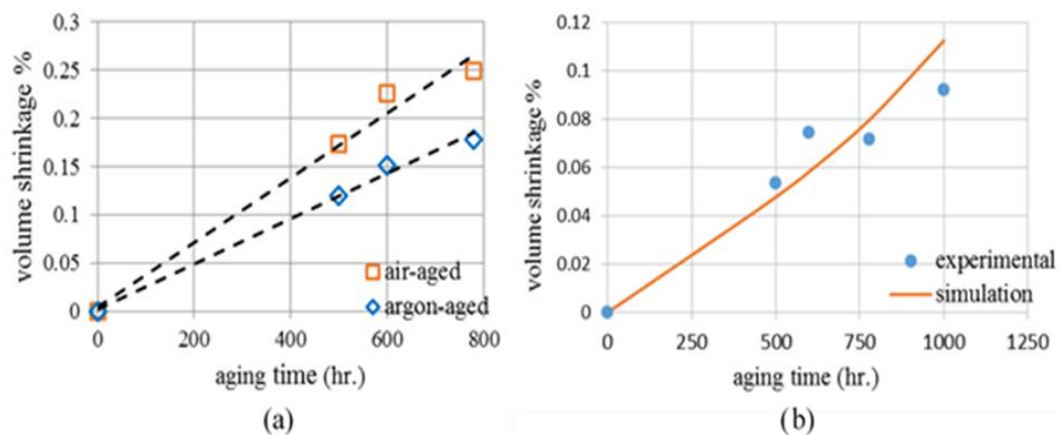
Figure 11. Volumetric shrinkage (a) experimental and (b) a comparison
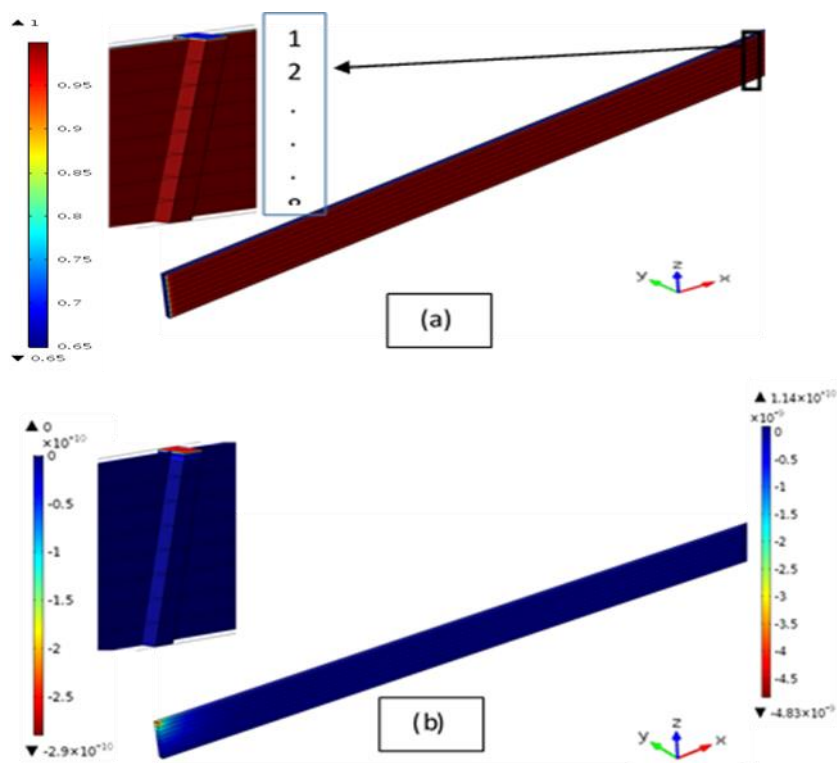
Figure 12. Macro-scale (a) oxidation state and (b) shrinkage displacement (w)

Figure 13. Meso-scale (a) oxidation state and (b) z-shrinkage displacement (w)

Figure 14. Results of oxidation state, shrinkage displacements, and σ_{22}

Figure 15. 3D Micro-scale STATUSXFEM

Figure 16. A comparison between SEM image and simulation

Table 1. Parameters used in oxidation simulation of a unidirectional laminate

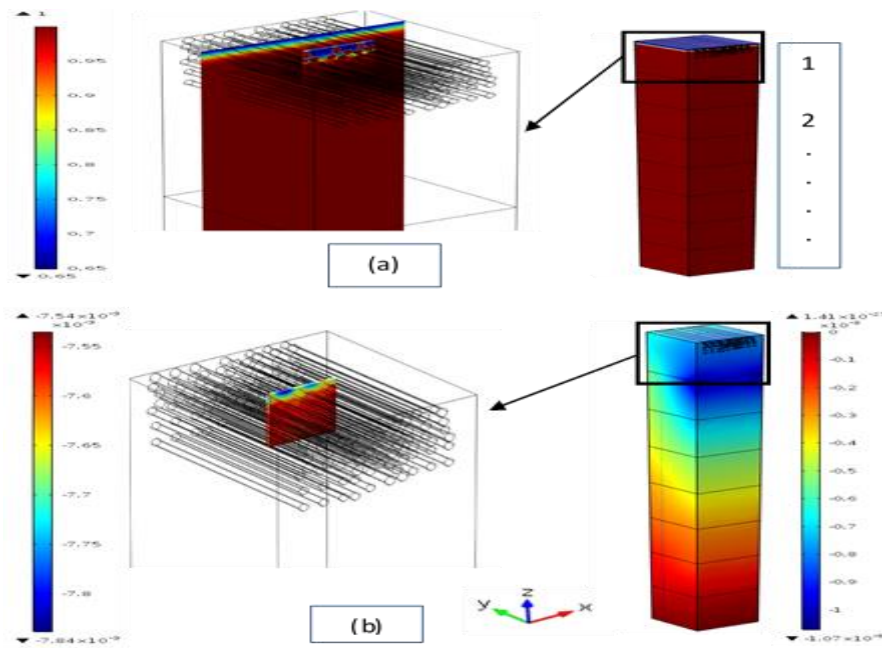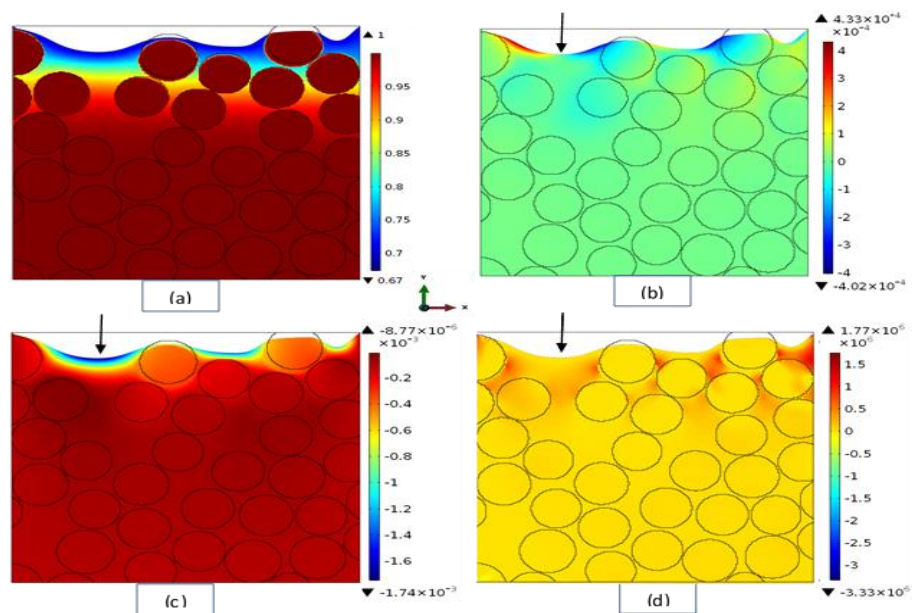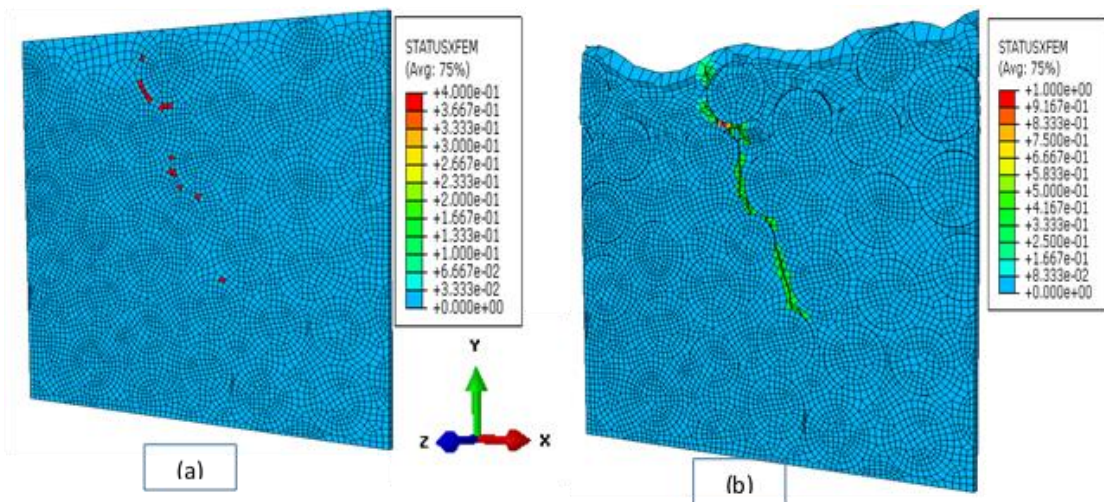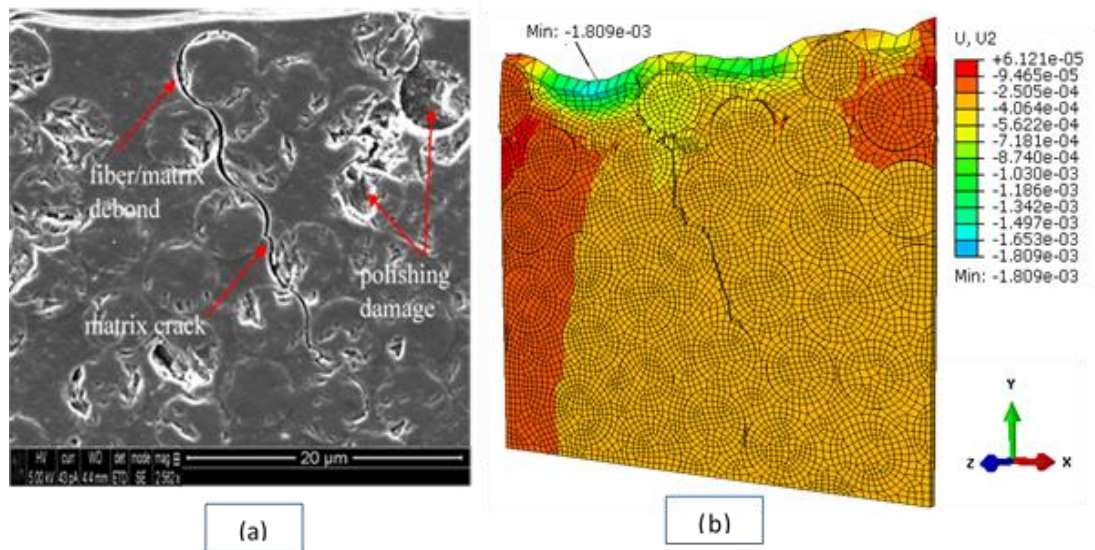| Parameter	Symbol	Value
Diffusivity of the unoxidized matrix ($\varphi = 1$)	D_0^{un}	1.62×10^{-4} mm^2/min
Diffusivity of the oxidized matrix ($\varphi = \varphi_{ox}$)	D_0^{ox}	1.94×10^{-4} mm^2/min
Longitudinal fiber diffusivity	D_L^f	$D_0^{un}/10^3$
Transverse fiber diffusivity	D_T^f	$D_0^{un}/10^5$
Density of laminate [*]	ρ_c	1.57 g/cm^3
Density of unoxidized polymer matrix [***]	ρ_o	1.24 g/cm^3
Fiber weight fraction[**]	W_f	65.3%
Density of fiber	ρ_f	1.78 g/cm^3
Fiber volume fraction[***]	V_f	57.66 %
Homogenized transverse-x diffusivity	D_X^{eff}	5.69×10^{-5} mm^2/min
Homogenized transverse-y diffusivity	D_Y^{eff}	3.29×10^{-5} mm^2/min
Homogenized longitudinal-z diffusivity	D_Z^{eff}	6.86×10^{-4} mm^2/min

* determined experimentally by water displacement according to ASTM D792   **manufacturer's data sheet

*** determined using calculation methods of ASTM D3171

Table 2. Elastic constants of the homogenized RVE

Property	Symbol	Value
Longitudinal tensile modulus[*]	E_{zz}	142.03×10^9 Pa
Transverse tensile modulus[*]	E_{xx}, E_{yy}	11.03×10^9 Pa
Longitudinal Poisson's ratio[**]	ν_{xy}	0.4
Transverse Poisson's ratio[*]	ν_{zy}, ν_{zx}	0.29
Longitudinal shear modulus[***]	G_{xy}	16.11×10^9 Pa
Transverse shear modulus[*]	G_{zx}, G_{zy}	24.82×10^9 Pa

* manufacturer's data sheet   ** Haque et al. [17]   *** determined using calculation methods of compliance terms [18]

Table 3. Homogenized cross-ply diffusion-reaction parameters

Parameter	Symbol	Value
Homogenized transverse-x diffusivity[*]	D_X^{eff}	11.9×10^{-4} mm^2/min
Homogenized transverse-y diffusivity	D_Y^{eff}	62.7×10^{-4} mm^2/min
Homogenized longitudinal-z diffusivity	D_Z^{eff}	62.7×10^{-4} mm^2/min
Proportionality parameter	$\alpha(t,T)$	$\begin{cases} 25 \times 10^{-5}, & t \leq 200 hr. \\ 1.8 \times 10^{-5} e^{(6.75 \times 10^{-7} \times t)}, & t > 200 hr. \end{cases}$

* through-thickness diffusivity

Table 4. Damage initiation and propagation properties

Property	Symbol	Value
Maximum principal stress (unoxidized matrix)	S_{max}	1.6×10^{-5} Pa
Maximum principal stress (oxidized/active oxidation matrix)	S'_{max}	1.6×10^{-5} Pa
Maximum nominal stress (cohesive surfaces)	S_n	$S_{max}/1000$
Fracture energy	G	1×10^{-5} J/m^2
Viscosity stabilization coefficient	v_s	1×10^{-4}

REFERENCES

1) Langer S., Fuller E. R., and Carter W. C., "OOF: An Image-Based Finite-Element Analysis of   Material Microstructures," Computing in Science and Engineering, Vol. 3, pp. 15–23, 2001.

2) Reid A. C. E., Langer S. A., Lua R. C., Coffman V. R., Haan S.–I., and Garcia R. E., "Image-Based Finite Element Mesh Construction for Material Microstructures," Computational Material Science, Vol. 43, pp. 989–999, 2008.

3) Reid A. C. E., Lua R. C., Garcia R. E., Coffman V. R., and Langer S. A., "Modeling Microstructures with OOF2," International Journal of Materials and Product Technology, Vol. 35, pp. 361–373, 2009.

4) Coffman V. R., Reid A. C. E., Langer S. A., and Dogan G., "OOF3D: An Image-Based Finite Element Solver for Materials Science," Mathematics and Computers in Simulation, Vol. 82, pp. 2951–2961, 2012.

5) Goel A., Chawla K.K., Vaidya U.K., Chawla N. and Koopman M., "Two Dimensional Microstructure Based Modeling of Young's Modulus of Long Fibre Thermoplastic Composite," Materials Science and Technology, Vol. 24, pp. 864–869, 2008.

6) Dong Y. and Bhattacharyya D., "Two Dimensional Microstructure Based Modeling of Young's Modulus of Long Fibre Thermoplastic Composite," Mechanics of Advanced Materials and Structures, Vol. 17, pp. 534–541, 2010.

7) Dong Y. and Bhattacharyya D., "Mapping the Real Micro/Nanostructures for the Prediction of Elastic Moduli of Polypropylene/Clay Nanocomposites," Polymer, Vol. 51, pp. 816–824, 2010.

8) Decelle J., Huet N. and Bellenger V., "Oxidation Induced Shrinkage for Thermally Aged Epoxy Networks," Polymer Degradation and Stability, Vol.81, pp.239–248, 2003.

9) Pochiraju K.V., Tandon G.P. and Schoeppner G.A., "Evolution of Stress and Deformations in High-Temperature Polymer Matrix Composites During Thermo-oxidative Aging," Mechanics of Time-Dependent Materials, Vol.12, pp.45–68, 2008.

10) Gigliotti M., Olivier L., Vu D. Q. and Grandidier J., and Lafarie-Frenot M.C., "Local Shrinkage and Stress Induced by Thermo-Oxidation in Composite Materials at High Temperatures," Journal of the Mechanics and Physics of Solids, Vol.59, pp. 696–712, 2011.

11) An N. and Pochiraju K., "Modeling Damage Growth in Oxidized High-Temperature Polymeric Composites," The Journal of the Minerals, Metals & Materials Society (TMS), Vol. 65, pp. 246–255, 2013.

12) Liang J. and Pochiraju K., "Oxidation-Induced Damage Evolution in a Unidirectional Polymer Matrix Composite," Journal of Composite Materials, Vol. 49, pp. 1393–1406, 2015.

13) Daghia F., Zhang F., Cluzel C. and Ladevèze P., "Thermo-Mechano-Oxidative Behavior at the Ply's Scale: The Effect of Oxidation on Transverse Cracking in Carbon–Epoxy Composites," Composite Structures, Vol. 134, pp. 602–612, 2015.

14) Pochiraju K.V., Tandon G.P. and Schoeppner G.A., "Evolution of Stress and Deformations in High-Temperature Polymer Matrix Composites During Thermo-oxidative Aging," Mechanics of Time-Dependent Materials, Vol. 12, pp. 45–68, 2008.

15) Schoeppner G.A., Tandon G.P. and Ripberger E.R.,"Anisotropic Oxidation and Weight Loss in PMR-15 Composites," Composites: Part A, Vol. 38, pp. 890–904, 2007.

16) Upadhyaya P., Roy S., Haque M. H. and Lu H., "Influence of Nano-Clay Compounding on Thermo-Oxidative Stability and Mechanical Properties of a Thermoset Polymer System", Composites Science and Technology, Vol. 84, pp. 8–14, 2013.

17) Haque M. H., Upadhyaya P., Roy S., Ware T., Voit W. and Lu H., "The Changes in Flexural Properties and Microstructures of Carbon Fiber Bismaleimide Composite after Exposure to a High Temperature", Composite Structures, Vol. 108, pp. 57–64, 2014.

18) Tuttle, M.E., Structural Analysis of Polymeric Composite Materials. CRC Press. 2003.

19) Asadpoure A., Mohammadi S. and Vafaia A., "Modeling Crack in Orthotropic Media Using a Coupled Finite Element and Partition of Unity Methods", Finite Elements in Analysis and Design, Vol. 42, pp. 1165–1175, 2006.

20) Huynh D. B. P. and Belytschko T., "The Extended Finite Element Method for Fracture in Composite Materials", International Journal for Numerical Methods in Engineering, Vol. 77, pp. 214–239, 2009.

21) Ebrahimi S.H., Mohammadi S., and Asadpoure A., "An Extended Finite Element (XFEM) Approach for Crack Analysis in Composite Media", International Journal of Civil Engineerng, Vol. 6, pp. 198–207, 2008.

22) Fayolle B., Audouin L. and Verdu J., "Oxidation Induced Embrittlement in Polypropylene – a Tensile Testing Study", Polymer Degradation and Stability, Vol. 70, pp. 333–340, 2000.

23) Wu W-F, Cheng H-C and Kang C-K. "Random Field Formulation of Composite Laminates", Composite Structures, Vol. 49, pp. 87–93, 2000.

24) Barber A, Kaplanashiri I, Cohen S, et al. "Stochastic strength of nanotubes: an appraisal of available data", Composite Science and Technology, Vol. 65, pp. 2380–2384, 2005.

25) Hussein, R.M., Anandan, S., and Chandrashekhara, K. "Flexural Behavior of Cross-Ply Thermally Aged Bismaleimide Composites" CAMX conference Proceedings, Anaheim, CA, September, 26-29, 2016.

26) Hussein, R. M., Anadan, S., and Chandrashekhara, K. "Anisotropic Oxidation Prediction using Optimized Weight Loss Models of Bismaleimide Composites." Journal of Materials Science, Vol. 51, pp. 7236–7253, 2016.

SECTION

4. CONCLUSIONS

The work performed in this dissertation provides a valuable procedure for developing a multi-scale framework for comprehensive thermo-oxidation damage study of HTPMC.

The first paper provides a micromechanical modeling approach for thermo-oxidation using 3-D FEA and optimization scheme for the proportionality parameter using GPS. The anisotropic growth in the oxidized layer and degree of non-linearity for the oxidized layer thickness at 176.67 °C (350 °F) and 200 °C (392 °F). A novel index is presented that corresponds to the weight loss per unit volume of the completely oxidized matrix. The analysis of thermo-oxidation behavior at the RVE level is more realistic, reflecting the diffusion-reaction mechanisms rather than incorporating the effect of area ratios as it is shown in the sample level. By simulation, the initial high rate of oxidized layer growth is markedly shown at both temperatures in the longitudinal direction; however, weight loss % predictions do not show a remarkable initial weight loss % rate in all directions.

The second paper provides a detailed study of mechanical behavior of thermally aged cross-ply BMI composites under bending loading experimentally and numerically. An analysis of the degradation mechanisms: cross-linking and oxidation in a multiscale approach is. The cross-linking mechanism degrades the composite flexural behavior in the range (t<500 hours) that BMI composites show a strong tendency to cross-link during

aging. The simulation results show that the cross-linking progression mainly affects the elastic properties at the mesoscale while, insignificantly affects the strength properties at the same level. The failure of the matrix due to compression is the critical mechanism of failure among the fiber tension/compression and matrix tension/shear. After being aged for 1,700 hours, samples show 0.5 % loss of the original weight and 19 % reduction in the flexural modulus. The cross-linking completion is at around 500 hours where the T_g plot shows the lowest rate of change with aging time. The formation of "blunt" micro-cracks around 500 hours reveals that the oxidative shrinkage reached a critical value.

In the third paper, a multiscale approach is proposed to simulate the shrinkage deformation and micro-scale cracking damage at 200 °C. The effects of the global thermo-oxidation on the local boundary conditions are considered by running macro- and meso-scale simulations and extracting the induced 3D displacements (u, v, and w). The oxidative macro-shrinkage strain is assumed linearly dependent on the oxidation state variable and attains its maximum value $\varepsilon_s^{ox} = 2.5 \times 10^{-5}$ when the matrix is completely oxidized. However, the local value of the maximum shrinkage strain is $\varepsilon_s^{ox}(local) = 3.25 \times 10^{-4}$ and has the local crack matched to the SEM image measurements. This suggested a distribution of the form $\varepsilon_s^{ox}(local) = f(x, y, z)$ similar to all material properties. Since testing is not practical at the local scale, powerful simulation schemes are necessary under reasonable assumptions especially, the boundary conditions. The micro-cracking is validated using a 3D static simulation to the OOF- generated/replicated mesh and geometrical domain. Not only the crack length is closely simulated, but also the crack meander and opening. However, the procedure is validated for a real crack; a plethora of future validation cases are required to generalize the approach.

BIBLIOGRAPHY

1) Schoeppner, G.A., Tandon, G.P. and Pochiraju, K.V. Multiscale Modeling and Simulation of Composite Materials and Structures. Springer 2008.

2) Boyd, J., Bongiovanni, C.L. and Thai, B. "Bismaleimide Resin with High Temperature Thermal Stability." U.S. Patent 2007/0117956 A1, May 24, 2007.

3) Bellenger, V., Decelle, J. and Huet, N. "Ageing of a Carbon Epoxy Composite for Aeronautic Applications." Composites: Part B 36 (2005): 189–194.

4) Kung, H-K. "Effects of Surface Roughness on High-temperature Oxidation of Carbon-Fiber-Reinforced Polyimide Composites." Journal of Composite Materials 39 (2005): 1677–1687.

5) Chung, K., Seferis, J.C. and Nam, J.D. "Investigation of Thermal Degradation Behavior of Polymeric Composites: Prediction of Thermal Cycling Effect from Isothermal Data." Composites: Part A 31 (2000): 945–957.

6) Pochiraju, K.V., Tandon, G.P. and Schoeppner, G.A. "Evolution of Stress and Deformations in High-Temperature Polymer Matrix Composites During Thermo-oxidative Aging." Mechanics of Time-Dependent Materials 12 (2008): 45–68.

7) Roy, S., Sing, S. and Schoeppner, G.A. "Modeling of Evolving Damage in High Temperature Polymer Matrix Composites Subjected to Thermal Oxidation." Journal of Materials Science 43 (2008): 6651–6660.

8) Roy, S. and Sing, S. "Prediction of Thermo-Oxidative Degradation in Polymer Matrix Composites Using Micromechanical Modeling and Homogenization at the Macro-Scale." Mechanics of Advanced Materials and Structures, 19 (2012): 68–78.

9) Upadhyaya, P., Sing, S., and Roy, S. "A Mechanism-Based Multi-Scale Model for Predicting Thermo-Oxidative Degradation in High Temperature Polymer Matrix Composites." Composites Science and Technology 71 (2011): 1309–1315.

10) Haque, M. H., Upadhyaya, P., Roy, S., Ware, T., Voit, W. and Lu, H. "The Changes in Flexural Properties and Microstructures of Carbon Fiber Bismaleimide Composite After Exposure to a High Temperature." Composite Structures 108 (2014): 57–64.

11) Meng, M., Le, H.R., Rizvi, M.J. and Grove, S.M. "3D FEA Modeling of Laminated Composites in Bending and Their Failure Mechanisms." Composite Structures 119 (2015): 693–708.

12) Antoun, B., Qi, H.J., Hall, R., Tandon, G.P., Lu, H., Lu, C., Furmanski, J. and Amirkhizi, A., Challenges in Mechanics of Time-Dependent Materials and Processes in Conventional and Multifunctional Materials, Volume 2. Springer 2014.

13) Langer S., Fuller E. R., and Carter W. C., "OOF: An Image-Based Finite-Element Analysis of Material Microstructures," Computing in Science and Engineering, Vol. 3, pp. 15–23, 2001.

14) Reid A. C. E., Langer S. A., Lua R. C., Coffman V. R., Haan S.–I., and Garcia R. E., "Image-Based Finite Element Mesh Construc¬tion for Material Microstructures," Computational Material Sci¬ence, Vol. 43, pp. 989–999, 2008.

15) Reid A. C. E., Lua R. C., Garcia R. E., Coffman V. R., and Langer S. A., "Modeling Microstructures with OOF2," International Jour¬nal of Materials and Product Technology, Vol. 35, pp. 361–373, 2009.

16) Coffman V. R., Reid A. C. E., Langer S. A., and Dogan G., "OOF3D: An Image-Based Finite Element Solver for Materials Science," Mathematics and Computers in Simulation, Vol. 82, pp. 2951–2961, 2012.

17) Goel A., Chawla K.K., Vaidya U.K., Chawla N. and Koopman M., "Two Dimensional Microstructure Based Modeling of Young's Modulus of Long Fibre Thermoplastic Composite," Materials Science and Technology, Vol. 24, pp. 864–869, 2008.

18) Dong Y. and Bhattacharyya D., "Two Dimensional Microstructure Based Modeling of Young's Modulus of Long Fibre Thermoplastic Composite," Mechanics of Advanced Materials and Structures, Vol. 17, pp. 534–541, 2010.

19) Dong Y. and Bhattacharyya D., "Mapping the Real Micro/Nanostructures for the Prediction of Elastic Moduli of Polypropylene/Clay Nanocomposites," Polymer, Vol. 51, pp. 816–824, 2010.

20) An N. and Pochiraju K., "Modeling Damage Growth in Oxidized High-Temperature Polymeric Composites," The Journal of the Minerals, Metals & Materials Society (TMS), Vol. 65, pp. 246–255, 2013.

21) Liang J. and Pochiraju K., "Oxidation-Induced Damage Evolution in a Unidirectional Polymer Matrix Composite," Journal of Composite Materials, Vol. 49, pp. 1393–1406, 2015.

22) Daghia F., Zhang F., Cluzel C. and Ladevèze P., "Thermo-Mechano-Oxidative Behavior at the Ply's Scale: The Effect of Oxidation on Transverse Cracking in Carbon–Epoxy Composites," Composite Structures, Vol. 134, pp. 602–612, 2015.

VITA

Mr. Rafid Muhammad Hussein was born in Basra, Iraq. He was admitted to the University of Basra, Iraq in 1998 and received his Bachelor's degree in Mechanical Engineering in 2002. He worked at the State Company of Iron and Steel, Iraq, as a Mechanical Engineer from September 2003 to September 2009. He continued his graduate study at the University of Basra, Iraq and received his M.S. degree in Mechanical Engineering in 2009.

In January 2012, Mr. Rafid Hussein enrolled in the Ph.D. Program in Mechanical Engineering at Missouri University of Science and Technology. He has served both as a Graduate Research Assistant and Graduate Teaching Assistant between January 2012 and May 2018 in the Department of Mechanical and Aerospace Engineering. In May 2018, he received his Ph.D. degree in Mechanical Engineering from Missouri University of Science and Technology, Rolla, Missouri.